

Optimized Core Design and Fuel Management of a Pebble-Bed Type Nuclear Reactor

Optimized Core Design and Fuel Management of a Pebble-Bed Type Nuclear Reactor

Proefschrift

ter verkrijging van de graad van doctor
aan de Technische Universiteit Delft,
op gezag van de Rector Magnificus Prof. dr. ir. J.T. Fokkema,
voorzitter van het College van Promoties,
in het openbaar te verdedigen
op dinsdag 20 januari 2009 om 10:00 uur
door

Brian BOER

werktuigkundig ingenieur
geboren te Rotterdam.

Dit proefschrift is goedgekeurd door de promotor:

Prof. dr. ir. T.H.J.J van der Hagen

Copromotor:

Dr. ir. J.L. Kloosterman

Samenstelling promotiecommissie:

Rector Magnificus,	voorzitter
Prof. dr. ir. T.H.J.J van der Hagen,	Technische Universiteit Delft, promotor
Dr. ir. J.L. Kloosterman,	Technische Universiteit Delft, copromotor
Prof.[em] dr. ir. H. van Dam,	Technische Universiteit Delft
Prof. dr. ir. A.H.M. Verkooijen,	Technische Universiteit Delft
Dr. A.M. Ougouag,	Idaho National Laboratory, USA
Dr. ir. J.C. Kuijper,	Nuclear Research and consultancy Group
Prof. dr. H.Th. Wolterbeek,	Technische Universiteit Delft
Prof. dr. I.M. de Schepper,	Technische Universiteit Delft, reservelid

©2008, Brian Boer and IOS Press

All rights reserved. No part of this book may be reproduced, stored in a retrieval system, or transmitted, in any form or by any means, without prior permission from the publisher.

ISBN 978-1-58603-966-0

Keywords: High Temperature Reactor, pebble-bed, core optimization

Published and distributed by IOS Press under the imprint Delft University Press

Publisher

IOS Press

Nieuwe Hemweg 6b

1013 BG Amsterdam

The Netherlands

tel: +31-20-688 3355

fax: +31-20-687 0019

email: info@iospress.nl

www.iospress.nl

www.dupress.nl

LEGAL NOTICE

The publisher is not responsible for the use which might be made of the following information.

PRINTED IN THE NETHERLANDS

The research described in this thesis was performed in the section Physics of Nuclear Reactors (PNR), of the department Radiation, Radionuclides & Reactors (R³), of the Delft University of Technology, Delft, The Netherlands.
Visiting address: Mekelweg 15, 2629 JB Delft, The Netherlands

Financial support

Part of the work presented in this thesis was financed under the European Commission / EURATOM 6th Framework Programme RAPHAEL (ReActor for Process heat, Hydrogen And ELectricity generation), contract number 516508 (FI6O), effective April 2005 - April 2009

Part of the work presented in this thesis was financed by the Nuclear Research and consultancy Group (NRG), Petten, the Netherlands

Part of the work presented in this thesis has been financially supported by the Idaho National Laboratory, Idaho, USA

Contents

1	Introduction	1
1.1	High Temperature Gas-cooled Reactors	2
1.2	Research and development of the Very High Temperature Reactor	5
1.3	High Temperature Reactor designs relevant for this thesis	10
1.4	Hydrogen production methods	15
1.5	Objective and outline of this thesis	20
2	Validation of a neutronics and thermal-hydraulics code system for the simulation of pebble-bed reactors	23
2.1	Neutron cross section calculation procedure	24
2.2	Coupled DALTON-THERMIX code system	26
2.3	Simulation of the HTR-10	28
2.4	Simulation of the AVR	36
2.5	Simulation of the Pebble Bed Modular Reactor	43
2.6	Conclusion	48
3	Performance of coated particle fuel in High Temperature Reactors	51
3.1	Calculation procedure in stress analysis	52
3.2	Derivation of an analytical model for a 4-layer pressure vessel	55
3.3	Stress effects in the graphite matrix	61
3.4	Stress analysis of coated particle fuel in current and future HTRs	66
3.5	Conclusion	72
4	Fuel management optimization for pebble-bed reactors	75
4.1	Fuel management in pebble-bed reactors	75
4.2	Determination of the equilibrium core composition and power profile	76
4.3	Possible modifications of the pebble recycling scheme	79
4.4	Impact of multiple pebble recycling on the reactor performance	81
4.5	Impact of radial fuel zoning on the reactor performance	83
4.6	Fuel temperature of the improved design	90
4.7	Conclusion	90

5	Alternative pebble-bed concepts	93
5.1	The OTTO core	93
5.2	The conical core	96
5.3	The radially cooled core	98
5.4	Optimized radially cooled core design	104
5.5	Conclusion	107
6	Conclusions and discussion	111
6.1	Conclusions	111
6.2	Discussion and recommendations	113
A	Point kinetic equations and HTR-10 reactivity coefficients	115
A.1	Neutron point kinetic equations	115
A.2	Applicability of point kinetics	116
A.3	Reactivity coefficients of the HTR-10	116
B	Description of the DALTON and THERMIX codes	117
B.1	The neutronics code DALTON	117
B.2	The thermal-hydraulics code THERMIX	119
C	Coefficients used in stress analysis equations	121
	Nomenclature	125
	Bibliography	131
	List of publications	141
	Summary	143
	Samenvatting	147
	Acknowledgments	151
	Curriculum Vitae	153

1

Introduction

This chapter gives an overview of the past and present research efforts concerning the High Temperature Reactor (HTR). The first section describes the development of past HTR designs, while Sec. 1.2 presents the successive Very High Temperature Reactor (VHTR) research efforts and the related scientific and technical issues. Sec. 1.3 gives a detailed description of three HTR designs relevant for this thesis. The designs serve as a starting point for the development of an improved HTR core design. Sec. 1.4 gives a short overview of modern hydrogen production methods that could be coupled to a VHTR. The last section of this chapter gives the objective and the outline of this thesis.

The renewed interest in HTR technology can be associated with the developments in the world-wide energy market. The world's population is expected to grow from about 6 billion people to 10 billion in the coming decades. Together with an increase of the living standards this growth is expected to lead to an enormously higher demand for energy [1]. To cope with this increased demand, while omitting the use of increasingly scarce fossil fuels (oil) and avoiding an adverse environmental impact, there is a need for energy supply that is not only cost-effective and reliable but also safe and clean.

Nuclear energy by means of the 439 nuclear reactors operating world-wide today generate 16 % of the global electricity production and almost one third of the European electricity production [2]. Nuclear energy is a nearly carbon-free source of energy. A 1 GW nuclear plant can avoid about 6-7 million tonnes of CO₂ per year as well as related airborne pollutants as compared to a coal-fired plant. However, the largest share of the energy consumption comes from the transport sector which today uses mainly petrol as an energy carrier. Future technologies for the transport sector include major changes, such as electrically powered vehicles using batteries or fuel cell technology. The latter uses hydrogen (or methanol) as an energy carrier. The use of synthetic fuels for the transport sector has also gained a renewed interest.

The use of nuclear energy for the production of hydrogen or electricity for this purpose would create an envelope for emission reduction. Furthermore, hydrogen is

increasingly used today for the improvement of the degrading quality of oil (petrol) and is used in fertilizer plants [3]. The current market for hydrogen is 40 million metric tons/year (2005), worth about \$135 billion/year and growing about 10 % per year [4].

It is expected that nuclear energy will play an important role in the future energy mix, whether this will be limited to the replacement of the existing nuclear plants or by expansion of the nuclear fleet, either to meet the increasing demand for electricity or even in a dedicated role for hydrogen production.

1.1 High Temperature Gas-cooled Reactors

Promising among the existing nuclear reactor designs is the High Temperature Gas-cooled Reactor (HTGR or HTR) that has inherent safety characteristics and a high coolant temperature leading to a high efficiency and possibilities for process heat applications.

Gas-cooled HTRs originate from the first experimental nuclear reactors in the 1940s that operated in the US and used air at atmospheric pressure as a coolant [5]. Table 1.1 gives an overview of gas-cooled reactors that operated in the past. Although in the US priority had been given to high power density reactors using (pressurized) water as a coolant, interest in gas cooling led to the construction and operation of gas-cooled reactors in the UK and France in the 1950s. These so-called MAGNOX reactors used metallic natural uranium fuel with a magnesium-aluminum cladding and pressurized CO₂ as a coolant. Carbon-dioxide was chosen instead of air, because of its better thermal properties and the potential for higher temperature operation. The coolant outlet temperature in these reactors was however limited to 415 °C because of the possible CO₂ oxidation and melting of the cladding (~645 °C) and the phase change of the metallic uranium at 665 °C. The follow-up of the MAGNOX reactor, the Advanced Gas-Cooled Reactor (AGR), therefore used uranium oxide as fuel contained in a stainless steel cladding, which allowed for a coolant outlet temperature of 675 °C thereby improving the efficiency to 41.5 %. In another approach the CO₂ coolant was replaced with helium together with an all-ceramic core. The investigation of this HTGR concept was initiated at the same time both in the UK, where the DRAGON reactor reached first criticality in 1964 [6], and in Germany with the construction and operation in 1968 of the AVR pebble-bed reactor [7]. Furthermore, the Peach Bottom reactor [8], an HTGR using cylindrical fuel elements, was constructed and went in operation in 1967 in the US.

The above research efforts led to the construction of demonstration plants in the US with the Fort St. Vrain reactor [9] and in Germany with the Thorium High Temperature Reactor (THTR) [5, 10]. While the American design of General Atomics used prismatic fuel elements, the Germans continued with the use of spherical fuel (pebbles) [11]. The helium outlet temperature of these reactors was around

Table 1.1: *Main characteristics of past gas-cooled reactors.*

Reactor	MAGNOX	AGR	DRAGON	Peach Bottom	THTR
First power operation	1956	1963	1965	1967	1984
Country	UK\France	UK	UK	US	Germany
Power [MW _e]	35-590	625	20 (th.)	40	300
Efficiency [%]	19-34	41	-	35	40
Fuel element	Slugs	Rods	Rods (hex.)	Cylinders	Pebbles
Fuel loading	Nat. U	UO ₂	U-ThC	U-ThC	U-ThO ₂
Enrichment ²³⁵ U [%]	0	1.5-2.5	93	93.5	93
Coolant	CO ₂	CO ₂	He	He	He
Coolant T _{out} [°C]	335-415	635-675	750	770	750
Power dens. [MW/m ³]	0.5-1.8	2.6	14	8.3	6.0

750 °C. The designs emphasized on increasing the reactor size and for this reason a Pre-stressed Concrete Reactor Vessel (PCRv) was adopted in order to reduce the mechanical stresses in the large pressure vessel. Furthermore, the thorium fuel cycle, using highly enriched (93%) ²³⁵U and ²³³U with ²³²Th as the fertile material, was chosen for these designs. The high number of neutrons per neutron absorbed (η) for ²³³U in the thermal energy spectrum [12] of an HTR is the incentive behind this choice.

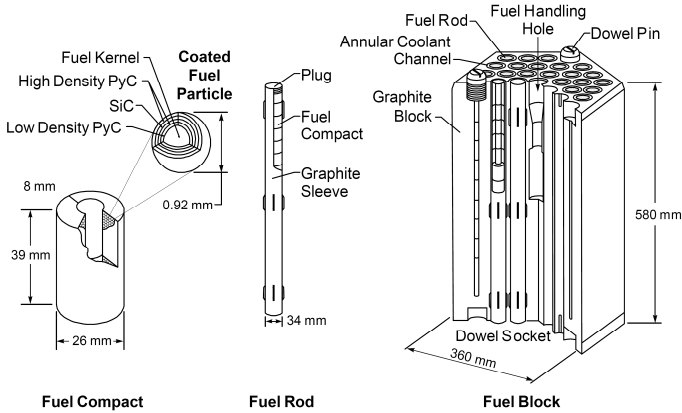
Because of the low uranium price in the decades that followed and the increased public demand for reactor safety the next HTR designs emphasized on a small sized modular cores with inherent safety characteristics using the once through ²³⁵U fuel cycle. The HTR-MODUL, a 200 MW_{th} design with an helium outlet of 950 °C using 8.6 % enriched UO₂, is prominent among these designs [13].

The inherent safety of the reactor is based upon the negative fuel and moderator temperature reactivity coefficients, the high thermal capacity of the graphite and the ability of the graphite structures in the core to transfer heat to the outer surface of the reactor by conduction and radiation in the absence of the coolant. By limiting the size and the maximum power density, while keeping a large outer surface area of the reactor for heat removal, one can ensure that the temperatures of the fuel remain below the limit during accident scenarios.

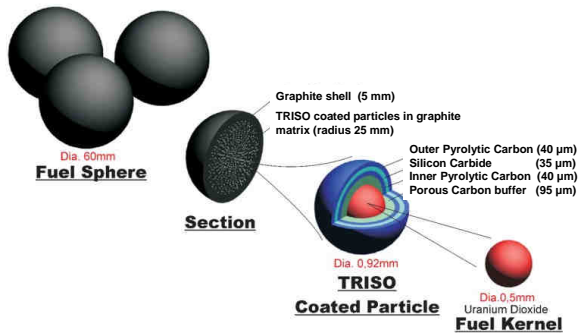
High Temperature Reactor fuel

At present, two fuel types remain for HTRs, which are the prismatic block type fuel and pebble type fuel. The prismatic fuel, shown in Fig. 1.1(a), consists of a graphite hexagonal block equipped with boreholes for the placement of fuel compacts or burnable poison rods and holes for coolant flow. The reactor core consists of several columns of stacked prismatic blocks surrounded by graphite reflectors. Some of the blocks are dedicated to reactor control and have three larger holes for the insertion

1. Introduction



(a) Prismatic type fuel



(b) Pebble type fuel

Fig. 1.1: Schematic overview of HTR fuel; (a) prismatic fuel blocks that contain fuel rods consisting of compacted TRISO particles in a graphite matrix; (b) a pebble containing TRISO coated particle fuel in a graphite matrix fuel zone surrounded by a 0.5 cm graphite shell.

of control rods and absorber spheres, which act as the reserve shutdown system. Although burnable poison is used for long term reactivity control, reactor operation has to be stopped for replacing and re-arranging fuel blocks.

The fuel holes are filled with rods made of TRISO coated particle fuel 1.1(a) compacted in a graphite matrix. The TRISO particles have a UO_2 (or a UC) kernel at their very center. Adjacent to the kernel is a porous carbon buffer layer designed to retain gaseous fission products and is coated with an Inner Pyrolytic Carbon (IPyC) layer, a Silicon Carbide (SiC) layer and an Outer Pyrolytic Carbon layer (OPyC).

The core of a Pebble-Bed type HTR contains several hundreds of thousands of

pebbles that form a porous bed through which the helium coolant flows. The graphite pebbles, with a diameter of 6 cm, contain the nuclear fuel within their fueled region of 5 cm radius. This fueled region consists of a graphite matrix containing tens of thousands of TRISO coated particles.

The pebbles are inserted in the core cavity to form a randomly packed pebble-bed. The advantage of the pebble-bed reactor is its possibility to re-fuel the core on-line by removing 'burned' pebbles from the bottom of the core and inserting fresh pebbles at the top. Since long term reactivity can be controlled effectively in this manner, there is no need for excess reactivity or burnable poison.

1.2 Research and development of the Very High Temperature Reactor

At present there are two HTRs operating in the world, namely the prismatic HTTR [14] in Japan and the pebble-bed type HTR-10 at the INET in China [15]. The construction of two demonstration-size plants is envisaged for the near future. The first is the Pebble Bed Modular Reactor (PBMR) design [16] in South Africa and the second is the HTR-PM in China [17], which are both based on the German HTR-MODUL design.

Japan: the HTTR

The Japan Atomic Energy Research Institute (JAERI) designed and constructed the High Temperature engineering Test Reactor (HTTR) in order to establish and upgrade the HTR technology basis in Japan and investigate high temperature heat applications. The HTTR is a 30 MW_{th} reactor with an maximum coolant outlet temperature of 950 °C that reached first criticality in 1998 [18]. The HTTR uses prismatic fuel blocks (see Fig. 1.2) and has a steel containment, although SiC coated low enriched (2-6 % ²³⁵U) UO₂ fuel is used, which makes the containment redundant. Various irradiation tests for fuels and materials have been initiated since 2005. The aim is to have a hydrogen production test facility coupled to the HTTR by 2015.

China: the HTR-10 and the HTR-PM

China began research work on pebble-bed high temperature gas cooled reactors at the end of the 1970s. In 1992 the Chinese government approved to build a 10 MW_{th} pebble-bed test reactor, the HTR-10, at the Institute of Nuclear and New Energy Technology (INET) of the Tsinghua University in Beijing. The HTR-10, which is largely based on the German HTR-MODUL design, reached criticality in December 2000.

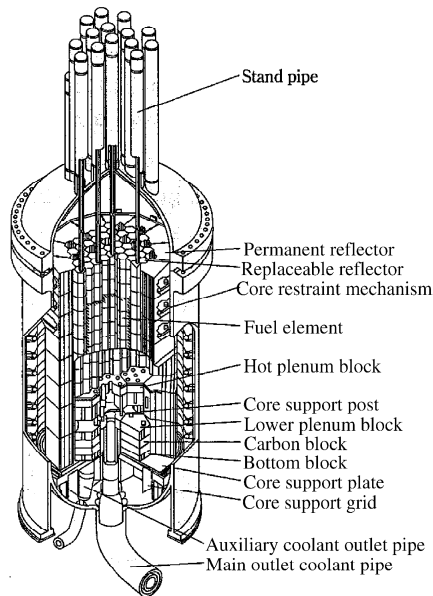


Fig. 1.2: *The prismatic block type HTTR.*

The follow-up of the HTR-10 is the High Temperature gas-cooled Reactor Pebble-bed Module (HTR-PM), which aims at a reactor power of at least 200 MW_e to be completed in 2013 [17]. The main objectives of the HTR-PM project are to demonstrate the inherent safety features for a large design and to show that an HTR is economically viable by adopting modularization of the design. Besides the original reactor design with a thermal power of 458 MW an alternative design of 250 MW is being considered [19]. The HTR-PM employs a steam cycle, while a gas turbine cycle and coupling to a hydrogen production facility are considered for the future, but will be tested on the HTR-10 first.

South Africa: the PBMR

The Pebble Bed Modular Reactor (PBMR) has been under development in South Africa since 1994 [16]. It was found that an increase of the reactor size from 302 MW to 400 MW was necessary to stay within the commercial targets aiming at 1000 - 1500 US \$ per installed kW. Some of the design considerations in achieving this increase in reactor power, while maintaining inherent safety, are discussed here. The conceptual design moved from a copy of the HTR-MODUL to a 400 MW design with a center reflector, thereby avoiding high temperatures in the core center. Furthermore, a direct gas turbine cycle was adopted to achieve higher efficiency. To stay within safety limits the annular core design moved from a dynamic inner reflector to a solid one. The

advantage of the dynamic column is that it can easily deal with high levels in fast neutron fluence that are common for the center part of the core, since it consists of replaceable graphite pebbles that can be circulated together with the fuel pebbles. However, at the boundary of the dynamic inner reflector and the surrounding zone of fuel pebbles a mixing zone exists. In this region the thermal neutron flux peaks and is even higher in the mixing zone than in the fuel zone. This impacts negatively on the maximum fuel temperatures in a Depressurized Loss Of Forced Cooling (DLOFC) event as the fuel in the mixing zone generates more energy than the fuel closer to the outside surface of the core. Furthermore, it also reduces the effectiveness of the control elements that are located in the outer reflector. These two factors, as well as the large bypass flow through the inner dynamic reflector proved to be the limiting factors to a possible increase in power level. By adopting a fixed inner reflector these problems are avoided and it offers the possibility of placing control elements in the center of the core, where their reactivity effect is the highest. Therefore, the cold shutdown system, consisting of small absorber spheres that can drop into boreholes, is located in the inner reflector in the present design.

The use of a PCRV is avoided since it does not allow for the passive removal of the decay heat through the outer surface of the reactor during accident situations. The ability to manufacture and transport the RPV limits the diameter size to 6.2 m and thereby determines the maximum size of the entire reactor, which in theory could be made larger for an annular core.

The Generation IV initiative

The Generation IV International Forum is a research initiative for the development of the fourth generation nuclear power plants [20]. The six most promising reactor concepts were selected on the basis of their ability to provide in a reliable and safe energy system together with a reduced nuclear waste production and increased economic competitiveness. The aim is to research and allow deployment of the following reactors before the year 2030: the Supercritical Water Reactor (SCWR), the Gas Cooled Fast Reactor (GCFR), the Sodium cooled Fast Reactor (SFR), the Lead cooled Fast Reactor (LFR), the Molten Salt Reactor (MSR) and the Very High Temperature Reactor (VHTR). The VHTR is a continuation and optimization of the present HTR designs with the aim of reaching a coolant outlet temperature of 1000 °C or beyond, which would increase reactor performance.

Linked to the VHTR of the Generation IV initiative are the development of the Next Generation Nuclear Plant in the US and the RAPHAEL project in the EU.

The US: the Next Generation Nuclear Plant

The Next Generation Nuclear Plant (NGNP) project in the US aims for the construction of a full-scale prototype VHTR by 2015. The main project goals are the demonstration of an inherently safe HTR with a high helium outlet temperature (1000 °C) using the nuclear Brayton cycle. Furthermore, the final goal is the nuclear-assisted production of hydrogen. Both prismatic block type and pebble fuel are still considered for the NGNP design with a once-through low-enriched uranium fuel cycle at a high burnup value.

Several core design optimization studies have been performed [21]. Modifications to the bypass flow and flow distribution of the existing prismatic block type GT-MHR design by General Atomics [22] resulted in an increase of the helium outlet temperature to 1000 °C without exceeding the peak transient fuel temperature limit of 1600 °C. Two inherently safe pebble-bed versions with a reactor power of 300 and 600 MW_{th} have been developed. By modifying the fuel zone radius of the pebble the fuel-to-moderator ratio has been optimized [23, 24]. This resulted in an improvement of the fuel utilization and the safety characteristics.

Several remaining issues have been identified during the design process [21]:

- It has been found that neutron cross section generation procedures require further refinement, which could be achieved by a better treatment of the Dancoff factor to account for shadowing effects in the double heterogeneous fuel (TRISO and pebble).
- The potential for 'hot streaking' (the possible formation of hot spots by fresh fuel pebbles) has to be assessed. A tailored loading of the burned pebbles could mitigate this problem.
- A large pressure drop was encountered for the 600 MW_{th} design, which could be reduced by directing the flow radially through the core thereby increasing the plant's efficiency with several percent. It is noted this modification could, in turn, increase the fuel temperature.
- A reduction of the coolant inlet temperature (<500 °C) would allow for the use of more conventional materials for the RPV, core barrel and other metallic core internal components.

It was found that the performance of the block type and pebble-bed designs with regard to safety are comparable. The pebble-bed has a better fuel utilization, requires less excess reactivity and has a lower fuel temperature (difference of 100 - 200 °C), while its disadvantages are the production of graphite dust in the primary cooling system and a higher core pressure drop.

The EU: the RAPHAEL project

In April 2005 an Integrated Project RAPHAEL (ReActor for Process Heat And Electricity) started on HTR/VHTR technology as part of the EURATOM 6th Framework Programme [25]. The main objective of this project is the increase of HTR reactor performance (operating temperature 800-1000 °C and burnup up to 200 MWd/kg HM). The development of such an HTR/VHTR goes far beyond the characteristics of past and present HTR operating reactors, both with pebble-bed cores (AVR, THTR, HTR-10) and block type cores (Peach Bottom, Fort St. Vrain and HTTR). The inherent safety features adopted by all present prototype projects, have not been used for large scale reactors yet; the temperatures aimed at, in the range 800-1000 °C, require materials with higher performances than those used in past HTRs, which need specific qualification. Operating HTR fuel in this range of temperature with a target burn-up (150-200 MWd/kg HM) higher than in previous projects is beyond existing industrial experience.

Furthermore, the project emphasizes on large scale industrial process heat applications for HTRs, for which no experience exists, not even at lower temperatures. For such applications, a large heat exchanger (Intermediate Heat Exchanger IHX) with a heat transfer capacity of several hundreds of megawatt, operating at high or very high temperature, is necessary.

The Delft University of Technology is one of the participating universities in the RAPHAEL project, having a tradition in HTR pebble-bed research. This research resulted in several PhD theses on various pebble-bed reactor physics topics: the validation of numerical methods for criticality analysis [26]; the possibility of plutonium burning in a pebble-bed reactor to reduce plutonium stockpiles [27]; and the possibility of adopting a fast spectrum in a pebble-bed reactor [28]. Furthermore, the implications of using an HTR in the direct Brayton cycle has been investigated focusing both on the reactor and on the energy conversion system [29, 30].

High Temperature Liquid-Salt-Cooled Reactors

As an alternative for helium, liquid salt can be used as a coolant for HTRs in combination with either prismatic block type fuel (AHTR) [31] or pebble fuel (LSPBR) [32]. The advantage of liquid salt, such as ${}^7\text{Li}_2\text{BeF}_4$ (Flibe), over helium is its better (volumetric) thermal capacity and heat transfer capability. Compared to helium at 70 bar and 1000 K with $\rho c_p = 17.4 \text{ kJ/m}^3/\text{K}$ and $\lambda = 3.9 \cdot 10^{-1} \text{ W/m/K}$, Flibe has superior properties with $\rho c_p = 4.5 \cdot 10^3 \text{ kJ/m}^3/\text{K}$ and $\lambda = 1.1 \text{ W/m/K}$ at atmospheric pressure, resulting in lower fuel temperatures and pressure losses. Disadvantages of Flibe are however its high melting point of 457 °C, its toxicity and possible corrosive interaction with other materials and the fact that Flibe has a higher neutron absorption cross section than helium. A possible detrimental effect on the temper-

ature reactivity coefficient can be easily avoided, but puts some restrictions on the reactor design [32]. The helium cooled HTR lacks this disadvantages, since helium is chemically inert and has a very low neutron absorption cross section ($\Sigma_a = 3.5 \cdot 10^{-6}$) at 70 bar and 1000 K.

VHTR technical issues

Besides the technical issues that were stated above the following items have to be addressed on the way to an HTR that can operate with a coolant outlet temperature of 1000 °C, while maintaining its inherent safety characteristics:

- The integrity of the coated particle for the increased operating temperature has to be addressed since it serves as the containment of the fission products. An increase of the fuel temperature could increase stresses in the coatings which would lead to an increase of the particle failure probability.
- Even higher temperatures are desirable to further increase efficiency. Therefore an optimization of the core is probably required including tailored re-loading of burned pebbles and a modification of the coolant flow direction.
- The coolant temperature range and reactor power might be optimized to a specific heat application in use. Prominent among these applications is the production of hydrogen.

The following section provides a detailed description of relevant pebble-bed reactor designs, which serve as a starting point for further studies.

1.3 High Temperature Reactor designs relevant for this thesis

From the previous sections it is found that the HTR-MODUL [33] is the predecessor of modern pebble-bed designs (PBMR, HTR-PM). The design of the HTR-MODUL (see Table 1.2) was based on the criterion that the fuel temperature would remain within limits, even in the absence of active cooling systems and a complete loss of the coolant. This led to a design with a small core diameter (3m) allowing the reactor to be shut down by control rods in the side reflector only and to avoid high temperatures in the center of the core. In order to avoid high temperatures (<1600 °C) during accident conditions the power density was limited to 3.0 MW/m³. To achieve a reactor power of 200 MW_{th} a core height of 9.4 m was chosen, resulting in the tall core design which is still employed by the modern designs. Both the low enriched uranium fuel in coated particles and the concept of inherent safety of the MODUL design were demonstrated in the AVR test reactor.

A detailed description of three pebble-bed reactor designs is given below, namely the AVR, the HTR-10 and the PBMR. The AVR and HTR-10 are small test reactors in which the basic technology of the pebble-bed reactor concept has been investigated.

In these reactors a shut down of active cooling under depressurized and pressurized conditions, respectively, without intervention of a safety system have been conducted successfully, without a significant increase in the fission product release from the fuel. The PBMR design adopts this concept of inherent safety while scaling the reactor power for economic reasons as high as allowable.

The AVR

The Arbeitsgemeinschaft Versuchsreaktor (AVR) is an experimental high temperature pebble-bed reactor on industrial scale that operated in Jülich, Germany, for 21 years until 1988. A schematic overview of the reactor is shown in Fig. 1.3. The AVR was an important test reactor in which various fuel types have been irradiated. Both BISO and TRISO particles containing uranium and thorium oxide or carbide fuel. Fuel types containing thorium in dedicated particles as well as in a mixture with the uranium were tested. An important characteristic of the AVR is the location of the steam generators and the blowers inside the steel Reactor Pressure Vessel (RPV) in contrast with present HTR-10 and PBMR designs (Fig. 1.3(a)). The steam generator also serves as the decay heat removal system in case of accident situations, while in the new designs the decay heat removal system is located on the outside of the RPV.

The helium flows through the core from bottom to top, where slits and holes in the top reflector allow access to the steam generator. After passing the steam generator at the top, the cold (250 °C) helium flows downward, passing through a narrow space between the reactor barrel and the RPV. This keeps these components at a relatively low temperature. Finally, the coolant reaches the blowers at the bottom and is circulated back into the reactor core. The AVR used a second (outer) RPV for increased safety. An important feature of the AVR is that it has four so-called graphite reflector noses stretching into the pebble bed. The noses have a guiding tube for movement of control rods (Fig. 1.3(b)). It was found that the noses have a significant effect on the neutronic and thermal-hydraulic behavior of the AVR. The main effect of their presence in the pebble-bed is an increased reactivity worth and power peaking in the vicinity of the nose. Therefore, high fuel temperatures have been recorded during operation of the reactor for pebbles located near the noses [34].

A simulation of a depressurized Loss Of Flow Accident has been performed successfully, among several transient experiments, to demonstrate its inherent safety. Although the AVR initially operated at a coolant outlet temperature of 850 °C, this was subsequently raised to 950 °C. It was possible to add the pebbles either through a loading tube at the center position above the core or via four tubes located at the outside. This allowed for flattening of the radial power profile by loading of pebbles containing fertile material at the center position and fissile material on the outside.

Table 1.2: Main characteristics of relevant pebble-bed reactor designs.

Reactor	AVR	HTR-MODUL	HTR-10	PBMR
First power operation	1967	-	2000	-
Country	Germany	Germany	China	South Africa
Power [MW _{th}]	46	200	10	400
Pebble-bed diameter (in/out) [m]	0/3.0	0/3.0	0/1.9	2.0/3.7
Pebble-bed height [m]	3.0	9.4	1.8	11
Power density [MW/m ³]	2.2	3.0	2.0	4.6
Efficiency [%]	30	40	-	41
Fuel loading (enr. ²³⁵ U)	UO ₂ /(U,Th)O ₂ /C ₂	UO ₂	UO ₂	UO ₂
Enrichment ²³⁵ U [%]	10/17	8.6	17	9.6
Maximum fuel burnup (MWd/kg)	160	70	100	95
Coolant T _{in} [°C]	270	250	250	500
Coolant T _{out} [°C]	950	700	750	900
Pressure [MPa]	1.1	6.0	2.5	9.0
Thermodynamic cycle	Steam	Steam	Steam	Brayton (direct)

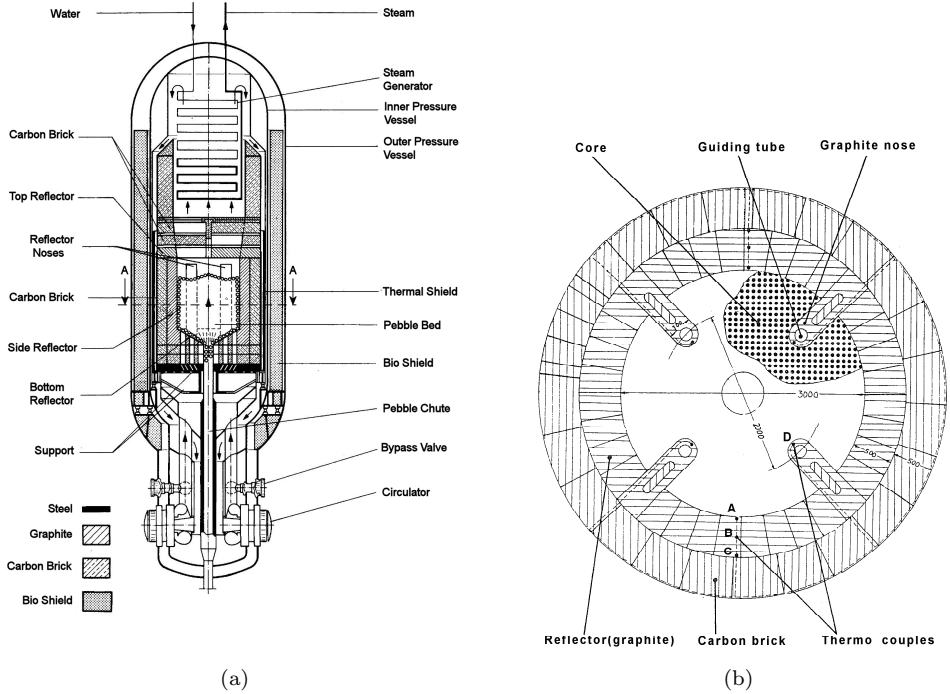


Fig. 1.3: Schematic overview of the AVR (adopted from [34]): (a) Main reactor components; (b) Horizontal cross section (A-A) of the AVR core showing the reflector noses and the positions of the thermocouples A through D.

The HTR-10

The HTR-10 reactor reached first criticality in December of 2000. Fig. 1.4(a) shows the layout of the HTR-10 and its main components [35]. The initial core was composed of a mixture of pebbles containing 5 g of 17 % enriched uranium and pebbles containing graphite only (dummy pebbles) in a ratio of 57:43 [36]. The equilibrium core contained 27,000 pebbles in total. The pebbles are added at the top of the core from a central fuel charging tube and move slowly downwards to the discharge tube below the core. Their burnup level is checked and the fuel elements which have not reached the burnup target are recirculated. This multi-pass (five passes on average) pebble scheme flattens the axial power profile.

Graphite reflectors surround the top, bottom and side of the pebble bed. The side reflector contains boreholes for the control rods, the helium cooling channels and for the absorber balls of the safety shutdown system. The direction of the coolant

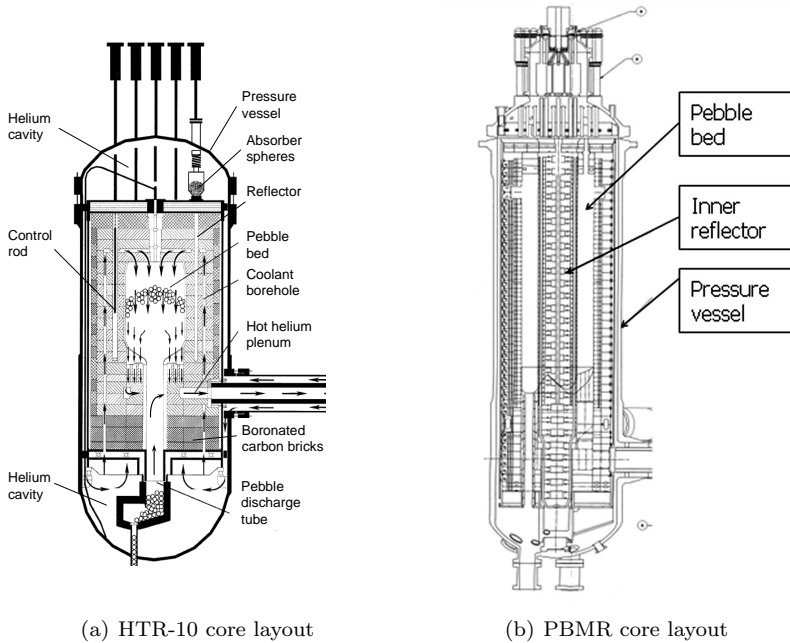


Fig. 1.4: Schematic overview of the HTR-10 (a) and (b) reactors.

flow through the reactor is noted with arrows. The helium coolant enters the reactor through the RPV and flows downward in a gap between the core barrel and the RPV, entering the bottom cavity. The main part of the helium flows from the bottom to the top of the reactor through flow paths in the bottom and side reflector and enters the helium plenum on top of the pebble bed. Part of the helium is used to cool the de-fueling chute and the control rods. Furthermore, there is a bypass flow going directly to the helium outlet plenum, without passing through the pebble bed [37]. At the top and bottom of the reactor helium cavities containing relatively cold helium ($< 250\text{ }^{\circ}\text{C}$) are located which play an important role during the transient behavior.

Boronated carbon bricks that are used as thermal insulation and neutron shielding of metallic components surround the graphite reflectors. A hot gas duct connects the reactor with the steam generator and the helium circulator that are contained in a separate vessel. The side by side arrangement of the reactor pressure vessel and the steam generator makes maintenance more convenient and reduces the probability of a core water ingress incident.

Two reactor cavity cooling systems (RCCSs) are located next to the reactor. In the absence of active cooling by the helium circulator this is the only system cooling the reactor. In this case the decay heat is dissipated from the core to the pressure vessel

by natural convection (depending on the system pressure), conduction and thermal radiation. The cavity cooling system that relies on the natural circulation of water, cools the RPV by transferring heat to air coolers outside the reactor building.

The Pebble Bed Modular Reactor (PBMR)

The Pebble Bed Modular Reactor (PBMR) is a High Temperature gas cooled Reactor that is currently being designed by the PBMR Ltd [16]. The latest core design has a thermal power of 400 MW (Fig. 1.4(b)) and contains an annular pebble bed with a fixed inner reflector. Compared to the HTR-MODUL the addition of the center reflector adds thermal inertia to the core and avoids power peaking at the core center.

Important characteristics of the reactor design are shown in Table 1.2. The 11 m tall core design contains 452,000 pebbles, which each contain 15,000 TRISO coated particles. The pebbles are used in a multi-pass pebble recycling scheme, passing the core six times on average and reaching a target burnup of >90 MWd/kg U. The fuel handling system consists of three fuel loading positions at the top and three de-fuelling tubes at the bottom.

The Reactivity Control System (RCS) consisting of 12 (B_4C) shutdown rods and 12 rods for reactor control are located in the outer reflector that surrounds the pebble-bed. A Reserve Shutdown System (RSS) can insert 1 cm diameter absorber spheres containing B_4C in boreholes in the center reflector.

The helium coolant enters the reactor through the inlet plenum in the side reflector and flows upwards in the riser channels in the reflector (Fig. 1.4(b)). The helium enters the core at the top, flows downwards through the pebble bed and flow paths in the bottom reflector. Finally, the helium exits through the outlet plenum.

Similar to the HTR-10 a reactor cavity cooling system is located next to the RPV. In contrast with the HTR-10, the PBMR utilizes a direct Brayton cycle to generate electricity instead of the Rankine (steam) cycle. The helium coolant exits the core at $900\text{ }^\circ\text{C}$ and enters the helium turbine, which drives a generator and the (low and high pressure) compressors. After the turbine, the helium passes through the primary side of the recuperator, the compressors and the secondary side of the recuperator before re-entering the core at $500\text{ }^\circ\text{C}$. To increase compressor efficiency the helium is cooled before each compression stage.

1.4 Hydrogen production methods

An (V)HTR can be combined with several chemical processes for hydrogen production (see Fig. 1.5) since it is capable of delivering heat at a maximum temperature of $750\text{-}950\text{ }^\circ\text{C}$. In this case the heat generated in the core of the reactor is transferred

1. Introduction

from the primary to a secondary loop, which utilizes the heat in either a Brayton (or Rankine) cycle for electricity production or it delivers the heat to the hydrogen production plant. The electricity generated can be utilized in the hydrogen plant or can be delivered to the electricity grid depending on the demand and the hydrogen production process.

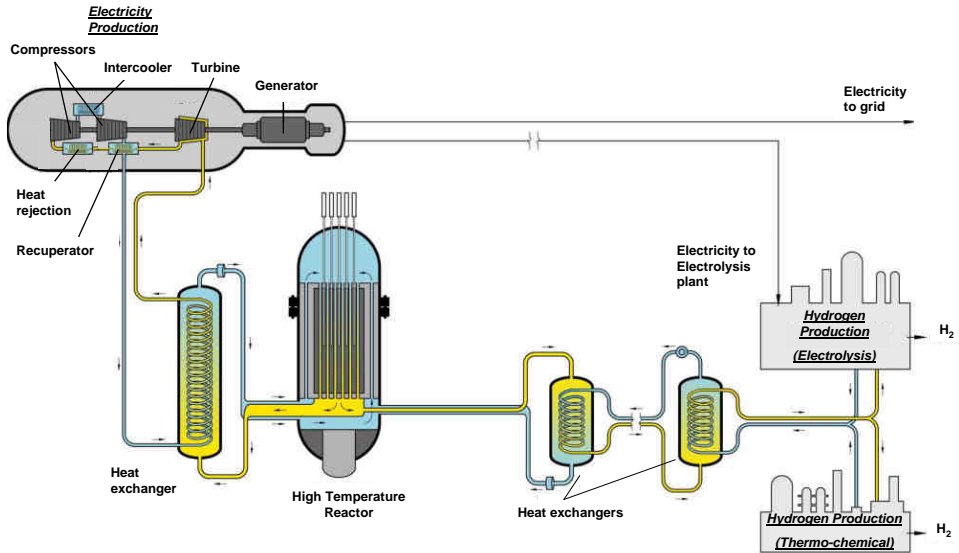


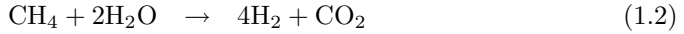
Fig. 1.5: Schematic overview hydrogen and electricity production using a High Temperature Reactor.

Today, steam reforming of fossil fuels (coal, petroleum, methane) is by far the most important hydrogen production process with a share of 96 % in the world-wide production [38]. The remaining share is produced mostly by the electrolysis of water. Together with thermo-chemical water splitting these methods are considered the most relevant options for hydrogen production that can be combined with nuclear energy. They are described in more detail in the following text.

Steam reforming of methane

Steam reforming of methane is the most important hydrogen production method today, with a share of 50% in the world-wide production [38]. In this method, steam is used to react with the methane, coming from either natural gas or bio-gas, using

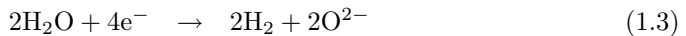
nickel as a catalyst. The two most important chemical reactions are:



Nowadays, steam reforming is used on an industrial scale at a temperature range between 500 °C and 950 °C, and pressures between 20 bar and 40 bar. The required heat for the reactions is traditionally provided by the combustion of methane, but could be replaced by another energy source, such as solar, coal or nuclear energy. Co-combustion of fossil fuels for the supply of heat produces additional CO₂ besides the steam reforming reaction itself.

Electrolysis of water

Besides methane, water can be used in electrolysis to produce hydrogen by the following electro-chemical reactions:



These chemical reactions can also proceed in the reverse direction. An example of that process is the 'combustion' of hydrogen in a (Solid Oxide) Fuel Cell. This cell consists of an anode, cathode and solid-oxide electrolyte and could in theory be used both for the production of hydrogen and for electricity generation. When operated in hydrogen production mode, steam at high temperature is dissociated at the cathode surface, thereby producing hydrogen and oxygen ions (chemical reaction 1.3). The oxygen ions can migrate through the oxide electrolyte to the anode. At the anode surface oxygen molecules are formed (chemical reaction 1.4). A voltage difference between the anode and cathode enables the transport of electrons to sustain the reactions.

The electrolysis can be performed at a wide range of temperatures (100-900 °C) with the use of steam. By operating the cell at higher temperatures the efficiency of the hydrogen production increases [39, 40]. Fig. 1.6 presents the energy demand for high temperature electrolysis ΔH , which is the sum of Gibbs energy ΔG and heat $T\Delta S$. The electrical energy ΔG per kg H₂ decreases with increasing temperature, because a larger part of the heat is used in the dissociation of H₂O. Furthermore, the increased temperature reduces the electrical resistance over the cell. This increases the overall hydrogen production efficiency from 43 % at 500 °C to 54 % at 900 °C.

Thermo-chemical water splitting

Direct thermo-chemical splitting of water in hydrogen and oxygen is only possible at temperatures in excess of 2500 °C. Over 100 possible chemical cycles have been

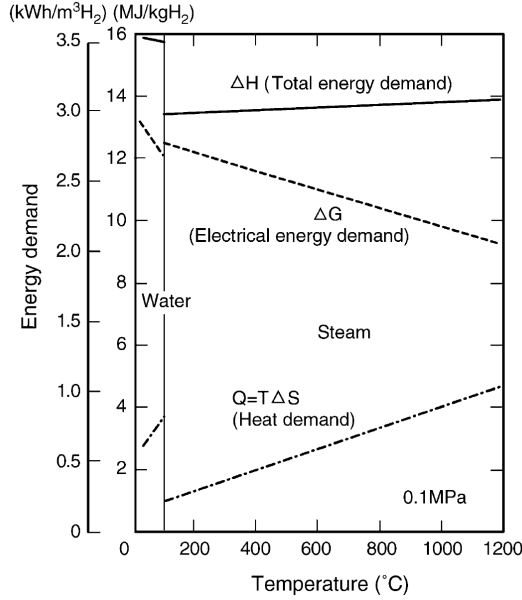
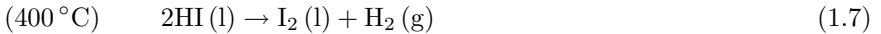
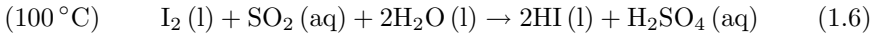
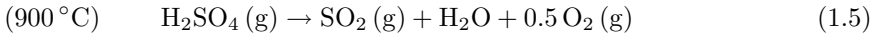


Fig. 1.6: Energy demand and its composition for high temperature electrolysis [39]. The share of electrical energy in the total energy demand decreases with increasing temperature.

proposed [41], which enable thermo-chemical splitting at lower temperatures by the use of several chemical reactions. The most promising among these cycles is the Sulfur-Iodine (S-I or I-S) cycle. The S-I cycle originates from the 1970s and research on this cycle is performed in the US, Germany and Japan. The chemical reactions of this cycle are:



A scheme of the cycle is shown in Fig. 1.7. In practice the separation of HI from the HI_x solution and the processing of H₂SO₄ complicate the presented scheme and reduce the achievable efficiency from the theoretical value of 65 % to 52 % (at 900 °C). Beside this high efficiency, compared to thermo-chemical cycles, this cycle has the advantage that the reaction at high temperature can absorb heat over a large temperature range, which can be matched with the energy source, for example the inlet and outlet temperature of the coolant of an HTR.

A lab scale plant with a maximum capacity of 30 m³ H₂/h of this cycle exists at the Japan Atomic Energy Research Institute (JAERI) [42, 43], where a stable operation of

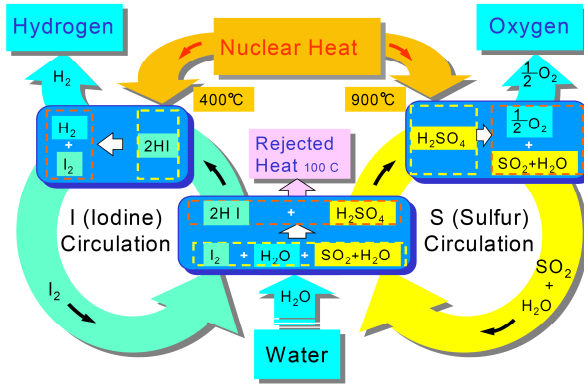


Fig. 1.7: Schematic overview of the Sulfur-Iodine (S-I) thermo-chemical process. Heat is used at two stages in the process (400 and 900 °C).

the test facility has been accomplished. The Japan Atomic Energy Research Institute is planning on building a pilot test facility in the near future [44].

Other thermo-chemical cycles that are being considered for nuclear hydrogen production are the Adiabatic UT-3 and the Cu-Cl cycle [41].

It is noted that the operating temperature of the above presented hydrogen production methods is above that of the coolant outlet temperature (280-330 °C) of a Light Water Reactor (LWR), which represents the majority of the nuclear reactors operating today.

Nuclear electricity production

The efficiency of the electricity production using heat of a nuclear reactor, which can be described in a simplified manner by the Carnot efficiency ($\eta_{Carnot} = 1 - T_{cold}/T_{hot}$), increases with the operating temperature.

Today's LWRs employ the Rankine cycle, in which steam is generated to drive a turbine that is connected to a generator. In modern Pressurized Water Reactor designs, such as the EPR, with a steam pressure of 77.1 bar an overall efficiency of 37 % can be achieved. High Temperature Gas-cooled Reactors are able to achieve higher efficiencies (>40 %) by adopting a gas turbine in the (in)direct Brayton cycle [29, 30] having reactor coolant outlet temperatures at 600-900 °C.

Although high temperatures are desirable, making use of peculiarities of CO_2 at its critical temperature and pressure, high overall plant efficiencies can be achieved at medium temperatures [45]. The critical temperature of carbon dioxide is 31.0 °C and

its critical pressure is 73.8 bar. At these conditions the compressibility factor Z exhibits a steep drop, down to $Z = 0.2$, which is considerably lower than the value of $Z = 1$ for an ideal gas [46]. This reduces the work of isentropic compression which linearly increases with Z for a real gas. Cycle efficiency can therefore be improved by designing a Brayton cycle in which the CO_2 coolant is at its critical conditions for the compression stage.

From the above it can be concluded that an HTR can produce energy at high efficiency in the form of electricity or high quality heat, which would allow for nuclear hydrogen production. A further increase in reactor operating temperature, in the creation of a VHTR, is attractive with regard to reactor efficiency.

1.5 Objective and outline of this thesis

This thesis deals with the pebble-bed type VHTR that aims at an increased helium coolant outlet temperature of 1000 °C and beyond to increase reactor performance and to allow for cost-effective production of hydrogen using nuclear energy.

The first objective of this thesis is to quantify the fuel temperature in a commercial size pebble-bed type HTR for increased operating conditions for both normal as well as accidental conditions and to predict the consequent fuel particle coating stress and its failure probability. It is expected that the intended operating conditions of the VHTR (high coolant temperature and a high fuel discharge burnup value) lead to high fuel temperatures and a consequent increase of the fuel particle failure probability.

In the previous sections it was shown that in the past high helium outlet temperatures have been achieved together with inherent safe operation in small HTRs. Scaling these designs by increasing the reactor size and the power density is attractive from economic considerations. However, this increases the fuel temperature. Therefore, the second objective of the thesis is to modify the present designs and fuel management to generate safety margins thereby mitigating problems with the increased fuel temperature and allowing for an increase of the helium outlet temperature.

It is been explained in the previous sections that in theory formation of hot spots by fresh fuel pebbles is possible and could be avoided by tailoring the loading of the pebbles depending on their burnup level. This advanced fuel management could also be used to flatten the power profile of the core. It was identified that the large pressure drop over the core could be mitigated by directing the flow radially through the core. The consequent increase in the fuel temperature can perhaps be mitigated by altering the pebble size and the pebble loading management.

This thesis is built up as follows:

- In Chap. 2 a code system for the simulation of the neutronic and thermal-hydraulic behavior of the pebble-bed reactor is described. The code system is

validated with experimental data from steady state and transient operation of the HTR-10 and AVR reactors. In a next step, the code system is applied to the PBMR design, which is chosen as the reference design for further optimization studies. A code to code comparison of the results is made and the maximum temperatures in the core during normal and transient behavior are calculated. The cause and location of the maximum fuel temperatures are identified, which serve as the guidelines for the design improvements of Chaps. 4 and 5.

- The calculated operating conditions of the PBMR from Chap. 2 are used in a fuel performance model, which is described in Chap. 3. This chapter gives a detailed description of the particle stress analysis model for the calculation of stresses in the particles coatings and surrounding graphite in the pebbles. This model is combined with a diffusion model which calculates the pressure build-up in the coated particles by gaseous fission products during irradiation in the core. Furthermore, the stress analysis model is able to take into account the presence of the graphite matrix material surrounding the fuel particles. The impact of its presence and dimensional change on the fuel coating stresses is analyzed. The models are applied to the PBMR design and the consequence of increased operating conditions on particle stresses and failure probability are analyzed.
- In the following chapter (Chap. 4) the fuel management of the reference design is optimized with the aim of reducing the fuel temperature during normal and accident situations. A fuel depletion model for the calculation of the equilibrium core composition is presented and has been used to calculate the composition for various pebble (re-)fueling strategies. In these strategies the number of pebble recycling steps and the radial reloading position are the optimization parameters. The optimal pebble refueling 'route' is searched with the aim of flattening the power profile that results in lower fuel temperatures.
- Chap. 5 proposes and investigates alternative core designs to further improve reactor performance. The incentive behind the OTTO design is to match the high temperatures in the core with low burnup pebbles in order to reduce particle stresses. Three OTTO designs with different core heights are investigated.

In an attempt to modify the power profile a conically shaped pebble-bed is adopted in a second alternative that aims at matching the power peak with low coolant temperatures.

The coolant flow direction is modified in the third alternative in order to reduce the pressure drop over the core and increase plant efficiency. It is attempted to reduce the consequent increase in fuel temperature by a combination of pebble size reduction and a optimized pebble (re-)fueling scheme. Both a one-dimensional analytical and a two-dimensional numerical investigation have been performed to calculate the temperatures in the core.

- The last chapter is dedicated to the conclusions and recommendations and is followed by the appendices. App. A gives the point-kinetic equations and the reactivity coefficients used in the PK-THERMIX model for the transient analysis of the HTR-10 presented in Chap. 2. Detailed descriptions of the neutronics code DALTON and the thermal-hydraulics code THERMIX that are used in the investigations are given in App. B. App. C presents the coefficients used in the stress analysis model of Chap. 3.

2

Validation of a neutronics and thermal-hydraulics code system for the simulation of pebble-bed reactors

In this chapter the methodology of the code system used for modeling the static and dynamic behavior of pebble-bed reactors is presented. The code system can be split up in two parts. The first focuses on the generation of nuclear data for the full-core analysis. This data is used in the second part, which is concerned with the neutronic and thermal-hydraulic analysis of the reactor. The purpose of the code is to calculate the fuel temperature for both normal and accident conditions for various reactor designs. In addition, other parameters of the core, such as the neutron flux and power profile, can be calculated for the evaluation of the fuel performance. It is expected that increasing the power, in order to elevate the coolant outlet temperature, results in an increase of the fuel temperature and consequent fuel particle coating failures.

The neutronic and thermal-hydraulic part of the code system consists of a new time-dependent (3D) diffusion code DALTON [47], described in App. B.1, which has been coupled to the existing (2D) thermal-hydraulics code THERMIX [48] (App. B.2). The followed approach for modeling the HTR dynamics is similar to other recent code systems such as PANTHERMIX [49], NEM(DORT-TD)-THERMIX [50], PEBBED-THERMIX(KONVEK) [51], PARCS-THERMIX [52], in which a diffusion (or transport code) for the neutronics is coupled to THERMIX (KONVEK/DIREKT). Other HTR dynamics codes that do not make use of THERMIX for the thermal-hydraulics are MARS-GCR/CAPP [53] and the TINTE code system [54].

By linking the DALTON-THERMIX code system (Sec. 2.2) with SCALE-5 [55] for the generation of temperature dependent neutron cross sections (Sec. 2.1), a flexible calculation tool is created for modeling and optimization of various HTR designs. The

2. Validation of a neutronics and thermal-hydraulics code system for the simulation of pebble-bed reactors

new code system is in this regard similar to the established VSOP (Very Superior Old Programs) code system [56], which also combines neutron cross section processing routines with a 2D diffusion and thermal-hydraulics model. However, the new code system is able to calculate various coupled transients, while the VSOP code cannot.

The past experience with HTR technology provides valuable information for validating codes. Experimental data concerning HTR dynamics has been obtained from the operation of the AVR. Several experiments were conducted, including a simulation of a Depressurized Loss Of Forced Cooling (DLOFC) incident in 1988 [34]. The main heat sink for the removal of the decay heat during this transient was the steam generator, which is also used during normal operation and is located above the top reflector within the RPV. In 2003 experiments were conducted on the HTR-10 reactor in China. In this 10 MW pebble-bed research reactor a Pressurized Loss Of Forced Cooling (PLOFC) and a Control Rod Withdrawal (CRW) experiments were performed. This reactor does not have a large heat sink within the RPV, but only a Reactor Cavity Cooling System with a capacity of 200 kW that is located outside the RPV. The passive removal of the decay heat by a RCCS during accident situation was proposed first for the HTR-MODUL reactor and is also adopted for modern large size designs, such as the PBMR. Unfortunately no experimental data is available for large size pebble-bed reactor designs that use this decay heat removal principle, which was demonstrated in the HTR-10. However, an international benchmark calculation has been organized by the NEA/OECD for steady state and dynamic behavior of the 400 MW PBMR design.

Therefore, it was chosen to validate the code system against both the pressurized transient of the HTR-10, which contains the modern decay heat removal system, and the depressurized transient of the AVR. Results are presented in Secs. 2.3 and 2.4, respectively. In a second step, the behavior of the PBMR-400 core design during normal and D\PLOFC transients is analyzed in Sec. 2.5. The temperature, power and flux profiles during normal operation determine the irradiation conditions of the fuel and serve as the boundary conditions of the fuel performance model described in Chap. 3. From these results possible improvements of the PBMR-400 design in order to reduce the fuel temperature or allow for an increase of the helium outlet temperature are identified and explored in Chaps. 4 and 5.

2.1 Neutron cross section calculation procedure

For the simulation of the HTR-10 transients both a point kinetic model [57] with externally calculated reactivity coefficients has been used, as well as a 2D model in DALTON with space and temperature dependent neutron cross sections. The calculation procedure for the reactivity coefficients and cross sections for both the HTR-10 and AVR reactors are similar. It uses several modules of the SCALE-5 code system [55] in order to take into account the double heterogeneity of the fuel (TRISO

and pebble) and the geometry of the reactor. The calculation steps are as follows:

1. First, the TRISO particles in the graphite matrix are modeled by using the CSASIX module of SCALE-5. In this module, the NITAWL-III [58] and BONAMI [59] modules are used for the evaluation of the resolved and unresolved resonances which are treated by the Nordheim Integral Method and the Bondarenko method, respectively. A one-dimensional discrete ordinates transport calculation using XSDRNPM [60] is made of a fuel kernel surrounded by cladding (material from the carbon buffer, IPyC, SiC and OPyC layers) and moderator (graphite) material (see Fig. 2.1). The moderator volume having radius R_0 is equal to the volume of the fuel zone of the pebble divided by the number of TRISO's. From this last calculation homogenized neutron cross-sections are made for "TRISO material". For this purpose a 172 energy group (XMAS) library is used, based on the JEFF2.2/3.0 and JENDL3.3 libraries and processed with NJOY. To account for the fuel-shadowing effect of the fuel kernels in the graphite matrix of the pebbles a Dancoff factor is used, which is analytically determined [61] and is a function of the number of fuel particles and the radii of the kernel, the fuel zone and the pebble.

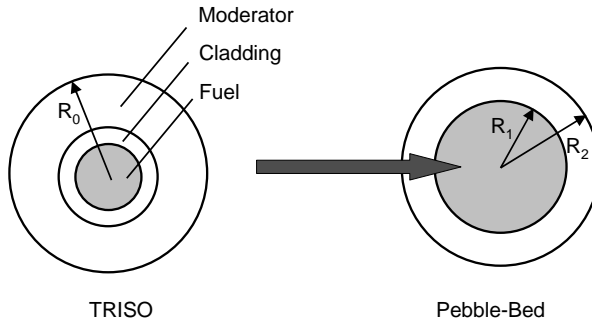


Fig. 2.1: *TRISO and Pebble model used in calculation of homogenized cross sections for the pebble bed region.*

2. The homogenized neutron cross sections for the TRISO material are used in a one-dimensional transport (XSDRNPM) calculation in which a sphere of TRISO material, with radius R_1 , is surrounded by a layer of graphite and helium with radius R_2 (see Fig. 2.1). In this calculation R_1 is equal to the fuel zone in the pebble and R_2 can be calculated from the packing fraction ψ ($=0.61$) and the ratio of moderator to fuel pebbles, f , by the following relation:

$$R_2 = \sqrt[3]{R_{peb}^3 \frac{1+f}{\psi}} \quad (2.1)$$

2. Validation of a neutronics and thermal-hydraulics code system for the simulation of pebble-bed reactors

If no moderator pebbles are present f equals zero. In the case of the HTR-10 $f = 43/57$ and since the fuel zone of the pebble is 2.5 cm and the pebble outer radius is 3 cm, a value of 4.26 cm is found for R_2 .

This transport calculation results in homogenized cross sections for "pebble-bed material".

3. As a last calculation step several one-dimensional transport calculations, representing a certain axial or radial cross section of the core, are performed. In general the geometry consists of a pebble bed region surrounded by graphite reflector regions. These regions are split up into several zones to generate zone weighted few group cross sections. In order to model the transverse neutron leakage in these 1D calculations the reactor height (or width) is supplied from which a buckling factor is derived. The zone weighted cross sections of these 1D calculations are allocated to the positions of the corresponding material in a 2D cross section map.

The above described procedure is repeated for several fuel and moderator temperatures resulting in a 2D temperature dependent cross section library. Directional dependent diffusion coefficients are calculated with an analytical solution [62] to treat the void regions in the core, such as the helium plenum above the pebble-bed. Regions containing the control rods are treated in a separate CSAS run representing a horizontal cross section of the rod and surrounding material (graphite and pebble-bed). The resulting cell weighted cross sections are transformed to a 'grey curtain' region for the 2D (r-z) cross section map by conservation of the neutron absorption reaction rates.

For the HTR-10 benchmark both reactivity coefficients as well as zone weighted cross sections have been calculated with the above procedure for a point kinetic model (see Appendix A) and 2D model in DALTON, respectively.

For the AVR benchmark, zone weighted cross sections with collapsed energy group structure could be generated using the last calculation step (3). However, it is chosen to omit this step, because the AVR core contains many different pebble types (9) and burnup classes (49). Instead, the homogenized pebble cross sections of the different fuel and pebble types of step (2) are mixed according to their presence in several core regions, while the collapsed group structure contains a relatively large number (9) of energy groups, with upper energy boundaries [63] at 19.64 MeV, 0.183 MeV, 0.914 keV, 19.64 eV, 4.0 eV, 2.36 eV, 0.40 eV, 0.1 eV and $4.2 \cdot 10^{-2}$ eV.

2.2 Coupled DALTON-THERMIX code system

In Fig. 2.2 a schematic overview of the coupled code system is presented. The coupled code system consists of the codes DALTON and THERMIX that are described in detail in Appendix B and several other codes and scripts. A description of each

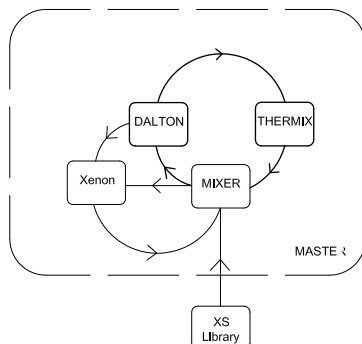


Fig. 2.2: Schematic overview of the coupled code system

component of the system is given below:

DALTON The DALTON code can solve the 3D multigroup neutron diffusion equation on structured grids (xyz or $rz\theta$ coordinates) (see App. B.1). DALTON calculates a 2D zone averaged power profile using neutron cross sections that have been obtained through interpolation using the local temperature and xenon concentration. In the case that the point kinetic equations are used, a fixed power distribution is scaled to the calculated total power.

THERMIX THERMIX(-DIREKT) [48] is a 2D thermal hydraulics code that consists of the two modules THERMIX (heat conduction and thermal radiation) and DIREKT (convection) (see App. B.2). The new power profile is used in THERMIX to calculate the temperature profile in the reactor at the new time point. For the core region two-dimensional temperature profiles for fuel and moderator temperatures of the pebbles are calculated. To this end a one-dimensional calculation for the temperature profile inside the pebbles is used, taking into account that the pebbles have a fuel free (graphite) zone in the outer (0.5 cm) shell.

XS library Before the thermal hydraulic and neutronic calculations are started, a neutron cross section (XS) library is created as a function of the fuel and moderator temperatures and the xenon concentration. In the case of the PBMR-400 benchmark the cross sections were supplied as part of the benchmark description and also depend on the local fast and thermal buckling.

Xenon The xenon concentration is determined using the well known simplified depletion chains for xenon and iodine [12].

MIXER An in-house perl script (MIXER) updates for each calculation step the neutron cross sections by linear interpolation using several routines of the SCALE code system [55].

MASTER Depending on the type of transient the MASTER program decides how

2. Validation of a neutronics and thermal-hydraulics code system for the simulation of pebble-bed reactors

often data is exchanged between the different codes and what the calculation mode type of the codes has to be, i.e. steady state (eigenvalue) or transient mode.

Time step control and calculation mode

For transient calculations DALTON and THERMIX are used consecutively without performing additional iterations. The time step control within the codes is done independently of each other. The (global) time step can be chosen manually or with a control algorithm that ensures convergence and stability of the coupled calculation result. The algorithm that was adopted is similar to the time step control in DALTON described in Sec. B.1. Following Eq. (B.8), the criterion for a time step to be accepted or not depends on the maximum allowable absolute error, ATOL, and relative error, RTOL, as supplied by the user. However, instead of the neutron flux ϕ_i that is used in Eq. (B.8), a vector \mathbf{y} containing N state variables is used to check the 'global' time step and predict the new step size. A restart of the coupled code system from the previous time point is required if the criterion is not met. The vector \mathbf{y} contains the following variables: the average helium temperature, the average fuel temperature and the total reactor power.

The calculation mode type can be adjusted for certain transient simulations, such as the Loss Of Forced Cooling Accident with or without the insertion of the control rods (SCRAM), in which the reactor is in a sub-critical condition for a long period in which the fission power is negligible. In these cases a THERMIX stand alone calculation is performed combined with an eigenvalue calculation in DALTON up to the point of re-criticality, when the calculation mode is switched back to fully coupled dynamics. At this point the flux and precursor level are normalized to a low power level, e.g. 1 W.

2.3 Simulation of the HTR-10

Apart from the calculation of the initial criticality and normal operation of the HTR-10 two transient cases are investigated, namely: a simulation of a Pressurized Loss Of Forced Cooling (PLOFC) and a Control Rod Withdrawal (CRW), which also leads to the shut down of the blower and consequent shut down of active core cooling. These cases can be considered as one of the most demanding transients in a nuclear reactor and were performed in the HTR-10 to demonstrate the inherent safety characteristics of a pebble-bed reactor using only the reactor cavity cooling system as an active heat sink. Results of calculations made with both THERMIX coupled to a point-kinetics model (PK-THERMIX) and a coupled 2D DALTON-THERMIX model are compared with experimental data from the HTR-10 reactor.

Initial criticality and normal operation

The initial core was composed of a mixture of pebbles containing 5 g of 17 % enriched uranium and pebbles containing graphite only (dummy pebbles) in a ratio of 57:43 [36]. The pebble discharge tube and the bottom cone-shaped part of the core region were filled with dummy pebbles. A mixture of the fuel and dummy pebbles was added to the core at room temperature until criticality was reached. Criticality was reached after adding 16890 mixed pebbles at 15 °C corresponding to pebble-bed height of 123 cm at 27 °C [36].

After the initial criticality was reached in December 2000 additional fuel and dummy pebbles were added to the core in order to maintain criticality at hot conditions. In the following 820 Equivalent Full Power Days (EFPDs) a mixture of fuel pebbles is added, while the dummy pebbles that filled the entire bottom region of the core are discharged [64]. After this period, fresh fuel pebbles are added to the core in combination with recycling of fuel pebbles. It is therefore assumed that the core, when the transient test were performed in October 2003, consisted of a combination of fuel pebbles having a certain burnup value and dummy pebbles.

The point of criticality has been calculated with the cross section procedure of Sec. 2.1 combined with a 2D calculation for a fixed temperature of 27 °C. The cross section generation procedure predicted a k_{∞} of 1.7625 for the pebble-bed material (see Fig. 2.1), which is close to the value of 1.76155 calculated with TRIPOLI [65]. For a pebble-bed height of 108 cm and 126 cm DALTON predicts a k_{eff} of respectively 0.9698 and 1.0268, which leads to a critical height of 117 cm (TRIPOLI, $H_{crit} = 117.4$ cm). It is expected that the treatment of the void regions for the movement of the control rods and the absorber balls, which were modeled by reducing the density of the graphite in those areas, leads to an underestimation of the neutron streaming effects and therefore in an overestimation of the k_{eff} .

In the coupled DALTON-THERMIX calculations it was assumed (see Sec. 1.3) that the entire discharge tube was filled with a mixture of fuel and dummy pebbles and that the fuel in the core has an homogeneous average burnup value. Furthermore, it is assumed that the control rods remain in the upper position. This leads to an k_{eff} of 0.9497 and 1.0132 at burnup values of 8.5 % and 6.8 % FIMA, respectively, for a coupled DALTON-THERMIX calculation.

The results of the temperatures (FIMA = 8.5 %) at specific locations in the core (Fig. 2.7, [66]) of a coupled calculation are presented in Table 2.1. It is noted that there is an uncertainty in the specific location of the thermocouples. Furthermore, the 2D model in THERMIX does not capture the 3D effects, which are especially important in the region of the side reflector which contains the holes for the control rods and absorber balls. This can explain the differences in the calculated and measured temperatures.

2. Validation of a neutronics and thermal-hydraulics code system for the simulation of pebble-bed reactors

Table 2.1: Temperatures at several locations (Fig. 2.7) in the HTR-10 calculated with DALTON-THERMIX and measured during operation.

Location	Experiment [°C]	DALTON-THERMIX [°C]
Top reflector	230	242
Side reflector	460	457
Metal support structure	180	194
Outlet mixing room	810	810

Simulation of the PLOFC transient

The PLOFC simulation is initiated by shutting down the primary helium blower during steady state operation of the reactor. As a result the helium flow in the primary loop is stopped and the reactor is isolated from the water cooling systems on the secondary side of the steam generator. For calculation purposes, it is assumed that the helium flow reduces linearly within 12 seconds [67].

For both the PLOFC and the CRW simulations the reactor conditions and assumptions were as follows:

- The reactor has reached steady state operation at partial load of 30% of full power, i.e. 3 MW at the start of the transient in both the calculation model and in reality.
- It is assumed that the primary helium pressure at steady state partial load operation is 2.5 MPa and remains unchanged during the transient. In reality it was found that the pressure reduces slowly to 2.4 MPa in 2.8 hours [68].
- The measured helium temperatures at reactor inlet and outlet are 215 °C and 650 °C respectively at steady state partial load operation were adopted in the THERMIX model. Helium flow rate is defined by this temperature difference and the helium pressure.
- The control rods remain at fixed (upper most) position in the DALTON model. The reactivity insertion by rod movement in the CRW simulation is simulated by rescaling the fission source in DALTON and introducing an external reactivity in the PK model. The power density distribution is assumed to be fixed.
- The temperature at the radial side boundary, where the decay heat removal system is located, is set to a fixed temperature of 50 °C in THERMIX, while the top and bottom concrete structures surrounding the air cavity in which the reactor is placed was set to 35 °C. This corresponds to the average water temperature in the decay heat removal system which operated at 206 kW cooling power.
- The dummy pebbles were not modeled explicitly in THERMIX. Instead, all pebbles were assumed to be fuel pebbles having a reduced thermal conductivity, which was weighted with the fuel to dummy pebble ratio.

- Reactivity coefficients resulting from a DALTON-THERMIX calculation were used in the PK model. The following coefficients were used for the fuel, moderator and reflector, respectively: $\frac{d\rho_{fuel}}{dT} = -8.16 \cdot 10^{-5} \text{ K}^{-1}$, $\frac{d\rho_{mod.}}{dT} = -9.15 \cdot 10^{-5} \text{ K}^{-1}$ and $\frac{d\rho_{refl.}}{dT} = 6.41 \cdot 10^{-6} \text{ K}^{-1}$.

The calculation and experimental results for the PLOFC are presented in Figs. 2.3, 2.4 and 2.5. It can be seen that the helium mass flow reduction causes the tempera-

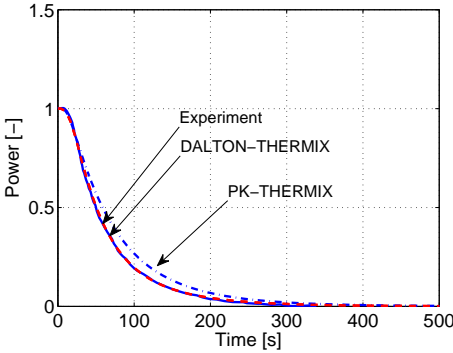


Fig. 2.3: Reactor (fission) power during the first 500 seconds during of the PLOFC transient in the HTR-10 measured during the experiment and calculated with the PK-THERMIX and the (2D) DALTON-THERMIX models. It is noted that the DALTON-THERMIX and experimental results are almost identical.

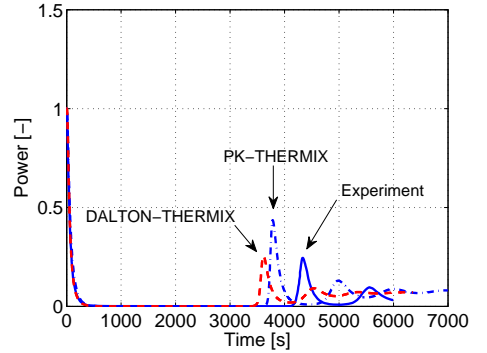


Fig. 2.4: Reactor (fission) power during the entire calculation domain of the PLOFC transient in the HTR-10 measured during the experiment and calculated with the PK-THERMIX and the (2D) DALTON-THERMIX models.

tures of the fuel and moderator to increase, resulting in a negative reactivity feedback caused by increased resonance absorption (Doppler effect) in the fuel and the shift in thermal spectrum caused by the moderator temperature feedback. Feedback from the reflector temperature is small, since the average change in reflector temperature in the beginning of the transient is small. The feedback results in a fast reduction of the fission reactor power and within 500 s the reactor power is determined by the decay heat power only (See Figs. 2.3).

During the transient, natural convection flows enable relatively cold helium from the helium cavities located inside the RPV on top and below the core (see Fig. 1.4(a)) to enter the bottom region of the core. Furthermore, the natural convection flow transports heat from the bottom to the top of the core. The above described effects cause the bottom of the core to cool down while the top is heated up, which can be seen from the calculated temperature profiles of the solid structures at the beginning and the end of the transient (Figs. 2.6(a) and 2.6(b)). The temperature at specific

2. Validation of a neutronics and thermal-hydraulics code system for the simulation of pebble-bed reactors

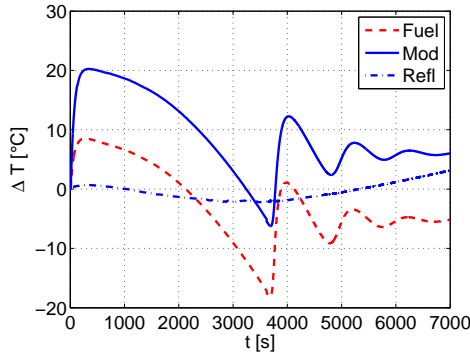


Fig. 2.5: Difference in the Fuel, Moderator and Reflector temperatures compared to values at normal operating conditions used in the PK - THERMIX model to determine the temperature reactivity feedback.

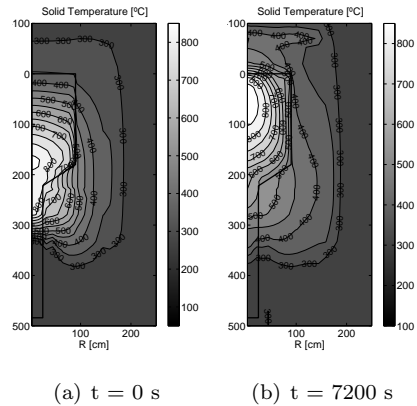


Fig. 2.6: Temperature profile of solid structures at the beginning (a) and end (a) of the PLOFC transient in the HTR-10.

positions (see Fig. 2.7) in the reflector, the core outlet and bottom support structure were recorded during the experiment [67]. It was found that the largest temperature difference between the beginning and end of the transient was found for the top reflector region, namely +215 °C. Temperature differences in the side reflector were relatively small, but a large decrease of the temperature by 315 °C was recorded for the core outlet (located next to the pebble de-fueling chute). Fig. 2.8 shows that both the trend and total temperature differences of the calculated results from THERMIX for these points are in agreement with the measured temperature.

According to the measurements, the bottom part of the core has cooled down sufficiently to reach criticality again and after 4200 s the core is generating a significant amount of fission power (see Fig. 2.4) according to the measurement. This results in an increase of the power and corresponding rise in fuel and moderator temperature. The increase of fuel and moderator temperature results again in negative reactivity feedback, which causes the reactor power to come down again. This oscillatory behavior occurs several times until a quasi-stationary situation is reached at elevated temperatures at a low reactor power, which is equal to the power of the decay heat removal system (206 kW) [67].

Both the PK-THERMIX and the DALTON-THERMIX models show similar trends in power and temperature as the measured data. Some differences between the codes and the experiment can be identified:

- The point of re-criticality predicted by the DALTON-THERMIX and PK-THERMIX model occurs ~ 700 and 500 seconds, respectively, before the measured time point. The location of the point depends on the temperatures in

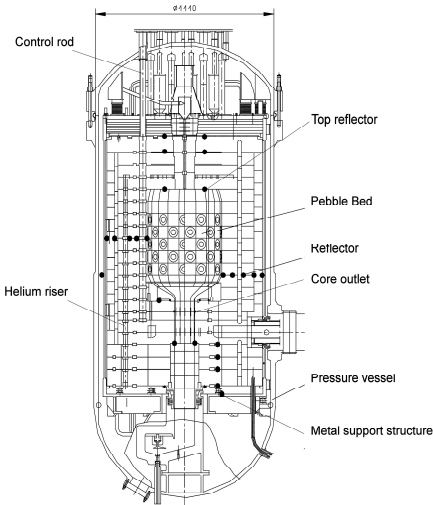


Fig. 2.7: Schematic overview of the HTR-10 reactor design showing measurement points for the top reflector, core outlet and metal support structure.

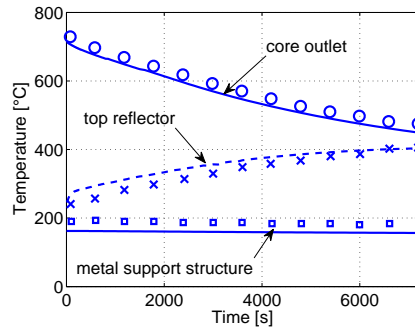


Fig. 2.8: Temperature during the PLOFC transient of the top reflector, core outlet and metal support structure. The measured data is shown by the markers, while the solid lines show the calculated results.

the core and their corresponding temperature reactivity feedback. The heat transfer from the core to the reactor cavity cooling system and the thermal capacity determine the temperature in the pebble-bed. It was found that the heat transfer to the cooler is overestimated by several percent at the end of the transient (6000 s). This results in a faster cooling down of the core and a higher power level at the end of the transient (Fig. 2.4) than in reality.

Furthermore, the build up of the ^{135}Xe concentration in the fuel will result in a negative reactivity feedback effect, which will delay the time point of re-criticality. This latter effect was not taken into account in the calculation models. It is therefore expected that including this effect will bring the point of re-criticality of the calculated results closer to the measurement.

- The maximum fission power after re-criticality, which equals 24.5% of the initial fission power according to the measurement, is better predicted with the DALTON-THERMIX model (25.5%) than with the PK-THERMIX model (43.5%). This can be attributed to the detailed neutronics (2D) model in the DALTON-THERMIX compared to the simplified point kinetic model in PK-THERMIX.
- The power oscillations after re-criticality in DALTON-THERMIX have a shorter period than the measurements indicating that the feedback in the DALTON-

2. Validation of a neutronics and thermal-hydraulics code system for the simulation of pebble-bed reactors

THERMIX is stronger than in reality. The oscillations are dependent of the fuel and moderator temperatures and their corresponding temperature reactivity effect. These temperatures are mainly dependent on the thermal capacity of the graphite in the pebbles. The reduced time period of the oscillations can therefore be sought in an underestimation of the thermal capacity or an overestimation of the temperature reactivity effect of the fuel and moderator in the DALTON-THERMIX model.

Control Rod Withdrawal without SCRAM

In a second experiment the loss of flow is combined with a withdrawal of a control rod. The transient is started (time point zero) by withdrawing one control rod at operational speed introducing positive reactivity [67], see Fig. 2.9. After 12 seconds, the reactor protection system was initiated by the signal "power increasing rate exceeds 3.5 %/s". This system shuts down the helium blower, but because of its mechanical inertia the speed of the blower only reduces gradually [67] to zero. At the same time a flapper valve is closed to isolate the reactor from the rest of the primary loop.

The mass flow through the core was not recorded during the transient. Therefore, it is assumed that after the initiation of the reactor protection system, the mass flow is reduced linearly and is completely stopped at $t = 80$ seconds, which corresponds to the reduction in the helium blower speed.

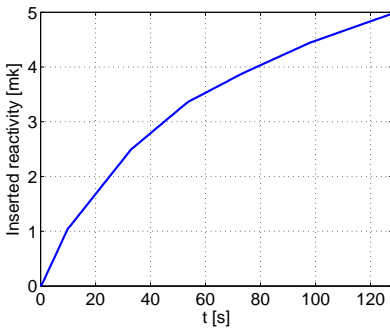


Fig. 2.9: *Inserted reactivity by control rod withdrawal.*

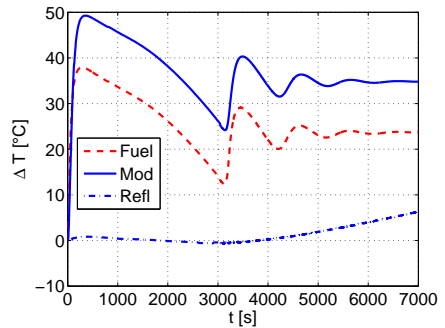


Fig. 2.10: *Difference in the Fuel, Moderator and Reflector temperatures compared to values at normal operating conditions used in the PK - THERMIX model to determine the temperature reactivity feedback during the CRW transient.*

The temperatures and the fission power during the first 500 seconds of the experiment are shown in Figs. 2.10 and 2.11(a), respectively. The insertion of positive

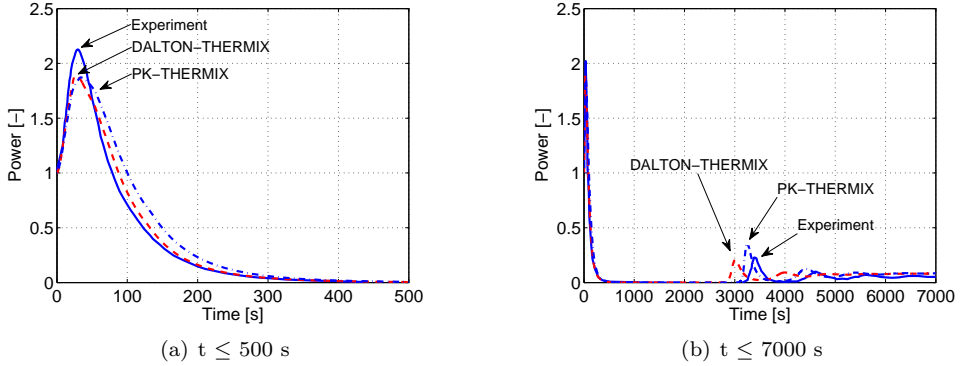


Fig. 2.11: Reactor (prompt) power of the HTR-10 during the Control Rod withdrawal transient of the HTR-10 during; (a) the first 500 seconds; (b) the entire time domain.

reactivity by the control rod withdrawal results in a rapid increase of the reactor power during the first 30 seconds of the transient. The increase in fuel and moderator temperature causes a negative temperature feedback, which is stronger than the reactivity added by the control rods, and within 500 seconds the contribution of the fission power the total reactor power is negligible. Criticality is reached again (see Fig. 2.11(b)), after sufficient cooling down of the core, similar to the core behavior during the PLOFC transient.

Although the shape of the power history is similar for the first 500 seconds of the transient, the maximum value reached is significantly lower for the PK-THERMIX (187 % of the initial fission power P_0) and the DALTON-THERMIX (1.89 P_0) calculation compared to the measured value (2.13 P_0). It was found that the maximum power reached is sensitive to the time point at which the mass flow reduction is initiated and the mass flow reduction rate. The uncertainty in their exact values could explain the difference between the calculated and experimental results.

Similar to the PLOFC transient, the calculated point of re-criticality occurs (250 seconds for DALTON-THERMIX) before the measured time point and the maximum power reached after this time point is 22 % of the initial power for DALTON-THERMIX and 36 % for PK-THERMIX compared to the measured 23 %. Similar to what was found for the PLOFC transient the point-kinetic results are in agreement with the DALTON and experimental results at the beginning of the transient. However, at the point of re-criticality the temperature and power profiles have changed significantly as compared to their shapes at nominal conditions. Therefore, the (2D) DALTON results are in better accordance with the experiments than the point-kinetic results.

2.4 Simulation of the AVR

A Depressurized Loss Of Forced Cooling incident (DLOFC) simulation was performed in the reactor in 1988 [34]. It is expected that the increase in core temperature under this depressurized conditions is larger than the pressurized PLOFC case that was simulated in the HTR-10. In contrast with the HTR-10, which contained only a single fuel type apart from the graphite-only pebbles, the AVR core was composed of several pebble and fuel types at various burnup levels.

The behavior of the AVR has been simulated with the DALTON-THERMIX code system as a second validation step next to the simulation of the HTR-10. A coupled steady state calculation has been performed to determine the initial conditions for the DLOFC transient, which has been simulated with a THERMIX stand-alone calculation.

Description of the DLOFC experiment

The DLOFC experiment was intended to simulate the reactor losing forced cooling and system pressure in full load condition. However, a fast depressurization could not be performed for practical reasons. Alternatively, the helium was pumped into the storage vessel by the gas purification system in three days. In Table 2.2 the main operating conditions of the AVR during full power operation and before the start of the DLOFC simulation are presented. Note that depending on the speed of the helium blowers the AVR could be operated with an helium outlet temperature between 810 and 950 °C.

Table 2.2: *Main operating conditions of the AVR at full power and at the start of the DLOFC experiment.*

Parameters	Full power	DLOFC	Unit
Thermal power	46	4	MW
Helium coolant			
Pressure	10.8	1.0	bar
Mass flow	16.3/12.7	1.5	(kg/s)
Inlet temperature	275/250	183	(°C)
Outlet temperature	810/950	810	(°C)
Steam generator			
Inlet temperature	110	130~60	(°C)
Mass flow (water)	56	25~20	(t/h)

First, the reactivity of the core was lowered by stopping the input of new fuel pebbles. This allowed for only a partial insertion of the control rods during the test, which guaranteed that the power distribution is similar to that of the full load

conditions. Then, the reactor was operated for some days at low power level (4 MW) until the full load (46 MW) temperature distribution was obtained. The main operating conditions of the AVR during normal and at the start of the transient are given in Table 2.2. The temperatures of the main components are shown in the second column of Table 2.3. Finally, the DLOFC transient was initiated by a shut down of the helium blowers, whereby the forced cooling of the reactor was stopped. The decay heat curve for full load conditions (46 MW thermal power) was simulated with the fission power by moving the control rods. The steam generator operated at about 50 percent of full mass flow during the entire DLOFC experiment and the water inlet temperature decreased from 130 °C to 60 °C.

Table 2.3: *Temperatures from measurements and a DALTON-THERMIX calculation of the AVR reactor a steady state power level of 4 MW before the start of the transient.*

Location		Experiment (°C)	Calc. (°C)
Side reflector:	Point A (Fig. 1.3(b))	553	562
	Point B (Fig. 1.3(b))	545	545
	Point C (Fig. 1.3(b))	535	528
Reflector nose:	Point D (Fig. 1.3(b))	608	592 ⁽¹⁾
Bottom reflector		207	209
Reactor barrel		276	276
Inner RPV:	axial center	189	180
Top of reactor		196	192
Discharge tube		198	188

Note: (1) surface temperature of the pebble nearest to the measurement point

Simulation of the initial conditions of the DLOFC experiment

A coupled steady state calculation of the reactor at 4 MW power has been performed using a coupled DALTON-THERMIX calculation. The succeeding transient, which is discussed in the next section, was calculated using a THERMIX standalone calculation, since the power profile is assumed to be fixed and the decay heat power was simulated by the movement of the control rods. This also prohibits the reactor to become subcritical by negative temperature feedback after shut down of the blower, and no re-criticality occurs as was seen for the HTR-10. The reactor power as recorded during the experiment has been provided to THERMIX.

A 9 energy-group structure was adopted for a 3D ($rz\theta$) calculation in DALTON. This relatively fine group structure was chosen to take into account the various fuel regions (139), pebble types (9) and burnup classes (49), while avoiding 1D transport calculations in the cross section generation procedure (see Sec. 2.1). Fig 2.12(b) shows

2. Validation of a neutronics and thermal-hydraulics code system for the simulation of pebble-bed reactors

the resulting fast and thermal fluxes at the axial center of the core. The influence of the graphite noses can be seen. The peaks of the thermal flux appear in the graphite noses, while the fast flux is depreciated in these areas. The peaks of the fast flux appear in the region which contains a high fissile nuclide concentration in the zones surrounded by the reflector noses and side reflectors. Note that at this axial position no control rods are present in the guiding tubes of the graphite noses. The 3D power

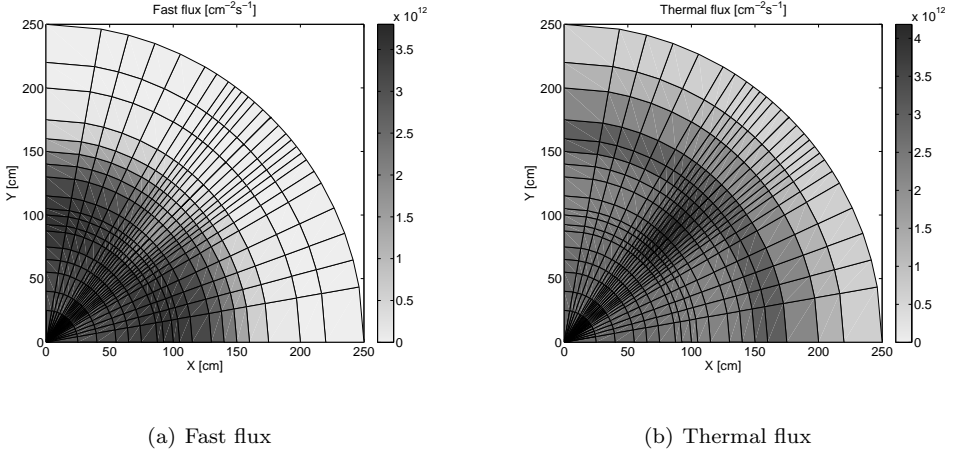


Fig. 2.12: Fast and thermal flux of the horizontal cross section ($0 \leq \theta \leq \frac{\pi}{2}$) of the AVR shown in Fig. 1.3(b), showing the impact of the reflector noses.

profile is averaged in the azimuthal direction to generate a 2D profile (see Fig. 2.13) for use in THERMIX. The power peak appears in the top-right region of the pebble-bed. The main reasons for this are the presence of the reflectors and noses near the outer region and the use of different fuel pebbles for the center region and the outer region of the core. Fig. 2.14(a) shows the temperature distribution of the reactor at the beginning of the transient. The position of the maximum temperature appears on the top, outside of the core. It is determined by the corresponding power density and the mass flow distribution in the reactor. The third column in Table 2.3 gives the calculated temperatures of the reactor, which are in good agreement with the experimental results shown in the second column of the table.

Simulation of the transient behavior of the DLOFC experiment

The transient of the DLOFC experiment was initiated by shutting down the helium blowers. As a result, this stops the heat removal by forced convection from the core and the temperature reactivity feedback causes the fission reactor power to reduce

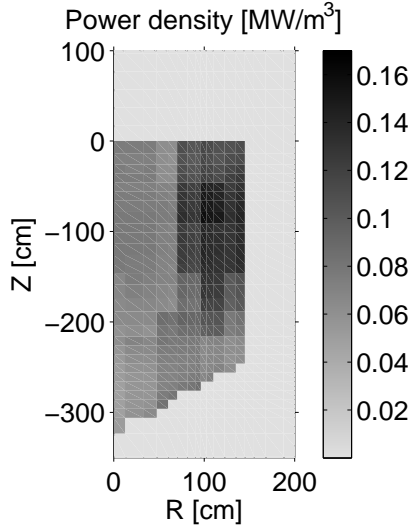


Fig. 2.13: *The 2-D power density profile in the AVR reactor core.*

quickly to zero. From this point, conduction, radiation and local natural convection all become important contributors to the decay heat removal from the core to the steam generator, which remains the main heat sink during the DLOFC transient. Although it is commonly considered as unimportant in a low pressure system, natural convection did contribute to the heat transfer in the AVR during the DLOFC experiment [34]. It was found that the natural convection was underestimated in the 2D THERMIX model, since the complex 3D geometry of the top region of the core could not be modeled explicitly. In order to simulate this local natural circulation, a very small artificial mass flow of 0.02 kg/s is applied in the model based on a detailed investigation of the natural convection flows in the AVR [69, 70].

Since the upward forced cooling flow is absent, the bottom and middle section of the core start to heat up by the decay heat while the steam generator is mainly cooling the top region of the reactor. Therefore the maximum temperature in the pebble-bed moves from outside-top to the center-middle. This can be recognized when comparing the temperature profile at the beginning of the transient (Fig. 2.14(a)) with the profile 50 hours after the start of the transient (Fig. 2.14(b)). With the reduction of the decay heat over time the cooling of the steam generator starts to dominate the heat balance and after 30 hours in the transient the entire core starts to cool down.

Figs. 2.15(a)-2.15(d) illustrate the temperatures of the side reflector in the axial center of the reactor core. Their positions are shown in Fig. 1.3(b) as points A through D. The temperatures of the side reflectors increase at the beginning of the transient

2. Validation of a neutronics and thermal-hydraulics code system for the simulation of pebble-bed reactors

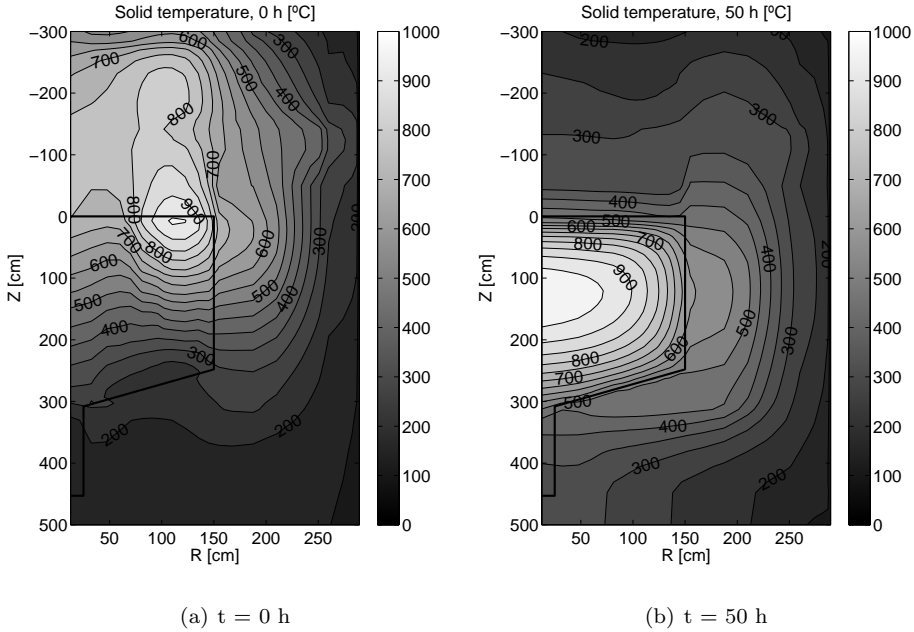


Fig. 2.14: Temperature profile of the solid structures at the start of the transient (a) and after 50 hours (b).

because of the absence of forced cooling and the consequent accumulation of the decay heat. The side reflectors reach the maximum temperature after about 16-22 hours for both the experimental and calculation results. Then, the reactor gradually cools down, discharging the heat to the steam generator and the outer reactor pressure vessel by conduction, radiation and natural circulation.

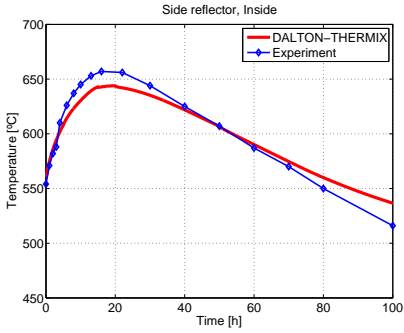
The reflector noses stretch into the pebble-bed and therefore the temperature of the tip of the nose is close to the temperature of the pebbles at this radial position during steady state operation. Fig. 2.15(d) shows the calculated surface temperature history of a pebble at this position and the measured temperature of the nose tip. It can be seen that their temperature histories follow the same trend, but that the experimental value for the nose tip is significantly lower than that of the calculated value for the pebble-bed. The difference shows that predicting the temperature of the nose region is difficult using a 2D model, in which the nose is not explicitly modeled. The 2D model does not take into account that the nose has a conductivity that is almost a factor 10 higher than that of the pebble-bed and that no decay heat is generated in the nose.

The trend of the temperature history of the bottom reflector (Fig. 2.15(e)) is some-

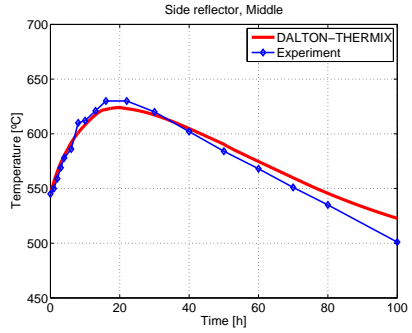
what different from the side reflectors, since it is located further away from the final heat sink, i.e. the steam generator. Its temperature increases with almost 300 °C and only slightly decreases in temperature after 70 hours.

The maximum temperature in the pebble-bed measured by pebbles with a measuring device was between 1070 and 1090 °C. The calculated maximum fuel temperature was 1041 °C and is located at the core center after 25 hours. For this location this is an increase of 500 °C compared to the initial temperature. Fig. 2.14 shows the change in the temperature profile of the AVR during the transient.

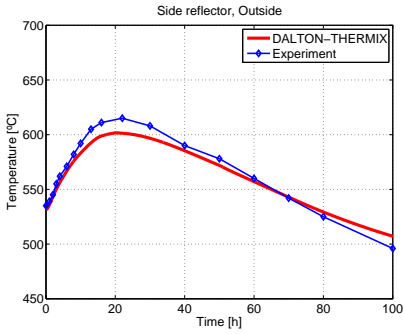
2. Validation of a neutronics and thermal-hydraulics code system for the simulation of pebble-bed reactors



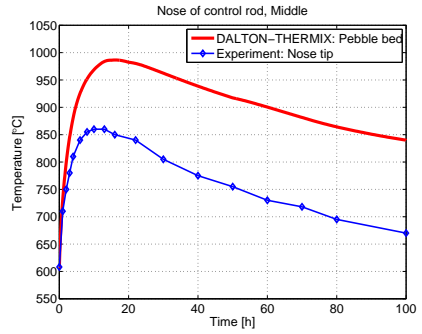
(a) Point A



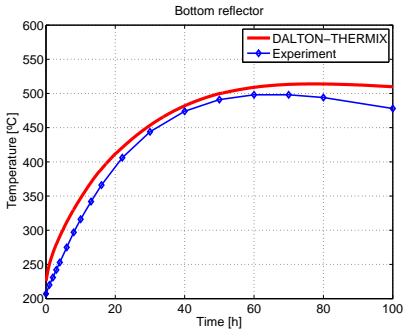
(b) Point B



(c) Point C



(d) Point D



(e) Bottom reflector

Fig. 2.15: Temperature histories of the side reflector and tip of the reflector nose, points A through D of Fig. 1.3(b), and the bottom reflector.

2.5 Simulation of the Pebble Bed Modular Reactor

The Pebble Bed Modular Reactor (PBMR) is a High Temperature gas cooled Reactor that is currently being designed by the PBMR Ltd. Steady state and transient benchmark exercises were organized by the Nuclear Energy Agency (NEA)[71]. In this section the results of the DALTON-THERMIX code system for a coupled steady state and (De)Pressurized Loss Of Forced Cooling (DLOFC/PLOFC) transient cases of the PBMR are verified with the results of the TINTE code system [54] made available by the PBMR Ltd. [72].

In this section the effect on the operating temperature for increased reactor power and size is investigated, going from a demonstration size, such as the HTR-10 (10 MW) and AVR (46 MW) reactors, to a commercial size of 400 MW. Neutron cross

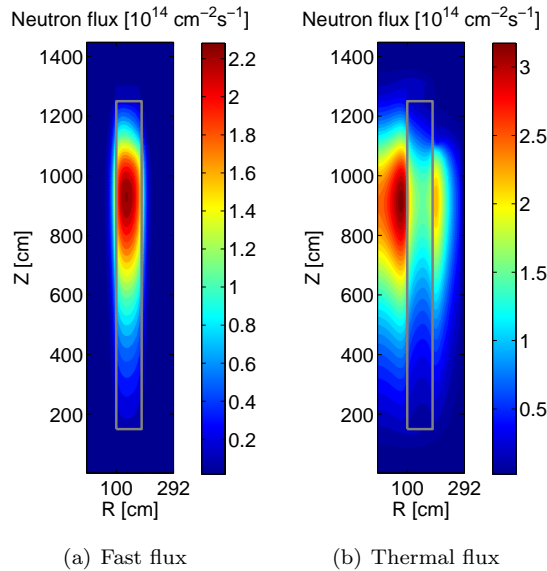


Fig. 2.16: The fast 2.16(a) and thermal 2.16(b) flux profiles in the PBMR at normal operating conditions showing the location of the peaks. The solid line shows the region of the pebble bed.

sections that depend on the fuel temperature, moderator temperature, xenon concentration, local fast and thermal buckling were provided as part of the benchmark description [71]. The buckling dependence was included to capture the spectral effects resulting from changes in the environment of a given core region. The local buckling

2. Validation of a neutronics and thermal-hydraulics code system for the simulation of pebble-bed reactors

of group g in a certain mesh volume is defined as:

$$B_g^2 = \frac{-\nabla \cdot D_g \nabla \phi_g}{D_g \phi_g}. \quad (2.2)$$

The control rods that are located in the side reflector, are modeled as a uniform 'grey curtain'. The plenum above the pebble bed and the helium gap between the side reflector and the core barrel are modeled as void regions using directional diffusion coefficients [62].

Normal operating conditions

A coupled neutronics / thermal-hydraulics calculation is performed to determine the conditions of the reactor during normal operation. In this case the resulting neutron flux profile from a DALTON eigenvalue calculation was normalized to a fixed power level of 400 MW, while the k_{eff} was allowed to deviate from unity. Several iterative runs of DALTON and THERMIX are performed until convergence is reached on the k_{eff} . The results for the neutron flux profiles, axial temperature and power profiles are shown in Figs. 2.16(a), 2.16(b), 2.17 and 2.18, respectively.

The flux profiles in Figs. 2.16(a) and 2.16(b) show a peak at the top of the pebble bed, which is caused by the fact that fresh fuel is inserted at the top of the core and removed at the bottom. The thermal flux profile shows peaks in the inner and outer reflector, resulting in power peaks near the radial edges of the pebble bed.

In Table 2.4 some key results of the two code systems are compared. The power profile in DALTON has a higher peak, which also results in a higher maximum neutron flux compared to TINTE. The differences for the average temperatures are within several degrees C. This can also be seen from Fig. 2.17 in which the axial profiles of the maximum and average fuel temperatures are shown. The small differences can be attributed to the difference in the power profile (see Fig. 2.18), resulting in higher temperatures for the DALTON-THERMIX results in the region of the power peak.

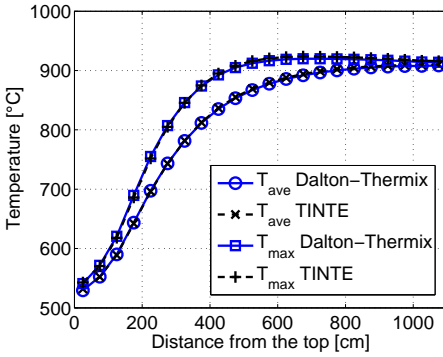
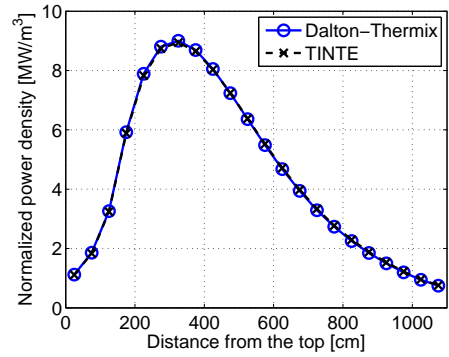
In general, a good agreement between the two code systems is found for the steady state results, although some differences in the neutronic results were encountered. In order to start from an exactly critical reactor at the beginning of the transient calculations the fission source (RHS of Eq. (B.3)) was scaled with the eigenvalue.

Depressurized Loss Of Forced Cooling

The first transient is a Depressurized Loss Of Forced Cooling (DLOFC) without SCRAM. Starting from full load operating conditions, the mass flow is reduced to 0.2 kg/s and the pressure to 1 bar assuming a linear reduction over 13 seconds. In a second case, assuming a SCRAM after 13 seconds, the control rods are fully inserted

Table 2.4: Comparison of Steady State results between DALTON-THERMIX and TINTE

Item	DALTON - THERMIX	TINTE	Unit
k_{eff}	0.99364	0.99396	-
Maximum Power density	10.64	10.55	W/m ³
Maximum fast flux	$2.27 \cdot 10^{14}$	$2.14 \cdot 10^{14}$	cm ⁻² s ⁻¹
Maximum thermal flux	$3.37 \cdot 10^{14}$	$3.17 \cdot 10^{14}$	cm ⁻² s ⁻¹
Outlet helium temperature	898.2	898.5	°C
Pressure drop	297.9	294.2	kPa
Average fuel temperature	807.4	813.0	°C
Average moderator temperature	794.0	787.2	°C
Average helium temperature	748.2	742.3	°C

**Fig. 2.17:** Comparison of the axial profile of the average and maximum fuel temperatures for DALTON-THERMIX and TINTE results at normal operating conditions of the PBMR.**Fig. 2.18:** Comparison of the axial power profile of DALTON-THERMIX and TINTE results at normal operating conditions of the PBMR.

within 3 seconds. Furthermore, the mass flow is reduced to 0 kg/s instead of the trickle flow of 0.2 kg/s.

The response of the reactor power for both cases (with or with SCRAM) of the DALTON-THERMIX calculation during the first 300 seconds is presented in Fig. 2.19. The temperature feedback causes a reduction in the fission power of the reactor. In the case that a reactor SCRAM is included, the fission power is reduced rapidly and the total reactor power is determined by the decay heat within seconds after the SCRAM.

In the case that no SCRAM is initiated, the reactor becomes critical again after it has sufficiently cooled down. The point of re-criticality occurs in the DALTON-

2. Validation of a neutronics and thermal-hydraulics code system for the simulation of pebble-bed reactors

THERMIX calculation after 51.8 h, compared to 50.0 h for the TINTE calculation. After several oscillations in power and temperature the fission power reaches a quasi-steady state (see Fig. 2.20), while both the temperature of the pebble-bed and of the reflector increase in the following hours (see Fig. 2.21).

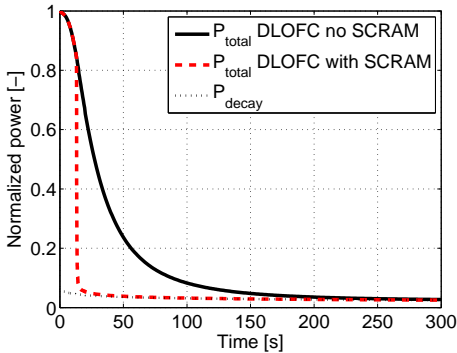


Fig. 2.19: Power (total and decay) history of DALTON-THERMIX for the first 300 seconds of the DLOFC transient showing the effect of a SCRAM.

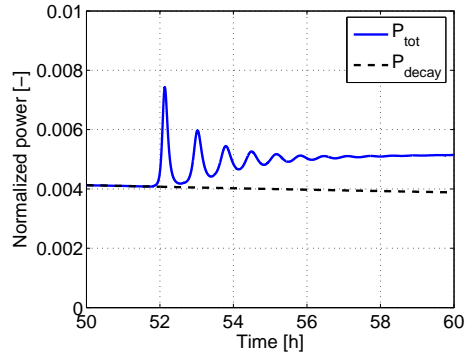


Fig. 2.20: Power (total and decay) history of DALTON-THERMIX results (between 50 and 60 hours) of the DLOFC (no SCRAM) transient.

The fuel temperature histories for the DLOFC with SCRAM are presented in Fig. 2.22. The resulting temperatures are higher than for the case without the SCRAM since the trickle flow of 0.2 kg/s is absent. The results for the average and peak fuel temperatures calculated with DALTON-THERMIX and TINTE are similar.

Pressurized Loss Of Forced Cooling with SCRAM

The Pressurized Loss Of Forced Cooling (PLOFC) case is similar to the DLOFC case with SCRAM with the difference that the system pressure is reduced from 90 bar to 60 bar during the first 13 seconds of the transient and the mass flow is reduced to 0 kg/s instead of 0.2 kg/s. After the pressure reduction it is assumed that the helium inventory of the reactor remains constant, allowing the pressure to vary over time depending on the helium temperature.

The power history of the PLOFC transient is almost identical to the power history for the DLOFC with SCRAM of Fig. 2.19 except for minor differences during the first 13 seconds.

The results for the fuel temperatures in Fig. 2.23 of the two codes again show a similar trend with DALTON-THERMIX predicting slightly lower temperatures.

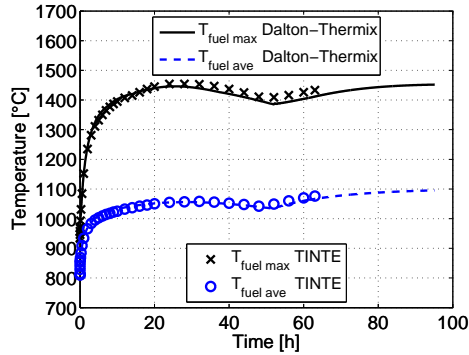


Fig. 2.21: Maximum (*max*) and Average (*ave*) temperature history of DALTON-THERMIX and TINTE results for the DLOFC transient (without SCRAM).

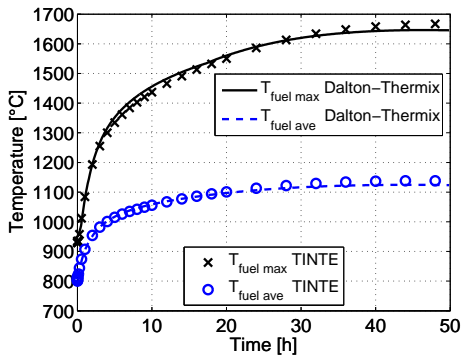


Fig. 2.22: Maximum (*max*) and average (*ave*) temperature history of DALTON-THERMIX and TINTE results for the entire DLOFC (with SCRAM) transient.

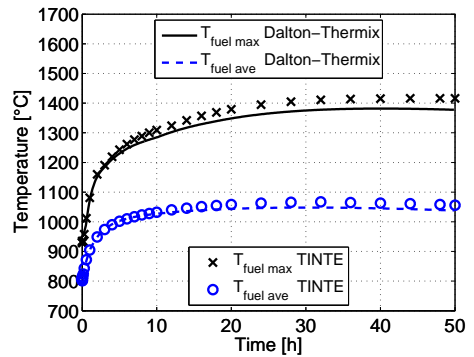


Fig. 2.23: Maximum (*max*) and average (*ave*) temperature history of DALTON-THERMIX and TINTE results for the entire PLOFC (with SCRAM) transient

The natural convection in the reactor increases the ability of the reactor to remove the decay heat, resulting in lower temperatures than encountered in the DLOFC (with SCRAM) case. In Figs. 2.24 and 2.25 the temperature profiles in the reactor are shown after 50 hours in the PLOFC transient and after 100 hours in the DLOFC transient. It can be seen that for the PLOFC case, which includes natural convection, the heat is transported to the top region of the core. The maximum fuel temperature for the PLOFC is 1382 °C, which is significantly lower than the 1648 °C that was found for the DLOFC case.

2. Validation of a neutronics and thermal-hydraulics code system for the simulation of pebble-bed reactors

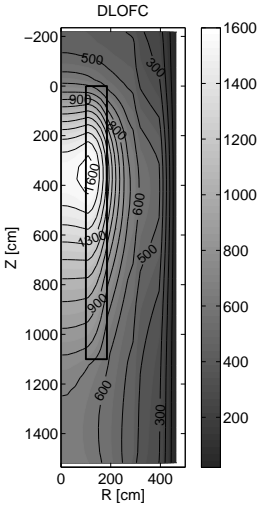


Fig. 2.24: Temperature profile [°C] at $t = 100$ hours of the DLOFC simulation with SCRAM.

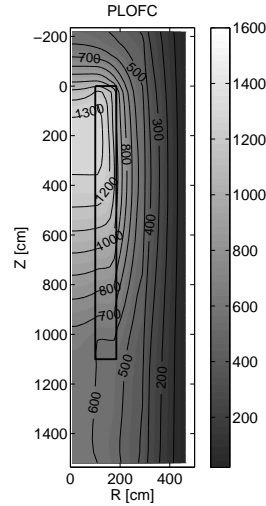


Fig. 2.25: Temperature [°C] profile at $t = 50$ hours of the PLOFC simulation with SCRAM.

2.6 Conclusion

In this chapter a new code system for the evaluation of static and dynamic behavior of pebble-bed reactors has been presented. Comparisons of the results of this code system with experimental data and TINTE of normal operation and LOFC transients were made for the HTR-10, AVR and PBMR reactors.

Regarding the modeling of pebble-bed HTRs the following is concluded:

- During normal operation of a pebble-bed reactor the convective heat transfer from the pebbles to the helium coolant effectively removes the heat from the core. Only a small portion (less than 1 % of the total power) of the generated heat is transferred to the surroundings by conduction and thermal radiation. In the absence of forced cooling during D\PLOFC transients, the value of this small heat loss determines the behavior of the reactor. The maximum temperature reached, the rate at which the core cools down thereafter and the consequent time point of re-criticality (if no SCRAM is performed) are largely dependent of this heat loss. Furthermore, the steady state power level reached after re-criticality (no SCRAM) is equal to the total heat loss of the reactor.
- It was found that the heat transfer by natural convection in HTR can also be of importance during loss of flow transients, even in a depressurized case. From the AVR benchmark it was learned that natural convection in the top region of

the core has a significant impact on the heat transfer between the core and the steam generator. Heat transfer through conduction and radiation alone could not explain the measured amount of heat transported to the steam generator.

- Small core flows, such as bypass flows for cooling of reflectors and control rods can be of major importance to the nominal and transient core behavior. This is caused by the resulting effect on the fuel and moderator temperatures, which have a large temperature reactivity feedback. It is therefore recommended that these flows are recorded during experiments and are incorporated in benchmark exercises.
- From the calculation of the initial criticality of the HTR-10 it was found that the contamination of boron in the moderator and graphite reflectors as well as the concentration of boron in the carbon bricks surrounding the reflector has a major impact on the criticality of the reactor, caused by the large absorption cross section of ^{10}B .
- The large helium cavities containing relatively cold helium at the top and bottom of the reactor have a large influence on the transient behavior. Their presence influences the way that the natural circulation flows are established.
- A point-kinetic model can be an effective tool for modeling the neutronics of small pebble-bed HTRs for some transients. However, the large change in the temperature and power profile during a D\PLOFC transient in an HTR, even in small cores such as the HTR-10, result in significant differences between the point-kinetic and (2D) neutronic calculation results.

Conclusions regarding the DALTON-THERMIX code system:

- The DALTON-THERMIX code system can effectively predict the temperatures in the core during normal and P\DLOFC transients for small and large pebble-bed reactor designs. It captures the dynamic behavior of the reactor and is therefore a useful tool in determining the inherent safety capabilities of pebble-bed HTR designs. Therefore, the DALTON-THERMIX code system forms the basis of the investigations that are presented in the following chapters on several pebble-bed VHTR designs as was proposed in Chap. 1.
- THERMIX underpredicts the natural circulation flows in depressurized transient cases and is therefore conservative with regard to the fuel temperature. Especially the description of the flow field in gas cavities is limited in THERMIX and could be improved.
- Some 3D geometry effects are not captured by the code system since THERMIX is limited to 2D (r-z). This limitation resulted in a significant difference between calculation and experimental result for the temperature of the AVR reflector nose.

From the viewpoint of HTR safety it was found that in the small HTR designs, such as the HTR-10 and AVR, the increase of the maximum fuel temperature during a

2. Validation of a neutronics and thermal-hydraulics code system for the simulation of pebble-bed reactors

D\LOFC compared to normal operation is within 100 °C. However, in the DLOFC case (with SCRAM) of the PBMR it was found that the maximum fuel temperature during the transient is 1648 °C. This is caused by the increase in power density, going from 2.1 MW/m³ (full load) and 2.6 MW/m³ of the HTR-10 and AVR reactors to a value of 4.8 MW/m³ for the PBMR design. An increase of the reactor power in the PBMR during normal operation aiming at an increased helium outlet temperature leads to an increased power density and resulting higher fuel temperature. In the following chapter the impact of the operating temperature on the integrity of the fuel is investigated to determine the maximum permissible fuel temperature.

3

Performance of coated particle fuel in High Temperature Reactors

The fuel design of all HTRs currently planned and investigated is largely based on experience gained primarily in German research reactors [11] over a span of several decades (AVR, THTR, Dragon designs, etc). The coating layers (IPyC, SiC and OPyC) of the TRISO particles provide the primary containment of the fission products that are produced within the fuel kernel. As a consequence, numerous publications on integrity and performance of the TRISO coated particles can be found in literature since the nineteen sixties [73], ranging from stress analysis investigations [74] to recent fully integrated fuel performance models [75, 76, 77, 78, 79, 80].

TRISO particles in HTRs experience stresses due to gaseous fission products build up within the buffer layer, shrinkage/swelling of the pyrocarbon layers and thermal expansion of all the layers. In most analyses of stresses and strains, the mechanical model consists of a single particle in vacuum [75, 74]. However, in the fuel zone of today's pebble designs, the TRISO particles can be within a short distance of one another [81] and it is therefore likely that the stress fields of neighboring particles influence the stress state of a given particle. Furthermore, the graphite in which the particles are embedded experiences dimensional change under irradiation, which in turn causes additional stresses on the fuel particles.

The PArticle STress Analysis (PASTA) code has been developed to calculate the stresses in the different layers of the coated particles and surrounding graphite during irradiation. This code is an extension of existing analytical models [74], based on visco-elastic description of stresses, and is able to quantify the effects mentioned above.

This chapter gives a description of the stress analysis model. First, the procedure for the determination of the boundary conditions (i.e. internal pressure, dimensional changes and fluence) for the PASTA code is presented in Sec. 3.1. In Sec. 3.2 a

detailed derivation of the analytical stress model in PASTA is presented. Sec. 3.3 describes the theory of the stress effects caused by the dimensional changes of the matrix graphite and neighboring particles. In the final sections of this chapter the PASTA code is applied to two cases in order to verify the model and to quantify the effects of the intended increase in operating temperature. An increase in the fuel temperature leads to higher internal pressure in the buffer layer of the coated particles, which is expected to increase the particle failure probability. The two cases considered are the HTTR [82] (first fuel loading) and a 400 MW_{th} HTR pebble-bed reactor model based on the PBMR-400 design. In the latter, the effect of the fuel temperature on the stresses in the coatings and the consequent failure probability are investigated.

3.1 Calculation procedure in stress analysis

Prior to the use of the stress analysis code PASTA, the boundary conditions such as the neutron flux, burnup and temperature profiles of the reactor core are calculated. These data are exploited to calculate the gaseous fission products generation inside the kernel, and their diffusion to, and build up within, the buffer layer. Also computed is the shrinkage/swelling of the pyrocarbon layers during the lifetime of the particle. During each time step, corresponding to a given position of the pebble in the core and a given irradiation dose, the mechanical stresses are evaluated. The following sections provide a more detailed description of the different calculation tools and assumptions that are used in this context.

Neutronics, thermal-hydraulics and fuel depletion

In the stress analysis of Sec. 3.4 of this chapter, a two-dimensional cylindrical geometry with axial symmetry is used in DALTON to model the neutronics of the reactor. The power profile is passed to the thermal hydraulics code THERMIX, while the flux profile is radially collapsed to a one-dimensional axial profile. This profile is used to determine the burnup history of the fuel. A detailed description of the method used to determine the equilibrium core composition and burnup history of the fuel is given in chapter 4. The thermal hydraulics code THERMIX (Direkt) [48] is used to compute the temperature profile from the given power profile. By performing iterative coupled calculations with the neutronics-thermal hydraulics codes, the steady state operating conditions of the design are determined following the procedure described in Chap. 2. To calculate the temperatures in the fuel particles, the results of THERMIX are used in an additional calculation [83], which takes into account the thermal resistance of the gap between the porous buffer layer and the inner pyrocarbon (IPyC) layer.

Irradiation effects in the particle coatings during operation

Fission products are formed within the fuel kernel as the fuel is depleted. The gaseous fission products diffuse to, and accumulate in, the buffer layer, and induce a pressure build up which depends on the kernel temperature and buffer volume.

Formation and diffusion of gaseous fission products in the fuel kernel

The buildup of gaseous fission products can be calculated analytically and numerically [75, 84] by solving the time-dependent fission product diffusion equation,

$$\frac{\partial C}{\partial t} = \frac{D_{fis}}{r^2} \frac{\partial}{\partial r} \left(r^2 \frac{\partial C}{\partial r} \right) + Q \quad (3.1)$$

in which C is the fission product concentration (cm^{-3}), r is the radial position in the kernel (cm), D_{fis} is the diffusion coefficient ($\text{cm}^2 \cdot \text{s}^{-1}$) and Q the source term of fission products ($\text{cm}^{-3} \cdot \text{s}^{-1}$). The source term is determined by the local power (burnup rate) in the reactor. From a fuel depletion analysis with ORIGEN [55] it is found that approximately one third of the fission products are gaseous xenon and krypton, which compares well with the 31 % found in Ref. [85]. Although an analytical solution exists using simplified boundary conditions, the numerical approach is preferred and used to solve Eq. (3.1). This method allows for a nonzero concentration at the boundary, which is an improvement compared to the analytical approach in which a zero concentration in the porous buffer layer is usually assumed throughout the irradiation period [84].

Besides direct formation of gaseous fission products, formation of CO gas by a reaction of oxygen present in the fuel kernel with carbon in the buffer layer is possible. The formation of this gas is taken into account by the following empirical formula [85, 86] for oxygen release per fission:

$$O/f = 8.32 \cdot 10^{-11} t_{irr}^2 e^{\left(\frac{-Z}{R \cdot T}\right)} \quad (3.2)$$

In this equation O/f is the number of oxygen atoms released per fission, after an irradiation time t_{irr} (s); Z has the value $162.7 \text{ kJ} \cdot \text{mol}^{-1}$, R is the universal gas constant ($\text{J} \cdot \text{mol}^{-1} \cdot \text{K}^{-1}$) and T is the temperature (K).

Calculation of the pressure in the buffer layer

The resulting pressure (p) on the IPyC layer is calculated with the Redlich Kwong equation of state [46], as a function of the kernel temperature (T_{kernel}) and the buffer

(molar) volume (V_m):

$$RT_{kernel} = \left(p + \frac{a}{T_{kernel}^{\frac{1}{2}} V_m (V_m + b)} \right) (V_m - b) \quad (3.3)$$

in which a and b are constants. The ideal gas law is not applied here, because it under-predicts the pressure significantly [76].

Dimensional change and creep of particle coatings

Under irradiation, the PyC layers are exposed to a fast neutron flux, which causes dimensional changes. The dimensional change rate depends on the initial density and anisotropy of the pyrocarbon material. Several empirical relations for the radial and tangential dimensional change rate exist [76]. In general the layers shrink at low neutron dose. This shrinking eventually comes to a halt at higher irradiation dose. In some cases, depending on the material properties, the shrinking turns into swelling at higher doses. The following relations are adopted in the present fuel performance model [76]:

$$\dot{S}_r = -0.077e^{(-t)} + 0.031 \quad (3.4)$$

$$\dot{S}_t = -0.036e^{(-2.1t)} - 0.01 \quad (3.5)$$

In these relations \dot{S}_r and \dot{S}_t are the dimensional change rates in the radial and tangential directions, respectively, expressed in $(10^{25}\text{m}^{-2})^{-1}$ and t is the fast neutron fluence (for energies $E > 0.1$ MeV) expressed in 10^{25}m^{-2} .

Moreover, pyrocarbon and graphite materials creep under irradiation, partly reducing the stress. For the pyrocarbon layers a value of $3.0 (\text{MPa}\cdot 10^{29} \text{m}^{-2})^{-1}$ is taken for the creep coefficient from literature [76]. From references [87, 88] the irradiation creep coefficient for HTGR (matrix) graphite was determined to be in the range of $3.4 - 4.8 (\text{MPa}\cdot 10^{29} \text{m}^{-2})^{-1}$ (for $E > 0.18$ MeV) at 1029 K - 1257 K, with an average value of $4.2 (\text{MPa}\cdot 10^{29} \text{m}^{-2})^{-1}$.

Calculation of the failure fraction of SiC

The combined effects of the fission products buildup in the buffer, the dimensional change, and the creep of the PyC layers lead to a certain stress in the SiC layer. The SiC layer is the main load bearer within the TRISO particle and can withstand high compressive stresses, but it could fail under high tensile stresses. The failure fraction of the SiC layer in the kernel can be calculated using the Weibull distribution function [82, 76, 89],

$$\Phi = 1 - e^{-\ln 2 \left(\frac{\sigma_t}{\sigma_{med}} \right)^m} \quad (3.6)$$

where σ_t and σ_{med} are the maximum tangential (tensile) stress and the median strength in the SiC, respectively. m is the modulus, taken to be 8.0 and the median strength is taken as 834 MPa, as reported in [82].

3.2 Derivation of an analytical model for a 4-layer pressure vessel

An analytical model is set up to calculate the tangential stresses as a function of the (fast) neutron dose in the coatings of the fuel particle and the surrounding graphite matrix. The approach taken is based on previously developed models [74, 90]. The major difference between those models and the current work is the addition of an extra layer representing the graphite matrix material surrounding the TRISO particle (see Fig. 3.1). By including this layer the effect of the graphite matrix dimensional changes and the stress effect of neighboring particles can be modeled. It is noted that, as in the previously existing models, the fuel kernel and buffer layer are not explicitly represented. It is assumed that possible swelling of the fuel kernel can be accommodated by the surrounding porous buffer layer.

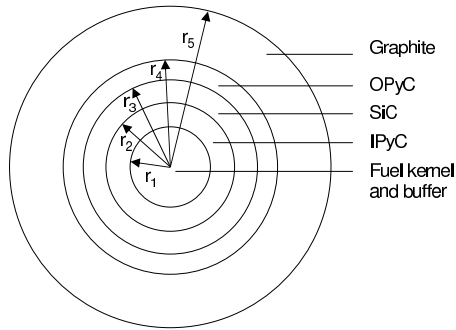


Fig. 3.1: *Geometry of a TRISO particle and graphite layer used in the 4-layer stress model.*

In the next section the equations for the stresses in a 4-layer pressure vessel are derived. The creep behavior in the pyrocarbon layers of the fuel particle and in the graphite matrix are modeled using a Maxwellian creep model. This model assumes that the steady state strain rate can be represented by an elastic model (spring) and a viscous model (dash pot) in series [90]. Transient creep is ignored because the resulting effects are expected to be small [91].

Governing equations and solution

The strain derivatives with respect to the neutron fluence t for the radial and tangential direction in a spherical element, including the source terms for the irradiation dimensional change rate (\dot{S}_r and \dot{S}_t) and the thermal expansion rates ($\alpha_r \dot{T}$ and $\alpha_t \dot{T}$),

can be written as [74]:

$$\frac{\partial \varepsilon_r}{\partial t} = \frac{1}{E} \left[\frac{\partial \sigma_r}{\partial t} - 2\mu \frac{\partial \sigma_t}{\partial t} \right] + c [\sigma_r - 2\nu \sigma_t] + \alpha_r \dot{T} + \dot{S}_r \quad (3.7)$$

$$\frac{\partial \varepsilon_t}{\partial t} = \frac{1}{E} \left[(1 - \mu) \frac{\partial \sigma_t}{\partial t} - \mu \frac{\partial \sigma_r}{\partial t} \right] + c [(1 - \nu) \sigma_t - \nu \sigma_r] + \alpha_t \dot{T} + \dot{S}_t \quad (3.8)$$

From the strain-displacement relations and equilibrium requirement it follows [92] that:

$$\varepsilon_r = \frac{\partial u}{\partial r} \quad (3.9)$$

$$\varepsilon_t = \frac{u}{r} \quad (3.10)$$

$$\frac{\partial \sigma_r}{\partial r} + \frac{2}{r} (\sigma_r - \sigma_t) = 0 \quad (3.11)$$

where u is the radial displacement.

In order to find the solutions to the above equations, the same procedure is used as in reference [93]. The closed form solution in this reference is an improvement over the earlier solution found in [90] and allows the material properties to change with irradiation dose. Furthermore, the solution allows for the Poisson's ratio of creep to deviate from $\nu = 0.5$.

The solutions for the radial displacement and for the radial and tangential stresses are assumed to be in form of a polynomial series [74]:

$$u(r, t) = \sum_{i,n=0}^{\infty} u_{i,n} t^n \quad (3.12)$$

$$\sigma_r(r, t) = \sum_{i,n=0}^{\infty} \sigma_{r,i} t^n \quad (3.13)$$

$$\sigma_t(r, t) = \sum_{i,n=0}^{\infty} \sigma_{t,i} t^n \quad (3.14)$$

The incremental solution for the displacement can be found by combining Eqs. (3.7)-(3.14), [74]:

$$\frac{d^2 u_i}{dr^2} + \frac{2 du_i}{r dr} - \frac{2}{r^2} u_i = \frac{2}{Er} (1 - 2\mu) f_i + \frac{2}{r} c (1 - 2\nu) \frac{f_{i-1}}{i} \quad (3.15)$$

where

$$f_{i+1} = -\frac{cE(1-\nu)}{(1-\mu)} \frac{f_i}{i+1} + \frac{E \left(\dot{S}_{r,i} - \dot{S}_{t,i} + \alpha_r \dot{T}_i - \alpha_t \dot{T}_i \right)}{(1-\mu)(i+1)} \quad (3.16)$$

with $f_0 = 0$. A function $F(t)$ can be defined by

$$F(t) = \sum_{i,n=1}^{\infty} f_i t^n \quad (3.17)$$

This function is used later in this chapter to determine the stresses within the coating layers. The incremental solution for the displacement obtained from Eqs. (3.15) and (3.16) is:

$$u_i = A_i r + \frac{B_i}{r^2} + \left[\frac{2(1-2\mu)}{3E} f_i + \frac{2c(1-2\nu)}{3i} f_{i-1} \right] r \ln(r) \quad (3.18)$$

where A_i and B_i are coefficients to be determined later. Using Eq. (3.18), the corresponding equations for the incremental stresses can be found:

$$\begin{aligned} \sigma_{r,i} = & \frac{E}{(1-2\mu)} A_i - \frac{E}{(1+\mu)} \frac{2B_i}{r^3} \\ & + \frac{2}{3} ((1+\mu) \ln(r) + (1-\mu)) \left[\frac{1}{(1+\mu)} f_i + \frac{Ec(1-2\nu)}{(1+\mu)(1-2\mu)i} f_{i-1} \right] \\ & - \frac{cE}{(1+\mu)i} \left[\left(1 + \frac{\mu(1-2\nu)}{(1-2\mu)} \right) \sigma_{r,i-1} + \left(\frac{(1-2\nu)}{(1-2\mu)} - 1 \right) \sigma_{t,i-1} \right] \\ & - \frac{E \left(2\mu(\dot{S}_{t,i-1} + \alpha_t \dot{T}_{i-1}) + (1-\mu)(\dot{S}_{r,i-1} + \alpha_r \dot{T}_{i-1}) \right)}{(1+\mu)(1-2\mu)i} \end{aligned} \quad (3.19)$$

$$\begin{aligned} \sigma_{t,i} - \sigma_{r,i} = & \frac{3E}{(1+\mu)} \frac{B_i}{r^3} - \frac{2}{3(1+\mu)} \left[(1-2\mu) f_i + \frac{Ec(1-2\nu)}{i} f_{i-1} \right] + \\ & + \frac{Ec(1+\nu)}{(1+\mu)i} (\sigma_{r,i-1} - \sigma_{t,i-1}) + \frac{E \left((\dot{S}_{r,i-1} + \alpha_r \dot{T}_{i-1}) - (\dot{S}_{t,i-1} + \alpha_t \dot{T}_{i-1}) \right)}{(1+\mu)i} \end{aligned} \quad (3.20)$$

The internal and external pressures, $p(t)$ and $q(t)$, are applied as the boundary conditions at the inner and outer radii of the layer under consideration, i.e. at r_a and r_b , respectively, by expressing them in the following forms:

$$p(t) = \sum_{i,n=0}^{\infty} p_i t^n \quad q(t) = \sum_{i,n=0}^{\infty} q_i t^n \quad (3.21)$$

In this sign convention the pressures $p(t)$ and $q(t)$ are positive outward. Following reference [90], Eq. (3.19) is used to equate the radial stress at the surfaces to the above pressures. The coefficients A_i and B_i can now be found. Furthermore, a useful

3. Performance of coated particle fuel in High Temperature Reactors

relation that applies for the radial and tangential stress components in a spherical shell, between radii r_a and r_b , is derived from Eq. (3.20):

$$\sigma_{t,i}(r) - \sigma_{r,i}(r) = \frac{3(r_a r_b)^3}{r^3(r_a^3 - r_b^3)} \left(p_i - q_i - \frac{2}{3} f_i \ln \frac{r_a}{r_b} \right) + \frac{f_i}{3} \quad (3.22)$$

Eqs. (3.18) and (3.22) are combined and a general expression for the displacement in a spherical layer is found:

$$u(r, t) = K_1 p(t) + K_2 q(t) + K_3 \int p(t) c dt + K_4 \int q(t) c dt + K_5 \int \left(\dot{S}_r(t) + \alpha_r \dot{T}(t) \right) dt + K_6 \int \left(\dot{S}_t(t) + \alpha_t \dot{T}(t) \right) dt + K_7 F(t) \quad (3.23)$$

The coefficients K_i are given in App. C. They depend on the radial position, the geometry and material properties of the layer. It is noted that the coefficient K_7 vanishes at the layer boundaries, i.e. $r = r_a$ or $r = r_b$.

Solutions for the displacement of each interface between two layers at any point in time are sought. The boundary conditions at each interface between two layers imply continuity of radial stress and displacement. The pyrocarbon and graphite layers are assumed to exhibit creep and anisotropic swelling, and all four layers are allowed to exhibit anisotropic thermal expansion. For all the layers the displacements at interfaces (i.e. layer inner and outer surfaces) are given by Eqs. (3.24)-(3.29). In these equations, p , $\sigma_{r,I}$, $\sigma_{r,O}$, $\sigma_{r,X}$ and q are respectively the pressure in the buffer layer, the radial stress at the IPyC outer surface (or SiC inner surface due to continuity of radial stress through an interface), the radial stress at the OPyC inner surface, the radial stress at the matrix graphite inner surface and the pressure on the outer surface.

IPyC outer surface

$$u_I = a_1 p + a_2 \sigma_{r,I} + a_3 \int p c_I dt + a_4 \int \sigma_{r,I} c_I dt + a_5 \int \left(\dot{S}_{r,I} + \alpha_{r,I} \dot{T}_I \right) dt + a_6 \int \left(\dot{S}_{t,I} + \alpha_{t,I} \dot{T}_I \right) dt \quad (3.24)$$

SiC inner and outer surface

$$u_I = b_1 \sigma_{r,I} + b_2 \sigma_{r,O} + b_3 \int \alpha_{r,S} \dot{T}_S dt + b_4 \int \alpha_{t,S} \dot{T}_S dt \quad (3.25)$$

$$u_O = c_1 \sigma_{r,I} + c_2 \sigma_{r,O} + c_3 \int \alpha_{r,S} \dot{T}_S dt + c_4 \int \alpha_{t,S} \dot{T}_S dt \quad (3.26)$$

OPyC inner and outer surface

$$u_O = d_1\sigma_{r,O} + d_2\sigma_{r,X} + d_3 \int \sigma_{r,O}c_O dt + d_4 \int \sigma_{r,X}c_O dt + d_5 \int (\dot{S}_{r,O} + \alpha_{r,O}\dot{T}_O) dt + d_6 \int (\dot{S}_{t,O} + \alpha_{t,O}\dot{T}_O) dt \quad (3.27)$$

$$u_X = e_1\sigma_{r,O} + e_2\sigma_{r,X} + e_3 \int \sigma_{r,O}c_O dt + e_4 \int \sigma_{r,X}c_O dt + e_5 \int (\dot{S}_{r,O} + \alpha_{r,O}\dot{T}_O) dt + e_6 \int (\dot{S}_{t,O} + \alpha_{t,O}\dot{T}_O) dt \quad (3.28)$$

Graphite-matrix

$$u_X = f_1\sigma_{r,X} + f_2q + f_3 \int \sigma_{r,X}c_X dt + f_4 \int qc_X dt + f_5 \int (\dot{S}_{r,X} + \alpha_{r,X}\dot{T}_X) dt + f_6 \int (\dot{S}_{t,X} + \alpha_{t,X}\dot{T}_X) dt \quad (3.29)$$

The coefficients a_i, b_i, \dots, f_i can be calculated from the constants K_i given in App. C, by inserting the appropriate values for the layers.

Radial stresses at the interfaces

By equating the displacements at the layer interfaces of Eqs. (3.24)-(3.29) and differentiating with respect to t a system of equations for the radial stress at the interfaces is obtained. For the above 4-layer problem a system of three inhomogeneous linear equations is obtained (see App. C for the explicit expressions):

$$\dot{\sigma}_r - \mathbf{B}\sigma_r = \mathbf{G}(t) \quad (3.30)$$

which has the solution [94]:

$$\sigma_r = \sum_{i=1}^3 C_i \xi_i e^{\lambda_i t} + \mathbf{g}_0 + \mathbf{g}_1 t \quad (3.31)$$

where ξ_i and λ_i are the eigenvectors and eigenvalues of the \mathbf{B} matrix and C_i are constants determined by the initial conditions. In practice the eigenvalues and eigenvectors can be quickly calculated by numerical procedures. After this computation step the vectors \mathbf{g}_0 and \mathbf{g}_1 are calculated by inserting Eq. (3.31) into Eq. (3.30) and performing a simple Gauss elimination.

The function $F(t)$

When the radial stresses at the layer interfaces are known, the radial and tangential stresses at each point within the layers can be determined. Substituting Eq. (3.16)

into Eq. (3.17) and differentiating with respect to t yields the following equation for the function F :

$$\frac{dF}{dt} + \frac{cE(1-\nu)}{1-\mu}F = \frac{E}{1-\mu} \left(\overline{\dot{S}_r} + \overline{\alpha_r \dot{T}} - \overline{\dot{S}_t} - \overline{\alpha_t \dot{T}} \right) \quad (3.32)$$

in which the overline indicates that the relevant property is numerically averaged and is assumed to be constant over the time interval. The general solution for the function $F(t_n)$ is obtained by integrating between t_{n-1} and t_n :

$$F(t_n) = [F(t_{n-1}) - \gamma_0] e^{-\beta(t_n - t_{n-1})} + \gamma_0 \quad (3.33)$$

where,

$$\beta = \frac{cE(1-\nu)}{(1-\mu)} \quad (3.34)$$

$$\gamma_0 = \frac{\overline{\dot{S}_r} - \overline{\dot{S}_t} + \overline{\alpha_r \dot{T}} - \overline{\alpha_t \dot{T}}}{c(1-\nu)} \quad (3.35)$$

General stress equations

Eq. (3.31) gives the radial contact stresses at the interface of the layers. Used together with Eq. (3.33) it allows the determination of radial and tangential stresses at any position in the layers following the procedure in reference [90]. This results in:

$$\begin{aligned} \sigma_r(r, t) = & \frac{r_a^3 (r_b^3 - r^3)}{r^3 (r_b^3 - r_a^3)} p - \frac{r_b^3 (r_a^3 - r^3)}{r^3 (r_b^3 - r_a^3)} q \\ & - \frac{2}{3} \left[\frac{r_a^3 (r_b^3 - r^3) \ln r_a - r_b^3 (r_a^3 - r^3) \ln r_b}{r^3 (r_b^3 - r_a^3)} - \ln r \right] F(t) \quad (3.36) \end{aligned}$$

$$\begin{aligned} \sigma_t(r, t) = & -\frac{r_a^3 (r_b^3 + 2r^3)}{2r^3 (r_b^3 - r_a^3)} p + \frac{r_b^3 (r_a^3 + 2r^3)}{2r^3 (r_b^3 - r_a^3)} q \\ & + \frac{1}{3} \left[\frac{r_a^3 (r_b^3 + 2r^3) \ln r_a - r_b^3 (r_a^3 + 2r^3) \ln r_b}{r^3 (r_b^3 - r_a^3)} + 2 \ln r + 1 \right] F(t) \quad (3.37) \end{aligned}$$

The boundary conditions in this equation, p and q , are the radial stresses on the inner and outer surface of the layer, respectively. The radial stress p on the inner surface of the IPyC layer is calculated from the build-up of fission product in the buffer layer (Eq. 3.1). The boundary condition on the outer surface of the 4th (graphite matrix) layer is a zero radial stress in general, but can be set to a non-zero stress state to simulate the stress effect of neighboring particles. The calculation of this outer surface stress is dealt with in the following section.

3.3 Stress effects in the graphite matrix

Stress effects due to dimensional change of the graphite matrix

The 4-layer model that was derived in the previous section is now used to investigate the effects of adding a graphite layer to the 3-layer model. It is noted that at first the irradiation induced dimensional change of the fourth (graphite) layer is not taken into account. The properties of the particle and the graphite that were used for the calculations are shown in Table 3.1. The thickness of the graphite layer is chosen in such a way that its volume is equivalent to the average graphite volume in the fuel zone of the pebble per particle. For a pebble with 15,000 fuel particles and an outer radius of the OPyC of $r_4 = 0.0465$ cm, the graphite equivalent layer thickness is 0.058 cm and $r_5 = 0.105$ cm. In Fig. 3.2 it is shown that the presence of the graphite

Table 3.1: Values used [76] for evaluating the effects of graphite dimensional change.

Item	Value	Unit
Kernel diameter	500	μm
Buffer thickness	95	μm
IPyC thickness	40	μm
SiC thickness	35	μm
OPyC thickness	40	μm
Young's modulus of PyC	$3.96 \cdot 10^4$	MPa
Young's modulus of SiC	$4.0 \cdot 10^5$	MPa
Young's modulus of C matrix	$1.05 \cdot 10^4$	MPa

material has a significant effect on the tangential stress in the SiC layer. High tensile stresses are found in the early stage of the irradiation for cases in which the graphite has a low irradiation creep constant. Taking a high value for the creep constant reduces the tangential stress and the corresponding solution tends to the solution for a particle without the additional graphite layer. In reality, the graphite matrix experiences irradiation-induced dimensional changes as well as thermal expansion [95]. Measurements on the dimensional change of graphite have been performed during operation of the AVR reactor [95], by measuring the pebble diameter. In Fig. 3.4 the dimensional change rate remains negative, while others have found that for some graphite material and irradiation conditions (temperature and dose rate) a turn-around exists beyond which the dimensional change rate becomes positive [96].

Using the results in Fig. 3.4, the effect of graphite matrix dimensional change on the SiC tangential stress is shown in Fig. 3.3. The continuous line presents the case without dimensional change of the graphite matrix, while the dashed lines represent cases with dimensional change for various creep constants of the graphite matrix. Note that the creep constant of the pyrocarbon material is kept at a fixed value of $3.0 \cdot 10^{-29} (\text{MPa} \cdot \text{m}^{-2})^{-1}$.

3. Performance of coated particle fuel in High Temperature Reactors

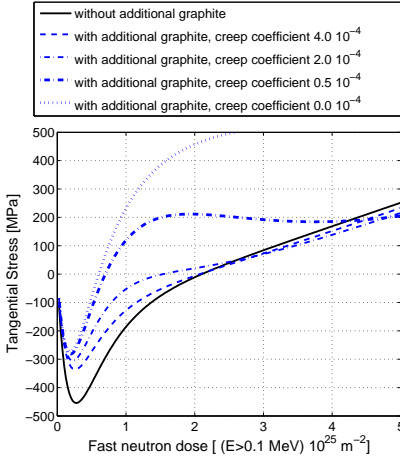


Fig. 3.2: Effect of the presence of graphite matrix on the SiC tangential stress (excluding dimensional change of graphite). The solid line represents the case without the additional graphite layer, the dashed/dotted lines represent the cases with a graphite layer for several values of the irradiation creep coefficient (in $(\text{MPa} \cdot 10^{25} \text{m}^{-2})^{-1}$).

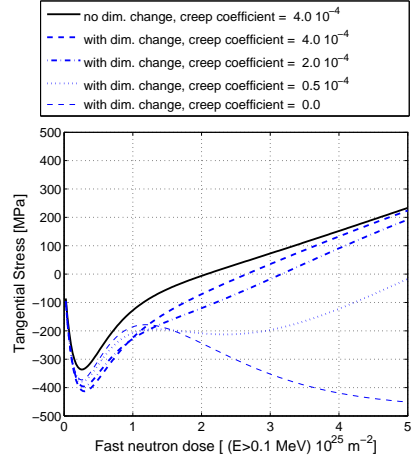


Fig. 3.3: Effect of the graphite matrix dimensional change on SiC tangential stress for several values of the irradiation creep coefficient (in $(\text{MPa} \cdot 10^{25} \text{m}^{-2})^{-1}$).

For the extreme case in which the dimensional change of the graphite matrix is not included, the fourth layer is counteracting the dimensional change of the OPyC layer, thereby reducing its compressive effect on the tangential stress of the SiC layer in the beginning of the irradiation (see Fig. 3.2). For an increased creep coefficient this counteracting effect is reduced, and even more so, if the graphite matrix is shrinking itself (Fig. 3.3). In the other extreme case in which the dimensional change of the graphite matrix is included without including irradiation creep of this layer (Fig. 3.3), the shrinkage of the graphite matrix results in a high compressive tangential stress during the entire calculation domain.

For all cases the dimensional change rate of the graphite layer has a significant impact on the tangential stress of the SiC layer, which determines the failure probability of the particle. The time at which the tangential stress becomes tensile depends on the value of the creep coefficient of the graphite matrix.

Inter-particle stress effects

We will now address the effect of the stresses coming from neighboring particles in the graphite matrix. In practical cases the radial and tangential stress components

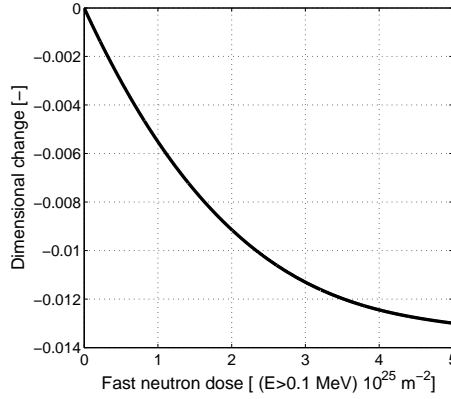


Fig. 3.4: Dimensional change of a pebble in the AVR, taken from reference [95].

originating from these neighbors differ in magnitude and sign (compression or tension). In Fig. 3.5 the position on a TRISO surface, determined with radius R and angles θ and φ , is denoted with P . At this position on the particle surface, radial and tangential stresses are present, resulting from the particle itself. The radial stress component has the direction of line OP . Furthermore, radial and tangential stresses coming from a neighboring particle at a distance d , with its center at O' , are also acting on point P . The direction of the radial stress of the neighboring particle is along line $O'P$. It must be kept in mind that in practical cases the radius of the particle is in the same order of magnitude as the distance d , for the closest neighbors. The magnitude of the radial and tangential stress components can be calculated with Eqs. (3.36) and (3.37), respectively, in which r is equal to $O'P$. In order to calculate the total

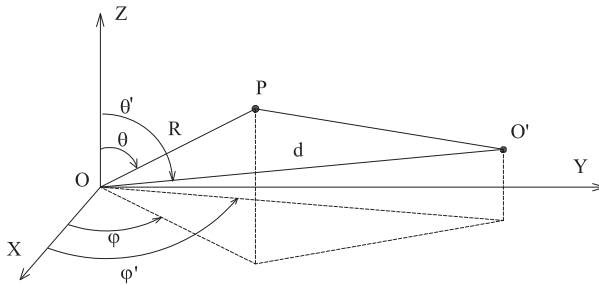


Fig. 3.5: Orientation of a TRISO particle at O and its neighbor at P' .

3. Performance of coated particle fuel in High Temperature Reactors

stress field, the stress components (σ') from the neighbor can be transformed to a stress tensor in the coordinate system of the given particle (σ), with:

$$\sigma = \mathbf{L}\sigma'\mathbf{L}^T \quad (3.38)$$

in which \mathbf{L} is the transformation matrix, consisting of the direction cosines between the two coordinate systems [92, 97].

This procedure is applied to several neighboring particles, assuming that all neighbors have the same stress state and that the stresses can be superimposed. Because the creep strain derivative depends on the actual stress itself, the creep effect leads to non linear behavior of the stress in time (see Eqs. (3.7) and (3.8)). Therefore, the actual combined stress from multi-particle effects should result in slightly more creep strain (and consequently more stress relief in the graphite) than will be calculated from summing individual particle stresses.

From Eqs. (3.36) and (3.37) it can be seen that the magnitude of the stress reduces with the inverse of the cubed distance. However, the number of neighboring particles at a given distance increases with the distance squared. Therefore, neighbors that are within considerable distance of the particle considered, have to be considered.

It is first considered that the particles are distributed regularly in the matrix material. Fig. 3.6 shows a cubic distribution of particles, but a hexagonal and a random distribution are also considered in this chapter. The combined maximum principal stress resulting from all neighbors within a certain distance is presented in Fig. 3.7 for a cubic distribution of the neighbors.

The inter-particle stress effect is determined by calculating the principal stresses for several points on the surface of the particle. In Fig. 3.7 the maximum principal stress is presented as a function of the distance from the particle. With increasing distance, the number of neighbors to be taken into account increases, assuming that the particle considered is at the center of the pebble. At a large distance the stress effects from the neighbors becomes small. However, the distance from which the contribution to the total stress effect can be neglected is relatively large with regard to the particle diameter. On the other hand, a large part of the effect is determined by the closest neighbors. This can also be concluded from the stress effect for randomly distributed neighbors. The standard deviation from the average stress effect is also presented in Fig. 3.7 and shows a large spread, especially for short distances. In a random distribution, a neighbor can be at short distance from the particle, which results in a large effect on the stress. This can explain why the random distribution gives the highest inter-particle stress, resulting in an increase of 40% of the radial stress at the surface of the particle. The above calculations were performed for a pebble containing 15,000 TRISO particles. Fig. 3.8 shows the dependency of the relative maximum principal stress on the number of particles contained in the pebble (for a cubic distribution, considering neighbors within a distance of 0.3 cm). One can see that the stress effect has a nearly linear dependency on the particle packing

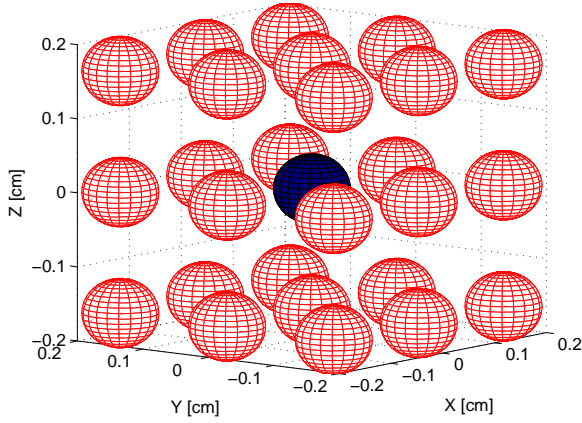


Fig. 3.6: Position of neighboring fuel particles (light) with regard to a given particle (dark) for a cubicle lattice.

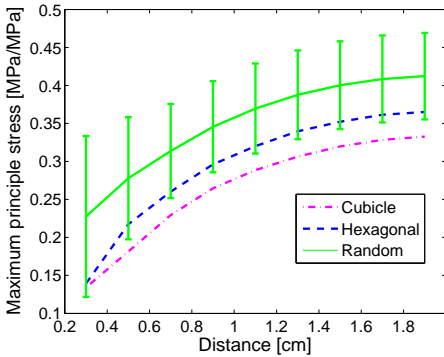


Fig. 3.7: Maximum principal stress normalized to a radial stress of 1 MPa at the surface of the TRISO particles, resulting from neighbors within the specified distance from the particle.

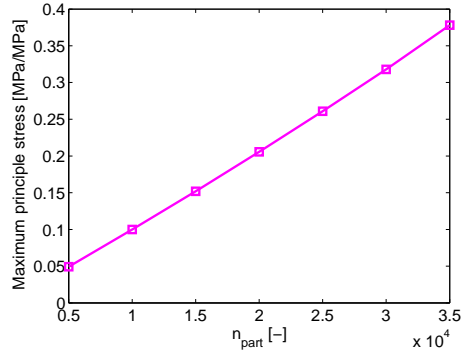


Fig. 3.8: Maximum principal stress as a function of the number of particles in a pebble.

fraction. In the above analysis it is found that the inter-particle stress effect is about 40 % of the radial stress at the outer surface of a particle for a pebble containing 15,000 randomly distributed TRISO particles. We will now turn to the model of a single particle to quantify the impact of this stress on the tangential stress in the SiC.

Fig. 3.9 shows the radial stress at the surface of a single particle during irradiation, calculated with the 4-layer model and assuming the same conditions as in section

3.3 (excluding the effect of the graphite matrix dimensional change). To quantify the

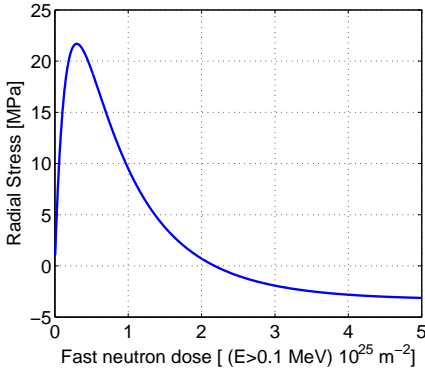


Fig. 3.9: Radial stress at the outer surface of the OPyC layer of a TRISO particle during irradiation.

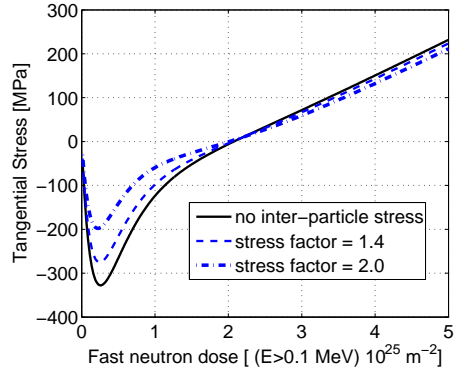


Fig. 3.10: Tangential stress of the SiC layer for several values of radial stress increase acting on the outer surface of the particle.

inter-particle effect, the radial stress presented in Fig. 3.9 is used in a 3-layer model as a boundary condition to calculate the effect on the maximum tangential stress in the SiC layer. The radial stress at the surface is therefore increased by a factor between 1 and 2, to represent the stress effects of the neighboring particles. It must be noted that this is a first approximation of the inter-particles stress effect. In reality the stress field on the surface of the particle, resulting from neighboring particles, will not exactly be radially uniform.

The results of the calculations are shown in Fig. 3.10. It can be seen that there is a small effect on the SiC tangential stress for the case of 40 % stress increase (factor 1.4), especially at the beginning of the irradiation. In general the tangential stress is reduced for this irradiation case, being either less compressive or less tensile. It can therefore be concluded that the impact on the failure probability of the particle is small for the reference packing fraction.

3.4 Stress analysis of coated particle fuel in current and future HTRs

Two applications of PASTA to present-day HTR fuel designs are carried out. In the first application a code to code comparison is made for the first fuel loading of the HTTR to verify the results of PASTA. Furthermore, the effect of the graphite matrix on the coating stresses is quantified. The second application is the PBMR-400 design (see Sec. 1.3) for which the effect of the fuel temperature on the coating stress is investigated.

Table 3.2: *Properties of particle fuel in HTTR irradiation experiment*

Item	Value	Unit
Fuel density	10.7	$\text{g}\cdot\text{cm}^{-3}$
Enrichment	9.17	%
Kernel diameter	600	μm
Buffer thickness	60	μm
IPyC thickness	30	μm
SiC thickness	25	μm
OPyC thickness	45	μm
Fuel temperature	1573	K
EOL fast fluence	$3.0\cdot 10^{25}$	m^{-2}
EOL burnup	66	GWd/t
Irradiation time	100	days
SiC median strength	834	MPa
Weibull modulus (SiC)	8.0	-

Stress analysis of the first fuel loading of the HTTR

PASTA is applied to the irradiation experiment of the first fuel loading of the High Temperature Engineering Test Reactor (HTTR) [82] and compared with stress analysis calculations performed by Sawa et al. [82] and with the TIMCOAT code [75]. The data used for this calculation are presented in Table 3.2. In comparison with Table 3.1 the HTTR particle has a larger kernel, but thinner buffer -and SiC layers, which is expected to result in larger stresses for similar irradiation conditions. Furthermore, the temperature for the HTTR experiment is relatively high, which will increase the stress even more.

Cases with and without the effects of the dimensional change of the graphite matrix and inter-particle stress are considered to see whether the presence of the graphite matrix has an effect on the failure probability. Fig. 3.11 shows that the results for the tangential stress in the SiC layer obtained with the PASTA code are in good agreement with the other two codes. At the beginning of irradiation, shrinkage of the PyC layers causes compressive (negative) tangential stresses in the SiC layer and positive tangential stresses in the PyC layers. This negative stress turns positive half way through the irradiation by buildup of internal pressure caused by gaseous fission products and CO gas. The differences in the position and magnitude of the minimum SiC tangential stress are directly due to the different equations for the irradiation induced dimensional change in the PyC layers introduced in the present model, by Sawa et al. and in the TIMCOAT code. Furthermore the creep coefficients used in the calculations of Refs. [82, 75] for these layers was unknown. The stress calculated by Sawa et al. increases almost linearly, after a decrease at the beginning of irradiation. It is likely that a linear approximation was used to describe the stress during this

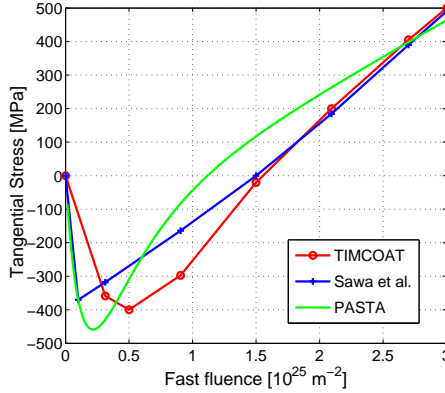


Fig. 3.11: Tangential stresses in the SiC layer calculated with PASTA, TIMCOAT [75] and by Sawa et al. [82], for the HTTR fuel during irradiation.

irradiation interval.

The effects of graphite dimensional changes are now analyzed by adding a graphite layer to the model with a thickness of $400 \mu\text{m}$. This thickness corresponds to the packing fraction of particles in an HTR using prismatic fuel, equivalent to the packing of 30,000 particles in a pebble, following the same calculation method for the thickness as in section 3.3. The fuel particles experience the same irradiation conditions as in the HTTR fuel experiment. The results for the coating stresses are presented in Fig. 3.12.

It is shown that the above mentioned phenomena have an effect on the tangential SiC stress. The graphite compensates for the shrinking of the PyC layers at the beginning of the irradiation, because its tangential shrinking rate is smaller than that of the PyC layers, resulting in a reduced compressive stress on the SiC layer. When irradiation progresses the isotropically shrinking matrix material offsets the stress induced by the radial swelling of the PyC layers. The particle is compressed by the matrix material, which reduces the tensile tangential stress in the SiC layer.

Finally, the failure probabilities of the SiC have been calculated, by use of Eq. (3.6). It is found that the failure probability is $5.0 \cdot 10^{-3}$ for the 3-layer coated particle and $1.4 \cdot 10^{-4}$ for the 4-layer particle including dimensional change of the graphite matrix. The reduction in failure fraction results from a reduction in the tensile tangential stress of the SiC layer for the case with an additional graphite layer.

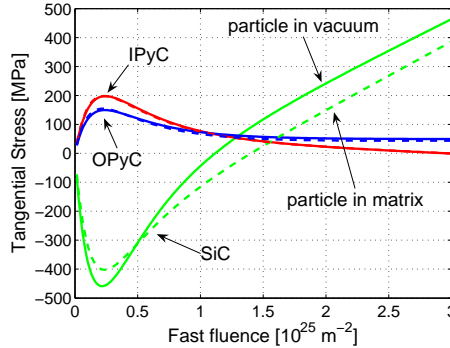


Fig. 3.12: Tangential stresses calculated with the PASTA code for the HTR experiment for a particle in vacuum (solid lines) and a particle in the graphite matrix (dashed lines). For these two cases a large difference exists between the SiC stresses.

Stress analysis of particle fuel in a 400 MW_{th} Pebble-Bed HTR

As a second application, PASTA is used to calculate stresses in the fuel of a 400 MW_{th} Pebble-Bed HTR based on the PBMR-400 design. Data concerning this reactor are taken from reference [71] and the general design characteristics were presented in Chap. 2.

Simplifications were used in the neutronic model, i.e. the void regions, control rods and reactor vessel were not modeled explicitly. By using the procedure described in section 3.1, the neutron flux, burnup, power and temperature profiles were calculated. Results are presented in Figs. 3.13 to 3.16. A coupled thermal hydraulics - neutronics calculation was performed using temperature dependent neutron cross sections and assuming a fixed reactor power, resulting in a k_{eff} of 1.0260. In the actual PBMR design, the presence of the control rods at the top of the side reflector results in a harder neutron energy spectrum and a shift of the neutron flux peak away from the top (Fig. 3.13). In Fig. 3.14 the burnup level of the pebbles during irradiation is presented. During each cycle the pebbles reach considerably higher burnup, especially after the first cycle. The calculated power profile (Fig. 3.15) causes the maximum fuel temperature to rise quickly from top to bottom in the pebble bed, before reaching a maximum value and decreasing slowly towards the bottom.

The pressure in the fuel particle and resulting tangential stress during irradiation are shown in Figs. 3.17 and 3.18, respectively. The pressure in the buffer layer increases during each cycle, due to an increasing amount of gaseous fission products in the buffer and to the high temperatures at the bottom region of the reactor core. At the beginning of each cycle the pressure is relatively low since the pebble is located in the relatively cool top region of the core.

3. Performance of coated particle fuel in High Temperature Reactors

On one hand, the inter-particle stress effects result in an additional radial tensile stress on the surface of each particle during irradiation. This causes a slight increase in the (tensile) tangential stress in the SiC layer at the end of the irradiation. However, the dimensional change of the graphite matrix causes a more important reduction in the tangential stress in the SiC layer (Fig. 3.18).

One can conclude from the results presented in Fig. 3.18 that for both cases (with or without graphite matrix stress effects), the SiC layer remains in compression. Therefore the SiC layer does not fail directly from pressure buildup in the buffer layer. However, it has been shown that the SiC layer can fail indirectly after cracking of the PyC layers [75, 98], which results in a high local tensile stress around the crack tip.

During accident situations the temperature in the reactor may increase, resulting in increased pressure in the buffer layer and possible tensile stress in the SiC layer. This leads to an increased failure probability of the SiC layer, especially at the end of the irradiation period. The presence of the graphite layer reduces this tensile stress resulting in a lower failure probability of the SiC layer during the transient.

Fig. 3.18 shows that the tangential stresses in the IPyC and the OPyC layers are almost unaffected by the presence of the graphite. Consequently, the failure probability of these layers by cracking of the pyrocarbon material is also unaffected.

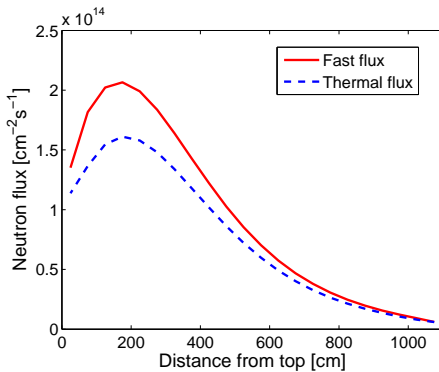


Fig. 3.13: Axial neutron flux profile in the pebble bed.

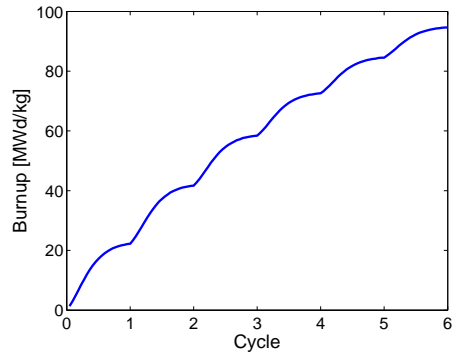


Fig. 3.14: Fuel burnup during irradiation (pebbles are cycled six times through the core).

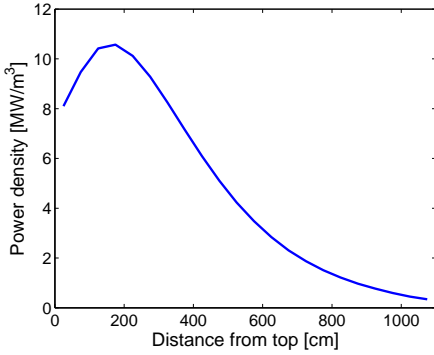


Fig. 3.15: Axial power profile in the pebble bed.

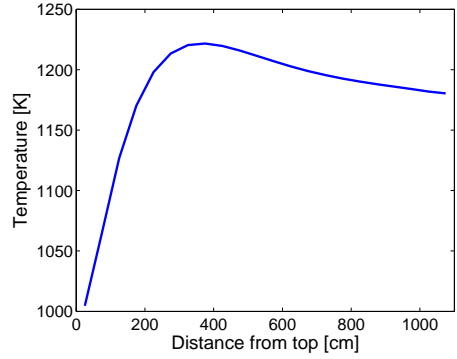


Fig. 3.16: Maximum fuel temperature profile in the pebble bed.

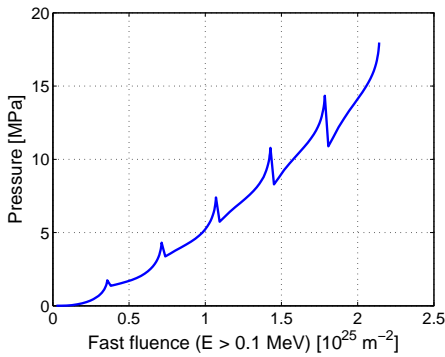


Fig. 3.17: Pressure in the buffer layer of a fuel particle in the center of a pebble during irradiation.

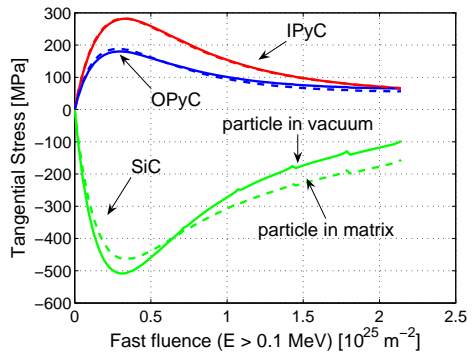


Fig. 3.18: Tangential stresses in particle coatings during irradiation, for two cases: a single three-layer coated particle in vacuum (solid lines), a three-layer coated particle in matrix material, which includes interparticle stress and graphite matrix dimensional change (dashed lines).

Effect of increased operating temperature on the fuel performance

From the previous section it was found that operating the reactor with a helium outlet temperature of 900 °C would not lead to a direct failure of the SiC layer. From Fig. 3.18 it can be seen that there exists a significant margin for the tangential stress of the SiC layer to become tensile. Therefore, an increase of the helium outlet temperature (and reactor power) for a fixed helium inlet temperature and mass flow

would be permissible.

In Fig. 3.19 the effect of the temperature increase on the final tangential stress in the SiC and the corresponding failure probability can be seen. Increasing the operating temperature increases both the diffusion of fission products (see. Eq. (3.1)) and the pressure in the buffer layer (see Eq. (3.3)). With increasing temperature, the SiC tangential stress becomes less compressive and turns to a tensile stress at a helium outlet temperature of approximately 1075 °C.

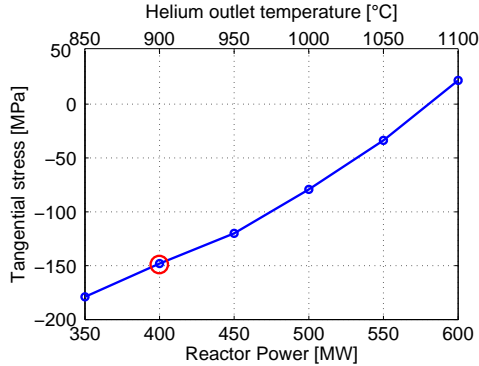


Fig. 3.19: Impact of the helium outlet temperature on the SiC tangential stress and the failure probability. The circle shows the operating condition of the reference design.

3.5 Conclusion

A stress analysis code was developed to analyze stresses in coated particle fuel of High Temperature Reactor pebble bed designs. Existing analytical stress analysis models for coated particle fuel were expanded with an additional layer in order to take into account stress effects due to dimensional change of the graphite matrix in which the coated particle fuel is embedded and stress effects of neighboring particles.

Shrinkage of the graphite matrix during irradiation results in a higher compressive tangential stress of the SiC layer for high neutron dose levels compared to a particle in vacuum, which is in general beneficial for particle endurance. This effect is similar to the effect that the shrinking pyrocarbon layers have on the SiC layer. However, for certain types of graphite and temperature ranges, the shrinkage turns to swelling, which leads to an increase in particle failure at high irradiation dose. It is therefore important to have good knowledge on the dimensional change and creep of the graphite matrix for analyzing stresses in coated particle fuel.

As a first approximation, the stresses coming from neighboring particles are modeled as a uniform stress on the outer surface of a given fuel particle. In reality the

stress on the outer surface will likely be non-uniform. An investigation of the effect of the non-uniform stress field on the stresses in the particle using a finite element code is considered to be part of future work. Furthermore, the calculation procedure for inter-particle stress effects might be improved by taking into account the nonlinear behavior of the creep in the summation of the individual stresses from neighboring particles. At high packing fractions, the neighboring particles can have a significant effect on the stress state of a given particle, which can result either in an increase or a decrease of the particle failure probability.

The stress analysis code was applied to an irradiation case of HTTR fuel. The tangential stress in the SiC layer calculated with PASTA and the corresponding failure probability were comparable with results from Sawa et al. [82] for the 3-layer model. A significant impact of the presence of the graphite matrix was encountered using the 4-layer model. The failure probability of the SiC layer was found to be $5.0 \cdot 10^{-3}$ for a particle in vacuum, while a value of $1.4 \cdot 10^{-4}$ for a particle in graphite matrix was found. This is caused by shrinkage of the graphite matrix which results in a reduction of the (tensile) tangential stress in the SiC layer.

In the application of PASTA to a 400 MW_{th} HTR based on the PBMR-400 design it was found that the SiC layer remains in compression during the entire irradiation period in the reactor. The presence of the graphite matrix results in an even higher compressive tangential stress in the SiC layer. For this reason an increase in the operating temperature is allowable. An analysis of a VHTR design with increased helium outlet temperature shows that up to a temperature of 1075 °C the SiC layer remains in compression. This shows that a VHTR Pebble-Bed based on the PBMR-400 with an helium outlet temperature of 1000 °C will not exhibit any direct failure of the SiC layer during normal operation.

However, it is expected that shrinkage induced cracking of the PyC layers, due to tensile stresses in the beginning of the irradiation, can lead to possible failure of the SiC layer [98, 99]. Furthermore, it has been shown in Chap. 2 that the fuel temperatures are elevated with several hundred degrees during a LOFC accident. It is therefore desirable to have a significant margin of compressive stress, which could be generated by reducing the temperature during normal and accident conditions. Modifications of the reference design are presented in the following chapters that result in lower fuel temperature and therefore larger safety margins.

3. Performance of coated particle fuel in High Temperature Reactors

4

Fuel management optimization for pebble-bed reactors

From Chaps. 2 and 3 it was found that a reduction of the power peak in the core is attractive to decrease the maximum fuel temperature and to increase fuel performance. In this chapter a calculation procedure is described, which combines fuel depletion, neutronics and thermal-hydraulics to investigate the impact of a several pebble (re)loading schemes in an attempt to reduce this temperature in the present PBMR design.

4.1 Fuel management in pebble-bed reactors

Current pebble-bed reactor designs, such as the HTR-PM and the PBMR, include an inner and outer graphite reflector. The employment of an inner reflector avoids a power peak at the center of the pebble-bed and adds additional thermal capacity to the core, which is beneficial during accident situations. The power profile in the annular pebble bed can exhibit peaks near these reflectors caused by the local abundance of thermal neutrons. Furthermore, the tall core geometry, adopted for thermal-hydraulic reasons, causes a large difference in the burnup level between top and bottom of the core, resulting in an axial power peak at the top.

By using several pebble inlet positions at the top of the core the pebble distribution and therefore the nuclide distribution over the core can be influenced. The power profile can be influenced in the radial direction by systematically placing pebbles with different enrichment or fertile content at a different radial starting position. In the extreme case, a central reflector can be formed using pebbles without fuel for the inner core zone [16]. Experiments were conducted in the past using several pebble types and inlet positions during the operation of the AVR reactor [7].

The axial power profile can be modified by recycling the pebbles several times through the core. This multiple recycling scheme has a secondary advantage, since it

provides the reactor designer with pebbles containing different amounts of fissile nuclides. By recycling these pebbles at different radial reloading positions, for example by placing fresh pebbles in the outer region of the core, it is possible to modify the radial power profile while omitting the use of pebbles with different enrichments or burnable poison [100].

Optimizing the pebble loading pattern, thereby improving the power profile, is expected to reduce the fuel temperature for a fixed helium outlet temperature. In this chapter a calculation tool is used to evaluate several pebble loading schemes. The effect of the improved power profile on the fuel temperature is quantified. The methodology for the calculation of the equilibrium nuclide concentration in the core is presented in Sec. 4.2. The effect of pebble recycling on the axial power profile of this reactor is described in Sec. 4.4, followed by an investigation of the effect of radial fuel zoning on the radial power profile (Sec. 4.5) and the temperature profile (Sec. 4.6). Furthermore, an optimization routine is used to find the optimal pebble loading pattern for cores with multiple fuel zones. In Sec. 4.7 conclusions are drawn on the possibility of operating present reactor designs at elevated temperatures by using an improved fuel management scheme.

4.2 Determination of the equilibrium core composition and power profile

In this section a calculation procedure is presented which determines the equilibrium nuclide concentration in the core, from which the power and temperature profile can be derived. This calculation tool is used to analyze the design modifications to the reference design.

The general equation for fuel depletion, including fuel movement, is as follows [63]:

$$\frac{DN_i}{Dt} = \sum_{j \neq i} (\phi \gamma_{ji} \sigma_{aj} + \alpha_{ji} \lambda_j) N_j - (\phi \sigma_{ai} + \lambda_i) N_i \quad (4.1)$$

where,

$\frac{DN_i}{Dt}$ = the material derivative of nuclide i

N_i = atomic concentration of nuclide i

ϕ = neutron flux

γ_{ji} = probability that a neutron interaction with nuclide j will yield nuclide i

σ_{aj} = absorption cross section of nuclide j

α_{ji} = probability that the decay of nuclide j will yield nuclide i

λ_j = decay constant of nuclide j

σ_{ai} = absorption cross section of nuclide i

λ_i = decay constant of nuclide i

Eq. (4.1) is evaluated assuming that each pebble is irradiated with a fixed flux level during a certain time interval, when it moves from one point in the core to the next. To account for the variation in the flux profile, the core is divided into several regions. For example, in the analysis of the PBMR in Sec. 4.3, 22 axial flux regions are used.

In a pebble-bed reactor, operation starts from an initial core composition in which pebbles with various fuel content or burnable poison are used. A certain loading strategy is applied consistently during operation and the core reaches an equilibrium composition. The equilibrium core contains pebbles of various burnup levels and its composition is therefore different from the initial core.

Similar to what is done in Ref. [51] we try to find the asymptotic nuclide distribution directly, without calculating any intermediate distribution. Assuming we have reached this equilibrium core, the neutron flux profile ϕ does not change in time. Instead of adopting the analytical approach [51], a numerical calculation scheme, similar to [101], was adopted using existing codes.

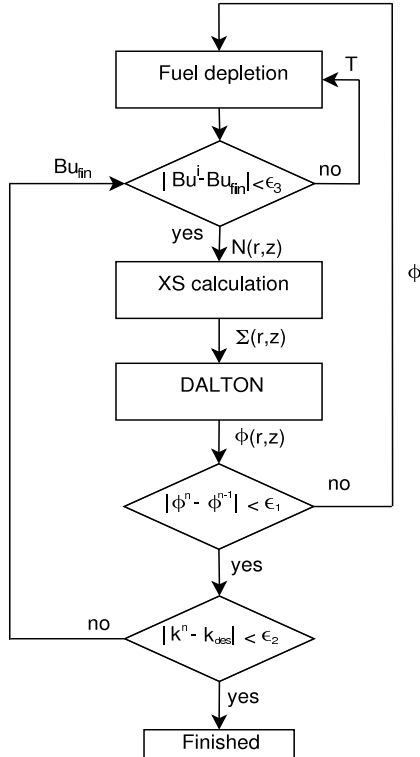


Fig. 4.1: Flow scheme of calculation procedure for the calculation of the power profile in the core.

The outline of the calculation method is presented in Fig. 4.1 and consists of several codes. The codes are used iteratively until convergence is reached on both inner and the outer iteration. The criterion for the inner loop is the change in the neutron flux, convergence on the outer loop is determined by the deviation from a preset k_{des} value. The final burnup level of the pebbles, Bu_{fin} , is modified to meet this criterion. The total residence time T that the pebbles remain in the core is modified in turn to reach this burnup level. The inner loop of the program consists of the following steps:

Fuel depletion calculation:

Provided the flux profile in the core is known, resulting from a certain pebble recycling scheme, the depletion of the fuel in the pebble during its lifetime can be calculated. To this end the core is divided into several discrete radial and axial zones in which one or more pebble burnup classes can be present. The actual depletion calculation is performed using the ORIGEN-S module [102] from the SCALE-5 code system [55]. Between burnup steps the cross sections are updated using successive 1D transport calculations for the TRISO and pebble geometry. To this end a 172 energy group XMAS library is used based on the JEFF3.1 library. The nuclide distribution over the core is known after the calculation of each burnup interval.

It is noted that the pebbles are allowed to pass through the core several times using a given (re)loading strategies. Therefore, it is possible that pebbles having different nuclide densities are located at the same position.

Calculation of the neutron cross sections:

Zone averaged nuclide concentrations $N(r, z)$ are now used for generating neutron cross sections for the entire reactor geometry using the calculation procedure of Chap. 2.

DALTON:

The neutron cross sections are used to calculate the two dimensional multi-group flux profile $\phi(r, z)$ with DALTON. Average fluxes are generated for each fuel depletion zone and scaled to the desired reactor power. The k_{eff} of the reactor is calculated.

Once the nuclide distribution over the core is known and the cross section generation step is applied for several temperatures of the fuel and moderator a temperature dependent cross section library is generated. This library can be used in coupled neutronic and thermal-hydraulic calculations using the DALTON-THERMIX code system [103]. In this way a temperature corrected power profile can be calculated.

4.3 Possible modifications of the pebble recycling scheme

The method described in the Sec. 4.2 is used to determine the nuclide distribution over the core and the corresponding power and temperature profile. The final burnup level for the pebbles was set to 95 MWd/kg, which is reached after a total residence time of approximately three years. This resulted in a k_{eff} of 1.0260, allowing for some positive reactivity for the controllability of the reactor, in the event of xenon poisoning. The shape of the power profile is similar to the power profile (see Chap. 2) of the DALTON-THERMIX calculation using cross sections that were generated with VSOP [56] in the framework of the OECD-NEA PBMR400 benchmark [104]. The maximum power density for this calculation was 10.55 MW/m³ and the k_{eff} for a case in which the control rods were withdrawn was 1.027. The peak of the power profile for the case with the VSOP cross sections moves to a lower position of the core since it was assumed for the depletion analysis that the control rods in the top of the outer reflector were partly inserted.

Fig. 4.2 shows the burnup as a function of the pebble pass through the core. The burnup level increases with each pass, while the difference in burnup level between two consecutive passes decreases. The burnup level shows a large increase at the beginning of each pass resulting from a peak in the flux profile in the top region of the core. Figs. 4.3 and 4.4 show the power density and fuel temperature profile

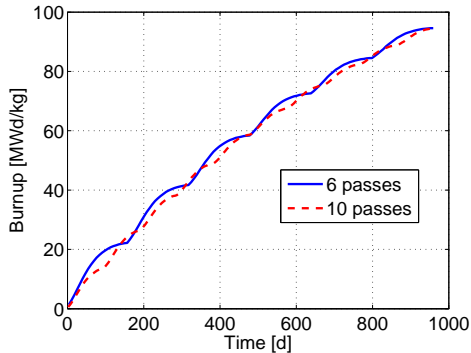


Fig. 4.2: Burnup level of a pebble as a function of the irradiation time. The evolution for both a total of 6 and 10 pebble passes is shown, while the final burnup remains 95 MWd/kg.

respectively. From these figures the following is remarked:

1. There are two power peaks located at the top of the core (Fig. 4.3), because this region has fuel with a higher fissile content. A large peak in the power density is unattractive in the case of a LOFC, since the maximum fuel temperature in the absence of cooling will be largely determined by this peak. On the other hand, the fuel temperatures (Fig. 4.4) in the bottom region are high compared

4. Fuel management optimization for pebble-bed reactors

to the top region, because the coolant flow direction is from top to bottom. This indicates that increasing the power density at the top might result in a decrease of the maximum fuel temperature during normal operation.

2. The power profile is even more elevated near the inner and outer reflector boundaries. The maximum power density is found at the inner boundary of the pebble bed ($R = 100$ cm, $Z = 250$ cm). This results in a large difference (> 85 °C) in the fuel temperature between the outside and inside of the core (Fig. 4.4).

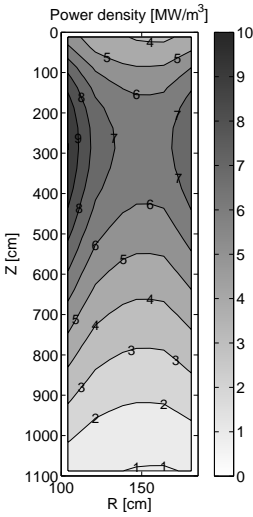


Fig. 4.3: Power profile during normal operation showing peaks in the top region of the core near the inner and outer reflectors.

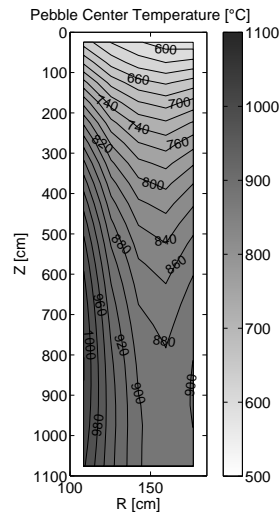


Fig. 4.4: Profile of pebble center temperatures during normal operation showing that the maximum value is located near the inner reflector at the axial center of the core.

The following design solutions are proposed, with regard to the maximum fuel temperature, respectively to the above mentioned items:

1. Changing the number of pebble passes from the six passes used in the reference to re-distribute the fissile material over the core height. Increasing the number of passes would spread the fissile material more homogeneously and would reduce the axial power peak, while decreasing the number of passes will elevate the power peak in the top region.
2. Adopting several radial fuel zones, thereby redistributing the fissile material in the radial sense in order to flatten the radial power profile and reduce the fuel temperature.

4.4 Impact of multiple pebble recycling on the reactor performance

In order to flatten the axial power peak, pebbles are recycled several times through the core before disposal. The effects on the axial power profile and (fuel) temperatures are analyzed, using the procedure from Sec. 4.2, for normal operation as well as for a DLOFC accident.

Normal operating conditions

The effect of the total number of pebble passes on the power profile and temperature profiles can be seen in Figs. 4.5 and 4.6. The total number of pebble passes ranges from one to ten. The shape of the profile changes from an exponential shape for one pass toward a more cosine shaped curve for ten passes. This is caused by the fact that the fissile material is spread more evenly over the core height and the burnup difference per pass decreases (see Fig. 4.2). The power peak reduces and shifts towards the center of the core with increasing number of pebble passes steps. Consequently, the location of the maximum fuel temperature also moves towards the bottom of the core. Furthermore, the shape of the fuel (pebble center) temperature profile changes into a gradually increasing function from the top to the bottom of the core (Fig. 4.6). From Fig. 4.7 it can be seen that increasing the number of passes

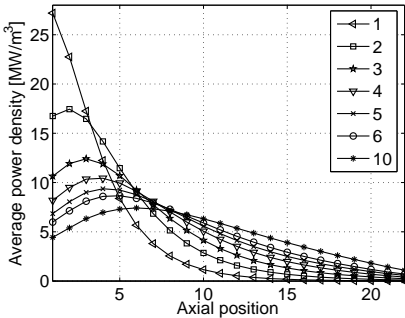


Fig. 4.5: *The axial power profile as a function of the axial position with the total number of pebble passes as a parameter. It can be seen that the power profile flattens with increasing number of passes.*

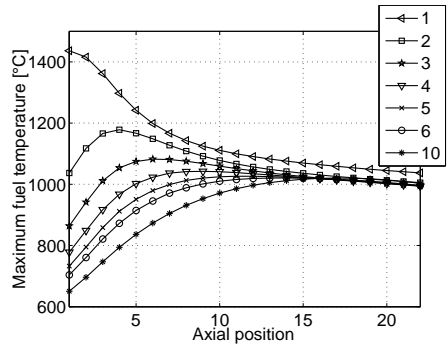


Fig. 4.6: *The maximum fuel temperature as a function of the axial position with the total number of pebble passes as a parameter. The location of the maximum value moves from the top towards the bottom of the core (from left to right in the graph) with increasing pebble passes.*

beyond six is not advantageous with regard to the maximum fuel (pebble center) temperature during normal operating conditions. The graph also shows a significant

increase in the maximum fuel temperature with increasing reactor power, for a fixed helium inlet temperature and mass flow. The size of the increase is weakly dependent on the number of passes. Depending on the design limit on the maximum allowable fuel temperature, the reactor power can be increased in order to increase the helium outlet temperature, resulting in a helium outlet temperature of 1000 °C at a reactor power of 500 MW.

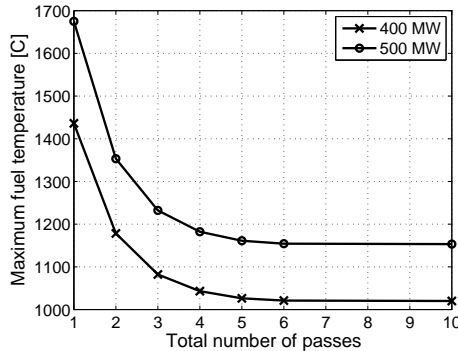


Fig. 4.7: Maximum fuel temperature during normal operation as a function of the total number of pebble passes for both 400 and 500 MW reactor power.

Depressurized Loss Of Coolant conditions

In Chap. 2 the (DLOFC) accident has been analyzed. In this transient, which can be considered as a worst case scenario for an HTR, a pipe break or leak in the primary system causes a fast depressurization of the core. Although the effects of the DLOFC accident are limited by the negative reactivity feedback and the capability of the reactor to transfer the decay heat from the core, fuel temperatures are considerably higher compared to normal operating conditions. The temperature profile in the reactor differs greatly from that during normal operation. The highest temperatures are in this case located in the region of the power peak (Fig. 4.8). Reducing this peak by increasing the number of pebble passes can therefore be effective in reducing this temperature. The effect of pebble recycling on the maximum temperature during the DLOFC transient has been investigated. The power profiles that have been derived in Sec. 4.4 for the different recycling schemes are used in THERMIX calculation to perform a DLOFC transient. In this thermal-hydraulic standalone calculation a reactor scram is assumed in the beginning of the transient, which results in a slightly lower temperatures compared the temperature encountered in Chap. 2. Furthermore, the reactor does not reach re-criticality. The result of the maximum fuel temperature during the transient as a function of the total number of passes is shown in Fig. 4.9 for both a 400 and 500 MW reactor design. Since the power profile is flattened with

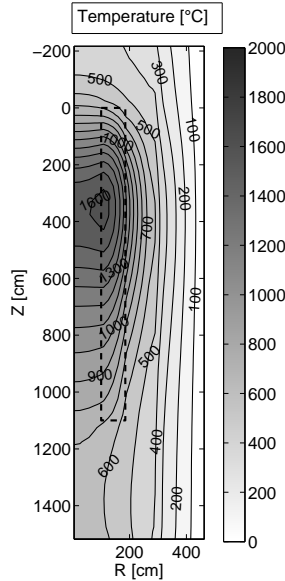


Fig. 4.8: Fuel and solid structure temperatures in the reference design during a DLOFC transient at the time point of the fuel maximum temperature. The core region is shown with a dashed line. Note that the maximum value is located near the power peak at the inner reflector.

increasing total number of pebble passes, the maximum fuel temperature during the transient is reduced. It can be concluded from Fig. 4.9 that the effect becomes smaller with increasing number of passes, but that the reduction in the fuel temperature from six to ten passes for the transient case is still considerable (100 °C).

Fig. 4.9 shows that increasing the reactor power from 400 to 500 MW with the aim of increasing the helium outlet temperature to 1000 °C results in an increase of the maximum fuel temperature during a DLOFC transient with roughly 200 °C. The cases with less than five pebble passes are not investigated for a 500 MW reactor since already for the 400 MW design too high temperatures were encountered.

4.5 Impact of radial fuel zoning on the reactor performance

In Sec. 4.3 it was identified that the radial power profile has peaks near the inner and outer reflector. In an attempt to reduce these peaks, the core is divided into several radial regions. It is assumed that the pebbles follow straight vertical flow lines and that radial mixing is limited as was observed in experiments [105]. Therefore no special arrangements have to be made for the guidance of the pebbles except for the placement of the pebbles on the top of the core.

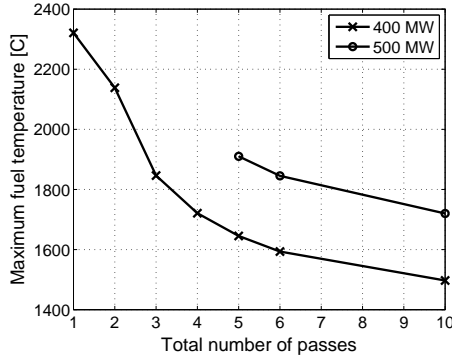


Fig. 4.9: Maximum fuel temperature occurring in a DLOFC transient as a function of the total number of passes for two values of the reactor power (400 and 500 MW).

In Sec. 4.4 it was found that using a total of ten pebble passes is advantageous with regard to the maximum fuel temperature during a DLOFC case. Therefore, this total number of passes (N_{tot}) is adopted throughout the following analysis for the radial zoning.

Fuel zoning effects

To illustrate the effect of radial fuel zoning in pebble bed reactors, a core with two radial (inner and outer) fuel zones is taken as a first example (see Fig. 4.10). It is expected that by placing fresh pebbles in the outer region of the core reduces the radial power peak near the inner reflector. The effect on the power density and k_{eff} is investigated for several recycling schemes. Each pebble first passes n times through the outer fuel region and the remaining number ($N_{tot}-n$) through the inner region. In this way the burnup level in the outer region of the core is lower than in the inner region.

Since each pebble passes the same number of times through the core and has the same velocity for all passes it follows that each pass is represented by the same number of pebbles. The inner and outer radii of the pebble bed are fixed to 1 and 1.85 m, respectively. The size (radius) of the fuel regions is determined by the number of pebble passes in each region. Fig. 4.11 shows the effect of the fuel zoning on the k_{eff} and maximum power density. In the case of a small number of passes in the outer zone, a small zone with a high fissile content is located near the outer reflector. Regions in the pebble bed of high neutron importance are located near the inner reflector and, although to a lesser extend, near the outer reflector. Placing fresh pebbles in these regions results in a high k_{eff} , and in a power peak.

By increasing the number of passes in the outer zone, the average fissile concentra-

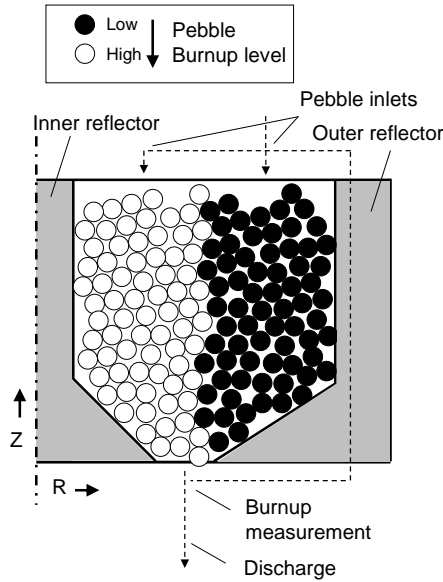


Fig. 4.10: Schematic overview of radial fuel zoning in a pebble bed reactor with an outer fuel zone of low burnup pebbles and an inner fuel zone of low burnup pebbles. The figure shows the cross sectional plane at one of the three pebble discharge tubes.

tion of the outer zone reduces. Furthermore, the boundary between inner and outer zone shifts and a larger part of the outer zone moves away from the outer reflector. The peak in the power density near the outer reflector is reduced as well as the k_{eff} . If more than seven pebble passes are used in the outer zone, the neutron flux in the outer zone is influenced increasingly by the inner reflector, which results in an increase in the k_{eff} .

The maximum power peak is not always located at the same position. For a small number of passes in the outer zone, the peak is located next to the outer reflector. With increasing number of passes in the outer zone a second peak near the inner reflector develops. Increasing the number of passes in the outer zone further, creates even a third peak, which is located at the inner radius of the outer zone. This explains the slight increase in the maximum power density going from three to four and from seven to eight number of passes in the outer zone (Fig. 4.11). In a second approach, the pebbles are recycled first in the inner region and then in the outer region. In general, this results in both a higher k_{eff} and a higher power peak than for the first approach (Fig. 4.12), since the fresh fuel is located in the region with a high neutron importance. For an increasing number of cycles in the inner region, the size of this region increases while the fissile concentration in this zone decreases. The first mentioned effect results in an increase of the k_{eff} , while the second effect decreases

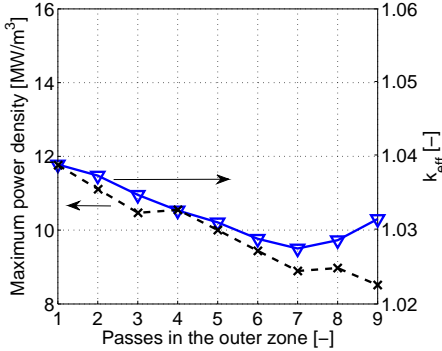


Fig. 4.11: Effect of radial fuel zoning on the k_{eff} and maximum power density for a two zone core in which an outside-inside recycling scheme is applied.

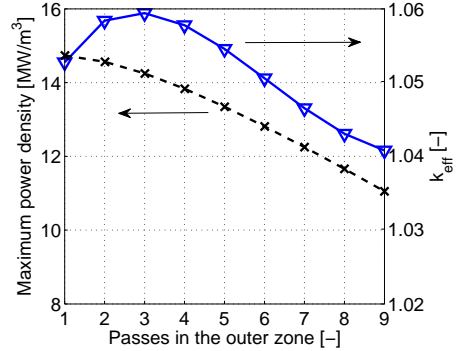


Fig. 4.12: Effect of radial fuel zoning on the k_{eff} and maximum power density for a two zone core in which an inside-outside recycling scheme is applied.

the k_{eff} . Therefore, an optimum exists for the k_{eff} when the pebbles are recycled in the inner zone three times. From the viewpoint of fuel efficiency, the inside-outside recycling scheme gives a better performance, at the expense of a high power peak near the inner reflector.

From the above it can be concluded that the maximum power density can be as low as 8.7 MW/m^3 by adopting a two zone recycling scheme. For this calculation, without temperature feedback, the resulting k_{eff} of 1.027 is lower than a core with only one zone (k_{eff} of 1.040) which has a maximum power density of 10.0 MW/m^3 .

Radial fuel zoning optimization using a heuristic method

In this section a more general approach for the pebble reloading scheme is presented in which the pebbles are allowed to pass in a any order through the different zones. For example, the pebbles can be (re-)inserted in a two zone core using following the sequence $\{1,2,2,1,2,1,2,2,1,1\}$, in which the numbers refer to the different zones.

As in the previous analysis the core is divided into n regions and in each region i the pebbles can pass k_i times, while the total number of passes N_{tot} is equal to $\sum_{i=1}^n k_i$. As before, the size of the region depends on the number of passes it contains, such that the number of pebbles is conserved.

A heuristic method based on the method of Ref. [106] was used to speed up the search for the optimal pebble reloading pattern. The search of the optimal pebble loading pattern starts with a global search in which the power profiles of several randomly chosen loading patterns H are evaluated. The loading pattern which results in the lowest power peak q is chosen as the first reference loading pattern $H_R(1)$.

An interchange optimization procedure is used to find an improved loading pattern by evaluating permutations of the reference loading pattern. Only permutations are allowed that interchange one certain loading position in the sequence with another. The logical flow structure of this local search that follows the global search is presented in Fig.4.13. In the case that one or more of the permuted patterns result in a reduction of the power peak, the best loading pattern is taken as the new reference from which a new local search is started. These local searches are repeated until no further improvement is found. Using the calculation procedure of Sec. 4.2 the loading patterns

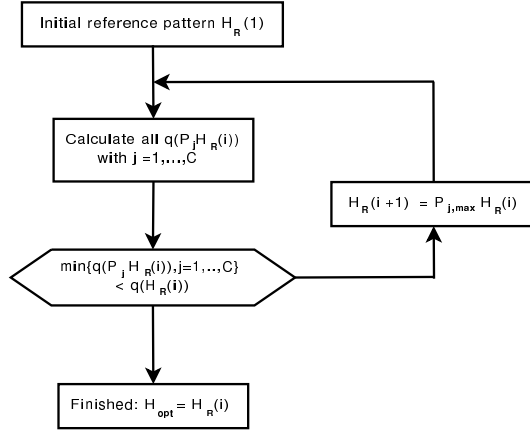


Fig. 4.13: *The logical flow structure of the search method of the optimal power profile.*

are evaluated, using a fixed evolution of the nuclide densities as a first guess. The corresponding flux and power profile are calculated with DALTON and the maximum power density, $q(P_j H_R(i))$, is derived. When the optimization procedure has found the best estimate for the optimal loading pattern, H_{opt} , the evolution of the nuclide densities is updated and the corresponding maximum power density is calculated following the calculation procedure of Fig. 4.1.

Three cases are investigated with the optimization routine, namely: no radial zoning (one zone), two radial zones and three radial zones. The average radial power profiles of the three cases are shown Fig. 4.14. It can be seen that the maximum power density reduces with increasing number of zones. For the three zone case, the radial profile is considerably flattened and the maximum power density is reduced to 8.2 MW/m^3 (Fig. 4.15). Fig. 4.14 also shows the optimal power profile which is a flat line with an average power density of 4.78 MW/m^3 . It shows that a further reduction of the maximum power density can be expected by increasing the number of zones although the size of the zones will be reduced towards the size of the pebbles.

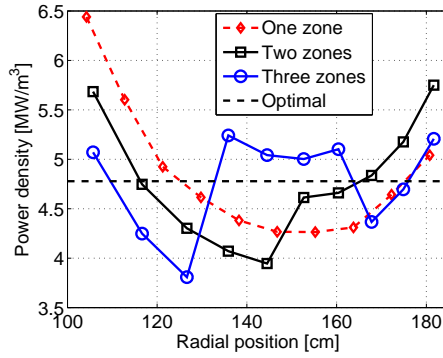


Fig. 4.14: Average radial power profile for one, two and three radial refueling zones. For the three zone core the pebbles are cycled through the three zones following the sequence: {2, 2, 1, 2, 1, 3, 2, 3, 3, 1}.

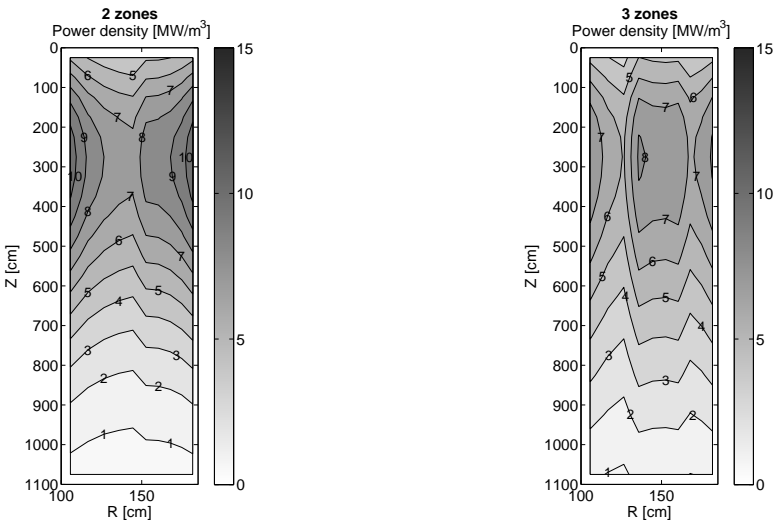


Fig. 4.15: Power profile of a two (left) and three (right) zone core, showing the flattening effect of the radial fuel zoning.

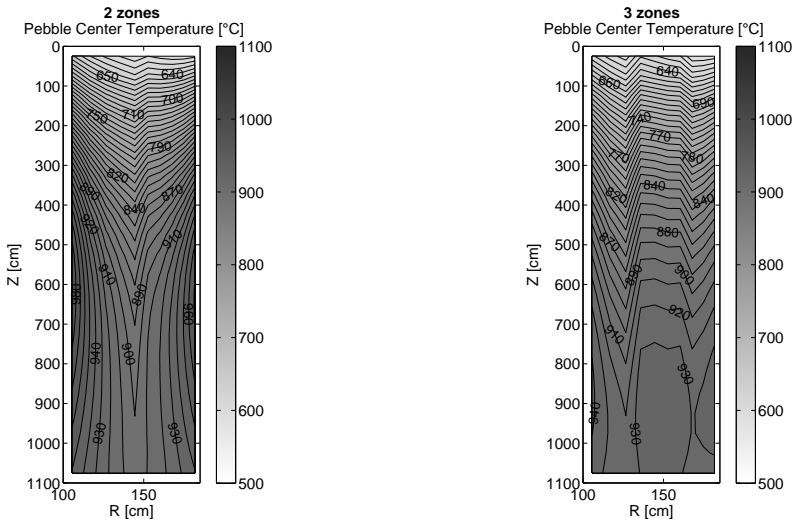


Fig. 4.16: Pebble center temperatures in cores with two (left) and three (right) radial zones, showing a reduction in the maximum temperature with increasing number of zones for normal operating conditions.

4.6 Fuel temperature of the improved design

The influence of the improved power profile on the fuel temperature during normal and a DLOFC transient have been investigated with the DALTON-THERMIX code system. The results are presented in Figs. 4.16 and 4.17, respectively.

Since the power profile is flattened for a core with three radial fuel zones, the temperature profile is also flattened (Fig. 4.16). The maximum fuel temperature is lowered with more than 30 °C and 80 °C as compared to the reference case for the two and three zone cores, respectively.

Because the maximum power density is reduced considerably for the improved design, the peak in the temperature profile that occurs in the DLOFC transient of the reference case is reduced (see Fig. 4.17). The maximum temperature occurring during the transient is reduced with approximately 300 °C.

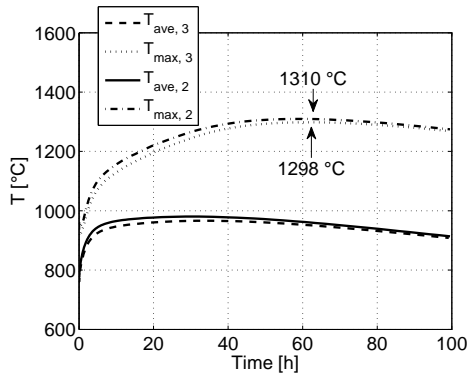


Fig. 4.17: Average (*ave*) and maximum (*max*) fuel temperatures during a DLOFC transient in cores with two and three zones.

4.7 Conclusion

The fuel loading pattern of the PBMR-400 was optimized with regard to the fuel temperature. The following conclusions are drawn:

- By adopting a multi recycling scheme for the pebbles the axial power profile is flattened and the maximum fuel temperature is reduced with increasing number of pebble cycles. Beyond six pebble passes no significant improvement is found for the maximum fuel temperature for normal operating conditions. However, an additional reduction of the maximum fuel temperature of 100 °C was found during a Depressurized Loss of Forced Cooling accident case if a total of ten pebble passes is used. Using more than ten passes is expected to result in only

a small reduction in the temperature for the transient case.

- By creating several radial fuel zones in the core in combination with multiple pebble recycling steps the radial distribution of fissile material can be influenced. For a two zone core it was found that by recycling the pebbles eight times in the outer zone and two times in the inner zone consecutively, the peak in the radial power profile reduces from 10 MW/m^3 to 8.7 MW/m^3 .
- The maximum power density can be further reduced to 8.2 MW/m^3 using three radial fuel zones. In this case the pebbles are (re)loaded following a specific sequence found with an optimization routine.
- In an improved pebble bed design with three radial fuel zones, the maximum fuel temperature during normal operation and during a DLOFC transient is reduced by $80 \text{ }^\circ\text{C}$ and $300 \text{ }^\circ\text{C}$, respectively.

5

Alternative pebble-bed concepts

In the previous chapter the fuel management of a pebble-bed reactor has been optimized without altering its geometry. In this chapter alternative reactor concepts are investigated whose dimensions (Sec. 5.1) and geometry (Sec. 5.2) are allowed to deviate from the reference design. Furthermore, the primary direction of the coolant flow in the core is altered in Sec. 5.3 in an attempt to reduce both the pressure losses over the core and the peak fuel temperatures.

5.1 The OTTO core

It is possible to derive an analytical expression for the axial power profile that will result in a flat axial fuel temperature distribution [11, 63]. The maximum temperature at the pebble center, for a pebble located at an axial position z in the core can be calculated from the helium temperature T and the power density q''' using the following equation [11]:

$$T_{max}(z) = T(z) + \frac{1}{\lambda_{tot}} q'''(z). \quad (5.1)$$

In this equation ($\frac{1}{\lambda_{tot}}$) is the thermal resistance between pebble center and helium coolant and is given in Sec. 5.3. It is assumed that the helium coolant that flows from the top to bottom of the core is the only heat transfer mechanism between the pebble surface and the final heat sink:

$$\rho c_p \varepsilon v_z \frac{dT}{dz} = q'''(z) \quad (5.2)$$

Demanding that the maximum temperature described by Eq. (5.1) is constant over the axial direction of the core results in the following equation:

$$\frac{dT}{dz} + \frac{1}{\lambda_{tot}} \frac{dq'''}{dz} = 0 \quad (5.3)$$

5. Alternative pebble-bed concepts

By combining Eq. (5.2) and Eq. (5.3) we arrive at a differential equation, which has the following solution for the axial power profile:

$$q'''(z) = Ae^{-\frac{\lambda_{tot}}{\rho c_p \epsilon v_z} z} \quad (5.4)$$

This exponential shape can be approximated by using an 'Once Through Then Out' (OTTO) fueling strategy, which results in a high peak in the power profile at the top of the reactor. This peak matches the low helium temperatures in this region of the core, while in the bottom region the high helium temperature is matched by a low power density.

It is noted that the asymmetrical power profile is in general considered to be disadvantageous during loss of flow accidents, in which the power peak results in high temperatures at the location of the peak. However, in the OTTO fueling scheme the high temperatures in the top region match the low burnup of the fuel, i.e. low concentration of gaseous fission products in the buffer layer of the TRISO. It will be shown that the stresses and corresponding failure fractions of the coatings remain low, while high fuel temperatures are encountered.

Table 5.1 presents the results for an OTTO core based on the PBMR geometry and two cores with reduced core height and power. For the 400 MW design, the tall core geometry combined with the high target burnup of the fuel, results in a power profile that deviates significantly from the one described by Eq. 5.4. The OTTO scheme therefore does not lead to a flat temperature distribution (see Sec. 4.4). Reducing the core height together with a reduction in reactor power, for a fixed average power per pebble, changes the burnup profile (Fig. 5.1) and reduces the maximum power density (Fig. 5.2) which results in a flattened maximum fuel temperature profile (Fig. 5.3).

Table 5.1: *OTTO core results.*

Item	P = 400 MW	P = 200 MW	P = 100 MW	Unit
	H _{core} = 11 m	H _{core} = 5.5 m	H _{core} = 2.75 m	
q''' _{max}	33.6	19.7	12.4	MW/m ³
T _{max} nominal	1436	1192	1100	°C
T _{max} DLOFC	2321	1544	1197	°C
σ _{t,SiC} nominal	-92.4	-85.0	-125.7	MPa
σ _{t,SiC} DLOFC	-115	-76.2	-122.9	MPa

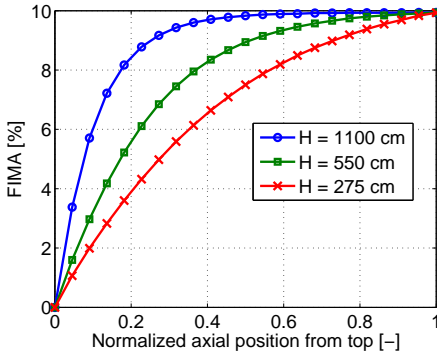


Fig. 5.1: Burnup in an OTTO fuel management scheme as a function of the axial position for three core heights.

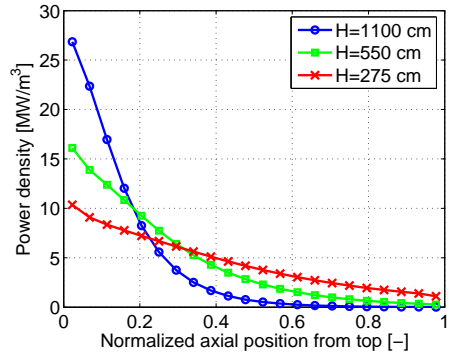


Fig. 5.2: Power profile in OTTO cores. The power profile is flattened for the cores with reduced heights ($H = 550$ and $H = 275$ cm) compared to the OTTO core with reference core height ($H = 1100$ cm).

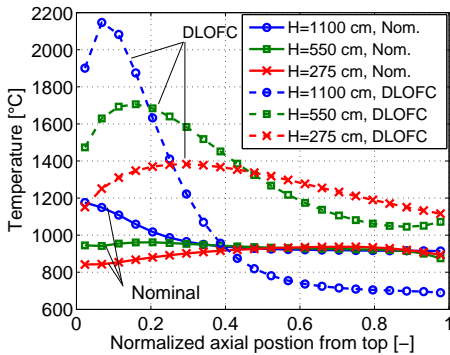


Fig. 5.3: Temperature profile in OTTO cores for both nominal and DLOFC conditions. The temperature profile is flattened for the cores with reduced heights ($H = 550$ and $H = 275$ cm) compared to the OTTO core with reference core height ($H = 1100$ cm).

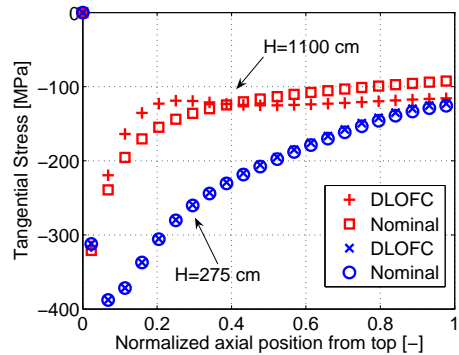


Fig. 5.4: Tangential stress in the SiC layer for both nominal and DLOFC conditions as a function of the axial position in OTTO cores with a height of 1100 and 275 cm.

A comparison of the tangential stresses in the SiC layer, calculated using the procedure of Sec. 3.2, for both nominal and DLOFC conditions has been made for the three OTTO designs (Fig. 5.4). Note that the stress profile of the core with $H = 550$ cm has a similar trend as a core with $H = 275$, but is omitted in this figure for the sake of clarity. For the DLOFC case the temperature profile changes, leading to higher temperatures in the top region and equal or lower temperatures in the bottom region of the core (Fig. 5.3). Since the burnup level and the amount of fission products in the buffer layer is low for the pebbles at the top region, the impact of the increased temperature on the stress is small. On the other hand, the temperatures in the bottom region are reduced in the case of the 1100 cm core height and only slightly increased for the two cases with reduced core heights. For these reasons, the maximum tangential stress during a DLOFC is of the same order of magnitude as the stress during nominal conditions (Table 5.1).

In the stress calculation for the DLOFC conditions it was assumed that there is no significant contribution of increased diffusion of gaseous fission products, caused by the elevated temperatures, since the time period of the transient is short compared to the diffusion process. In reality the resulting increase in internal pressure would cause the SiC tangential stress to be less compressive. Furthermore, the thermal expansion of the coating layers was not taken into account, since the coatings have similar thermal expansion coefficients [76] and the resulting stress effect is expected to be small.

It is noted that the maximum temperature in the core for the tall OTTO design exceeds by far the generally taken $1600\text{ }^{\circ}\text{C}$ while the stress in the SiC layer remains in compression, i.e. no SiC layer failure is to be expected. However, the high temperatures that were encountered in the tallest OTTO design are expected to exceed the design limits of other core components (i.e. core barrel and pressure vessel).

In the two following sections two alternative concepts are investigated in an attempt to further improve reactor performance. In the first concept a conically annular shaped pebble-bed is used to approximate the profile of Eq. 5.4. It is expected that widening the top region of the core shifts the power peak to the top. In the second concept the direction of the coolant is altered and an optimal profile for the radial direction is derived in a similar way as described above.

5.2 The conical core

A conical core is proposed in order to investigate the shift in the power peak and the corresponding effect on the fuel temperature compared to the reference design.

The conical annular pebble-bed has inner radii of 100 (bottom) and 60 cm (top) and outer radii of 170 (bottom) and 185 (top) cm. In this way the maximum outer radius of the pebble-bed is unaltered and the volume and outer surface are similar to

the annular core. It is noted that the slope of the inner and outer surfaces of the cone are limited to prevent blockage of the pebbles. Altering the shape of the pebble-bed

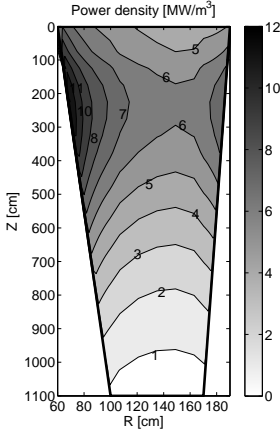


Fig. 5.5: Power profile in a conical core with six pebble passes. The location of the maximum power density has moved toward the top compared to the reference design.

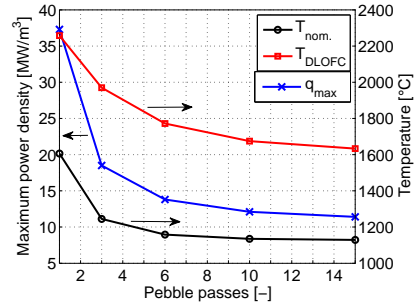


Fig. 5.6: Temperatures for nominal and DLOFC conditions and the maximum power density at nominal conditions for a conical core design as a function of the number of pebble passes.

from an annulus to a conical annulus has several effects on reactor performance. The axial velocity of the pebbles and the helium coolant are linearly dependent on the surface area perpendicular to the pebble flow. With respect to the fuel depletion the conical shape results in a larger residence time of the pebbles and a larger burnup gradient in the top region than in the bottom region of the core. Furthermore, the lower coolant velocity in the top region results in lower local pressure drop and heat transfer compared to the bottom region.

Fig. 5.5 shows the resulting power profile of a conical core using six pebble passes. It can be seen that the location (from ~ 300 to 250 cm z coordinate) and the magnitude (from 10.0 to 12.8 MW/m³) of the power peak have changed compared to the reference case, shown in Fig. 4.3.

The corresponding fuel temperatures during normal and DLOFC conditions are calculated as a function of the number of pebble passes (Fig. 5.6). Although the position of the peak is improved for some of the cases, its increased magnitude results in elevated fuel temperatures for both normal and DLOFC conditions.

It is established that by altering the shape of the pebble-bed a significant modification of the power profile can be realized. However, no significant improvements have been found for the particular shape proposed above and so the conical core is

abandoned for the rest of this thesis.

5.3 The radially cooled core

In Chap. 2 it was found that the pressure drop in the PBMR design is $\Delta p \approx 2.8$ bar. To compensate for this pressure loss a total circulator power which is more than 7 % of the net power generated is required for this design.

By altering the primary direction of the coolant flow from the axial to the radial direction, the pressure drop can be reduced tremendously [107]. In that case the coolant flows from the outer reflector through the pebble bed and finally to flow paths in the inner reflector, through which the coolant exits the reactor. The cooling flow paths in the reactor for radial and axial cooling are shown in Fig. 5.7. As a

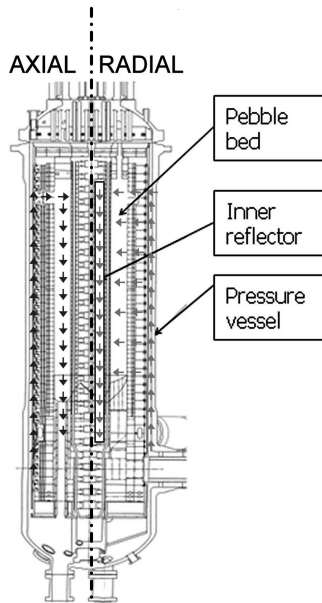


Fig. 5.7: Flow paths in an axially (left) and radially (right) cooled pebble bed reactor.

consequence of the modified cooling, the fuel temperatures are elevated due to the reduced heat transfer of the coolant caused by a lower fluid velocity. However, the low pressure drop in the radially cooled reactor allows for a reduction in the pebble size that reduces the fuel temperature.

Furthermore, it is shown that the radial power profile can be improved by recycling the pebbles several times in three separated radial fuel zones [108]. This reduces the fuel temperature significantly. A theoretical optimum for the radial profile can be

derived analytically and can be approximated by adopting several radial fuel zones.

In this section the effects of pebble size reduction on the pressure drop and the maximum fuel temperature are quantified. First, an analytical expression is derived to calculate the pressure drop and fuel temperature in a radially cooled reactor. In a second step a two-dimensional numerical model is used to calculate the combined effect of pebble size reduction and adoption of radial fuel zones for both normal and LOFC conditions.

Optimization of the pebble size

In order to quantify the effect of the pebble diameter size on the pressure drop and the fuel temperature a simple analytical procedure is used first.

The maximum temperature at the pebble center, for a pebble located at a radial position r in the core can be calculated from the helium temperature T and the power density q''' with the following equation [11]:

$$T_{max}(r) = T(r) + \frac{1}{\lambda_{tot}} q'''(r). \quad (5.5)$$

In the above equation $\left(\frac{1}{\lambda_{tot}}\right)$ is the total thermal resistance (multiplied with the volume) between helium coolant and pebble center. An equation for the total thermal resistance can be derived from a heat balance for a single pebble [11], assuming that heat is generated in the fuel region of the pebble only:

$$\frac{1}{\lambda_{tot}} = \frac{1}{(1-\varepsilon)} \left[\frac{R_{peb}^3}{2kR_{fuel}} - \frac{R_{peb}^2}{3k} + \frac{R_{peb}}{3h} \right]. \quad (5.6)$$

The heat transfer coefficient h between the helium coolant and the pebble surface can be calculated with [11]:

$$h = \frac{k_{he}}{2R_{peb}} \left(1.27 \frac{Pr^{0.33}}{\varepsilon^{1.18}} Re^{0.36} + 0.033 \frac{Pr^{0.5}}{\varepsilon^{1.07}} Re^{0.86} \right). \quad (5.7)$$

The pressure difference by friction in a pebble bed depends on the Reynolds number and is derived from the following relation [11]:

$$\nabla p = -\psi \frac{1-\varepsilon}{\varepsilon} \frac{1}{2R_{peb}} \frac{\rho}{2} |\mathbf{v}| \mathbf{v} \quad (5.8)$$

$$\psi = \frac{320}{(Re/(1-\varepsilon))} + \frac{6}{(Re/(1-\varepsilon))^{1/10}}. \quad (5.9)$$

and the Reynolds number is defined as:

$$Re = \frac{\rho 2R_{peb} \varepsilon |\mathbf{v}|}{\eta}. \quad (5.10)$$

5. Alternative pebble-bed concepts

For the axially cooled core a straightforward integration of Eq. (5.8) over the core height results in a relation for the core pressure drop. For the radially cooled core the velocity depends on the radial position. From the continuity equation,

$$\frac{1}{r} \frac{\partial(\varepsilon r v_r)}{\partial r} = 0, \quad (5.11)$$

it follows that

$$v_r(r) = \frac{r_o v_r(r_o)}{r}, \quad (5.12)$$

by assuming that the helium flows inward with a certain velocity at the outer radius. It is assumed that the porosity profile of the pebble bed is flat.

The momentum equation in cylindrical coordinates for the radial direction is as follows:

$$\varepsilon \rho v_r \frac{\partial v_r}{\partial r} = -\varepsilon \frac{\partial p}{\partial r} + \varepsilon \psi \frac{1-\varepsilon}{\varepsilon} \frac{1}{2R_{peb}} \frac{\rho}{2} v_r^2 \quad (5.13)$$

Note that the constant porosity drops out of the above equation. Combining Eq. (5.13) with Eqs. (5.8) through (5.10) and integrating over the radial direction results in the following expression for the pressure difference:

$$\begin{aligned} \Delta p = & (r_o v_r(r_o))^2 \left[\frac{\rho}{2} (r_o^{-2} - r_i^{-2}) \right] \\ & + (r_o v_r(r_o))^2 \left[A \cdot \ln(r_o/r_i) - B \cdot (r_o^{-9/10} - r_i^{-9/10}) \right], \end{aligned} \quad (5.14)$$

in which A and B are defined as follows:

$$A = \frac{160(1-\varepsilon)^2 \eta}{r_o v_r(r_o) \varepsilon^2 d^2} \quad B = \frac{10}{3} \frac{\rho(1-\varepsilon)}{\varepsilon d} \left(\frac{1-\varepsilon}{r_o v_r(r_o) \varepsilon \rho d} \right)^{1/10} \quad (5.15)$$

Note that the first term in Eq. (5.14) represents the pressure difference by convective flow, which is small compared to the pressure loss by friction for all cases considered.

The pressure and temperature have been calculated for various pebble diameters for both an axially and a radially cooled pebble bed based on the geometry of the PBMR-400 design. This design has a core height of 1100 cm, an inner reflector with a radius of 100 cm and a pebble bed with an outer radius of 185 cm. The standard pebble has a radius of 3 cm with a fuel-free (graphite) outer zone of 0.5 cm thickness. In the calculation for smaller pebble sizes, the fuel-free zone of 0.5 cm is kept, while the fuel zone size is varied. A case with pebbles of 0.5 cm radius without graphite shell is also considered.

The maximum temperature and pressure drop as a function of the pebble diameter for both radially and axially cooled pebble bed reactors are shown in Fig. 5.8. When radial cooling of the bed is adopted instead of axial cooling, both the coolant velocity

and the length of the flow path through the core are reduced, which results in a large reduction of the pressure drop over the core. The reduction in coolant velocity causes a reduction in the heat transfer between coolant and pebble surface and therefore the pebble center temperature increases (Fig. 5.8). For a given pebble diameter

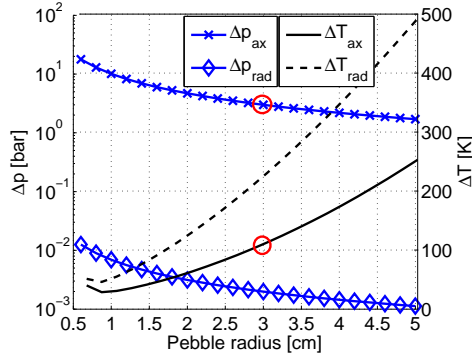


Fig. 5.8: Pressure drop (Δp) over the core and temperature difference (ΔT) between coolant and pebble center temperature for a radially (rad) and axially (ax) cooled pebble bed, as a function of the pebble radius. The circle shows the operating conditions of the PBMR-400 design.

the temperature difference is higher for the radially cooled bed than for the axially cooled one. Reducing the pebble diameter, in an attempt to reduce this temperature difference, leads to a high pressure drop for the axially cooled pebble bed. In this case the pumping power is several percent of the power generated. For the radially cooled pebble bed however, the pressure drop remains small, even for very small pebble diameters. Therefore, by combining radial cooling with a reduced pebble size, a low pressure drop together with lower fuel temperatures, compared to an axially cooled core for a fixed helium outlet temperature, are theoretically achievable. For example, Fig. 5.8 shows that compared to the current PBMR-400 design the same temperature difference can be achieved for a 1.8 cm pebble radius with a pressure drop a factor 1000 lower (3 mbar).

Derivation of the optimal power profile in a radially cooled reactor

Besides reducing the pebble diameter, the power profile can also be optimized in order to reduce the fuel temperatures. An analytical approach is used to derive the optimal radial power profile. In an attempt to realize this optimal profile the (radial) starting positions of the pebbles are altered. A more complex numerical calculation is used to determine the resulting power profile for several pebble loading patterns.

The differential energy equation in the radial direction for the helium coolant,

assuming that all the power generated is directly transferred to the helium coolant, is [109]:

$$\rho c_p \varepsilon v_r \frac{dT}{dr} = q'''(r) \quad (5.16)$$

Demanding that the maximum temperature described by Eq. (5.5) is constant over the radial direction of the core results in the following equation:

$$\frac{\partial T}{\partial r} + \frac{1}{\lambda_{tot}} \frac{\partial q'''}{\partial r} = 0 \quad (5.17)$$

By combining Eq. (5.16) with Eq. (5.17) and the previous result (Eq. (5.12)) for v_r we arrive at the following differential equation for the radial power distribution:

$$\frac{\partial q'''}{\partial r} + \left(\frac{\lambda_{tot}}{\rho c_p v_r(r_o) r_o \varepsilon} \right) r q'''(r) = 0 \quad (5.18)$$

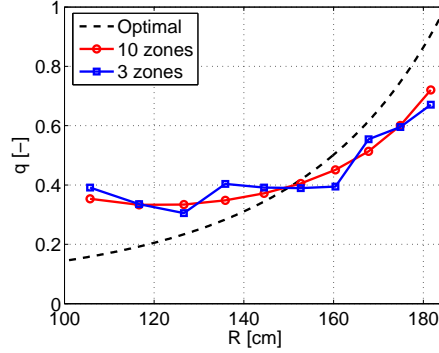
Solving Eq. (5.18) results in the following optimal power profile:

$$q'''(r) = A e^{\left(-\frac{1}{2} \left(\frac{\lambda_{tot}}{\rho c_p v_r(r_o) r_o \varepsilon} \right) r^2 \right)} \quad (5.19)$$

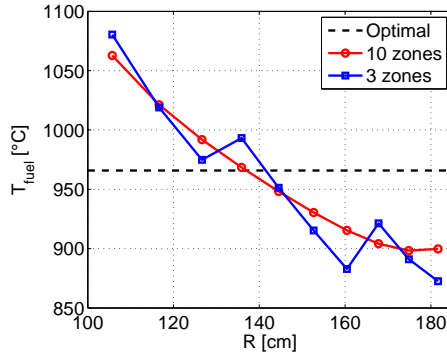
in this equation A is a coefficient to be determined from the total reactor power. The resulting optimal power profile for a standard pebble size ($R_{peb} = 3.0$ cm) is presented in Fig. 5.9(a) and the resulting flat temperature profile in Fig. 5.9(b). A large difference exists between the power level at the inner surface and outer surface of the pebble bed. It follows from Eq. (5.19) that the profile depends on the total heat transfer (Eq. (5.6)) and is more flattened for large pebble size. In order to approximate the optimal power profile in practice the radial distribution of the fuel has to be optimized.

Effect of radial fuel zoning on the power profile and fuel temperature

The optimal power profile is approximated by dividing the core into several radial fuel zones. A multi-pass recycling scheme is adopted in which pebbles with a low burnup are placed in the outer core region and high burnup pebbles in the inner region. In the case that the total number of pebble passes through the core is larger than the number of fuel regions, a fuel zone can contain pebbles having different burnup levels. Fig. 5.10 shows a pebble recycling scheme for a three zone core in which pebbles pass through the core ten times. The first pass of the pebbles is in the outer fuel zone and each consecutive pass is either in the same zone or in a zone closer to the inner reflector. Because fresh fuel is now present on the outside of the core and depleted fuel on the inside, the power level has increased on the outside and decreased on the inside. The power profile for the proposed loading pattern is



(a) Radial power profiles



(b) Radial temperature profiles

Fig. 5.9: The optimal (normalized) power profile yielding a radially flat temperature profile ($R_{peb}=3.0$ cm) determined by an analytical derivation and two power profiles obtained numerically by applying three and ten radial fuel zones (a). The corresponding temperature profiles are shown in (b).

calculated with the numerical procedure described in Sec. 4.2. The resulting power profiles for three and ten radial zones are presented in Fig. 5.11. In the case that ten radial zones are used, each zone represents one pebble pass, while for three radial zones, the pebbles pass through the inner and outer zone three times and four times through the middle zone (Fig. 5.10). The profile for the ten zone case shows a smooth surface, while the three zone case exhibits two jumps at positions of the fuel region interfaces. In Fig. 5.9(a) the radially averaged power profiles of the two numerical solutions are compared with the optimal radial profile. The corresponding 1D temperature profiles, calculated with Eq.(5.5), are presented in Fig. 5.9(b). It can

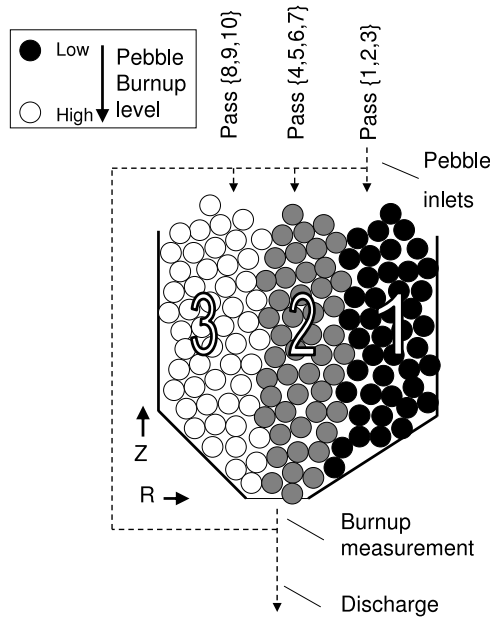


Fig. 5.10: Pebble loading pattern for a core with three radial fuel zones and ten pebble passes, showing how the pebbles are recycled from the outside to the inside.

be seen that the discontinuities vanish in the power profile when ten zones, instead of three, are adopted. However, the profile does not significantly improve with respect to the difference with the optimal profile.

The effect of the power profile, calculated with THERMIX [48], on the 2D pebble center temperature profile can be seen in Figs. 5.12 and 5.13. In the case of three radial fuel zones and a pebble radius of 3 cm, three peaks in the temperature profile can be identified that correspond with the peaks in the power profile. If the number of fuel zones is increased to ten and the pebble radius reduced to 0.5 cm only one peak in the temperature profile remains, which is located next to the inner reflector. The difference in the temperature between the outside and inside of the core is larger for the smaller pebble size, since the deviation from the optimal profile (see Eq. (5.19)) is larger for this pebble size.

5.4 Optimized radially cooled core design

The combined effect of pebble size reduction and the fuel management scheme on the pressure loss and maximum fuel temperature has been investigated with a two-dimensional reactor model in the thermal-hydraulics code THERMIX [48] for normal

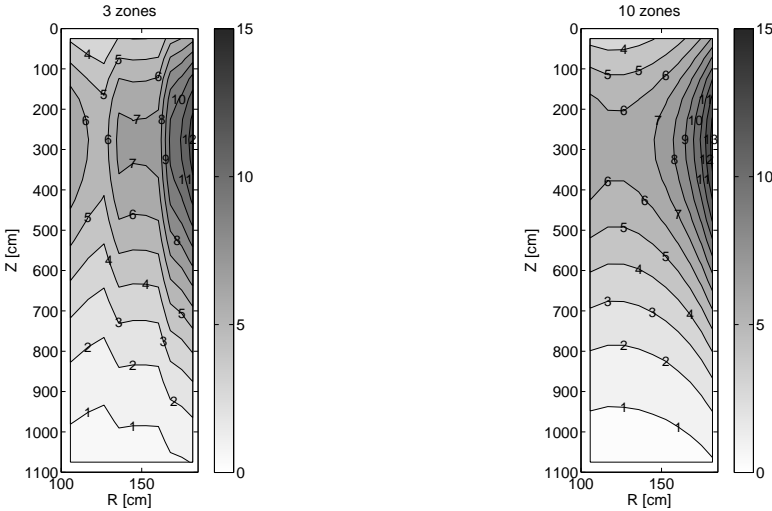


Fig. 5.11: Power profiles [MW/m^3] for both three (left) and ten (right) radial fuel zones.

and LOFC conditions.

Normal operating conditions

For the normal operating conditions, three different power profiles are used in the analysis. The first case represents a core configuration without radial fuel zoning (1 zone), while in the two other cases, the power profiles calculated in Sec.5.3 for 3 and 10 radial zones are used. In all cases a total of ten pebble passes is used and the pebble radius is varied between 0.5 and 3.0 cm.

The maximum fuel temperature for the normal operating conditions as a function of the pebble radius for several pebble radii is presented in Fig. 5.14. Both the use of more fuel zones and a reduction of the pebble size result in considerably lower fuel temperatures.

The average pressure drop over the pebble bed calculated with THERMIX for a 3.0 cm pebble radius was found to be $2.1 \cdot 10^{-3}$ bar, which compares well with the $2.0 \cdot 10^{-3}$ bar that resulted from the analytical calculation. The THERMIX calculation shows that less than 2 % of the total pressure drop occurs in the pebble bed for this case, while the main part is caused by the pressure drop at the slits and flow paths in the inner reflector. The total pressure drop in the core as a function of the pebble radius is shown in Fig. 5.15. Although the pressure drop increases with a reduction of the pebble size it remains more than an order of magnitude smaller compared to

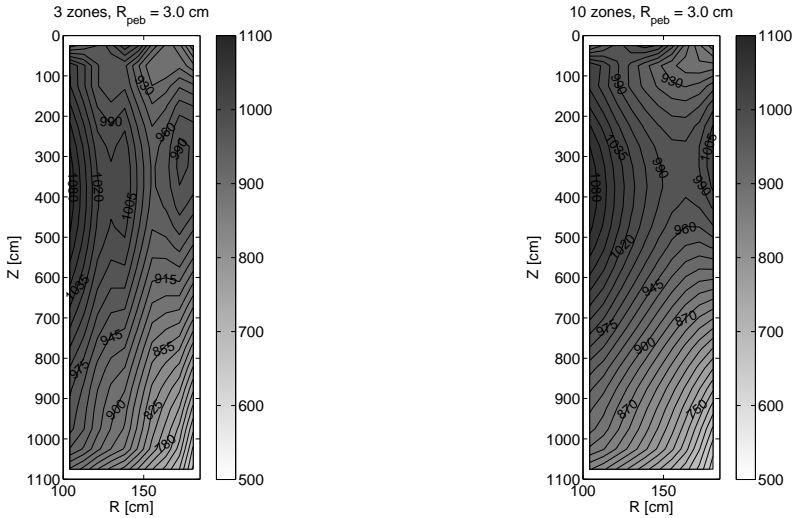


Fig. 5.12: Fuel temperature profiles [$^{\circ}\text{C}$] in a core with three (left) and ten (right) radial fuel zones for a pebble radius of 3.0 cm.

the axially cooled pebble bed for all cases.

LOFC conditions

The maximum and average fuel temperatures are calculated for both a Pressurized and Depressurized Loss of Forced Cooling (DLOFC and PLOFC) accident for a core with ten fuel zones and $R_{peg} = 0.5$ cm.

It is assumed that a reactor SCRAM is performed at the beginning of the transients and that the outer surface of the pressure vessel is cooled effectively by the decay heat removal system, which is simulated by a fixed temperature and heat transfer coefficient. Adiabatic boundary conditions are assumed for the top and bottom of the model. During the first 13 seconds of the transients the system pressure is reduced from 90 to 1 bar in the depressurized case and to 60 bar in the pressurized case. In both cases the mass flow is reduced to zero in the same time period.

In Fig. 5.16 the results for maximum and average temperature during the DLOFC and PLOFC transients are shown. The initial temperature profile for the transients can be seen in Fig. 5.13 and the initial maximum and average temperatures in Fig. 5.16 are 939°C and 753°C respectively. In the first few hundred seconds of the transients the maximum fuel temperature reduces quickly since the fission power reduces quickly and the total reactor power consists only of the decay heat. In the following hours, the maximum and average temperature of the pebble bed rise for both the DLOFC

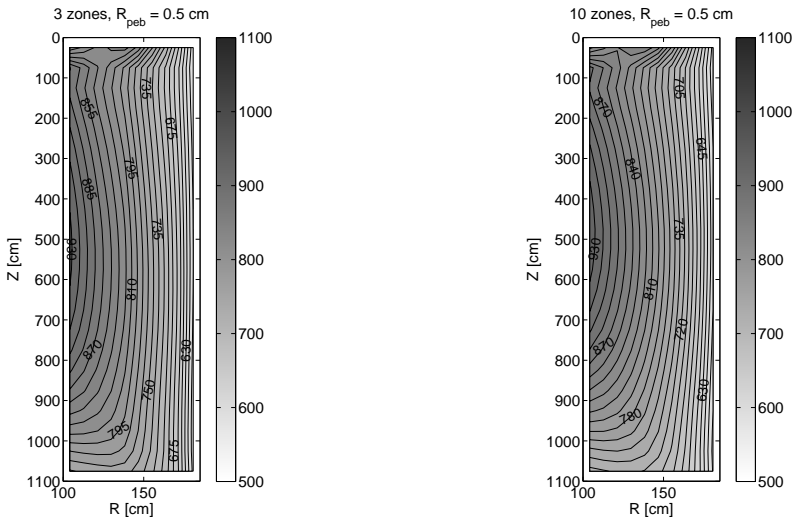


Fig. 5.13: Fuel temperature profiles [$^{\circ}\text{C}$] in a core with three (left) and ten (right) radial fuel zones for a pebble radius of 0.5 cm.

and PLOFC cases. The natural circulation in the PLOFC case distributes the heat over the entire core and to the inner reflector. This heat transfer mechanism is absent in the DLOFC case and since the heat is mostly generated in the outer region of the core (see Fig. 5.9(a)), the highest temperature is located in this region, while for the PLOFC case the highest temperature occurs at the inner region of the core. The heat of the reactor is removed through conduction in the outer reflector and finally through convection and radiation on the outside of the reactor pressure vessel. Therefore, the heat is more effectively removed in the DLOFC case. The temperature profiles for both cases at the time point of the maximum fuel temperature is presented in Fig. 5.17 to illustrate the above described effects.

The maximum fuel temperature for the two cases is significantly below 1600°C , which is generally taken as the design limit. Since the power during the transients is determined by the decay heat, which is small compared to the fission power during normal operation, the difference in temperature between surface and center of the pebble is small. Therefore the size of the pebbles is of less importance in the determination of the maximum fuel temperature during the transients.

5.5 Conclusion

Three alternative pebble-bed core concepts have been investigated and the following is concluded:

5. Alternative pebble-bed concepts

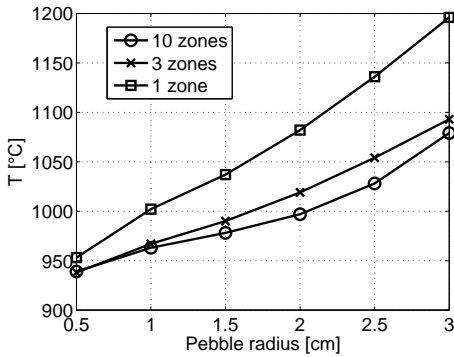


Fig. 5.14: Effect of pebble size on the maximum fuel temperature for a radially cooled reactor calculated with THERMIX for a core with 1, 3 or 10 radial fuel zones.

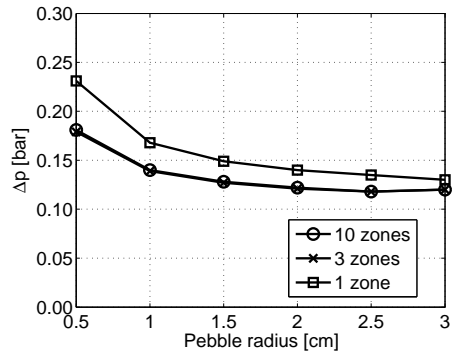


Fig. 5.15: Effect of pebble size on the pressure drop in the core (pebble bed and reflector flow paths) calculated with THERMIX for a core with 1, 3 or 10 radial fuel zones.

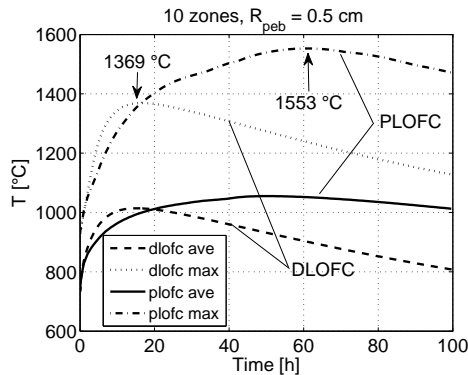


Fig. 5.16: Maximum (max) and average (ave) fuel temperatures during a Pressurized (plofc) and Depressurized Loss Of Cooling (dlofc) situation for a 10 zone core with $R_{peb} = 0.5$ cm .

- Using an OTTO fueling scheme in the reference core design, in an attempt to approximate the optimal power profile resulting in a flat fuel temperature profile, elevates the maximum fuel temperature during DLOFC conditions, while the maximum tangential SiC stress is comparable to the maximum stress at nominal conditions.
- The peak of the power profile in a conically shaped pebble-bed version of the PBMR is located closer to the optimal position, but does not yield an improved temperature distribution.
- By altering the coolant flow from axial to radial direction, the pressure drop in the pebble bed can be reduced from 2.8 bar to 0.002 bar for a standard pebble

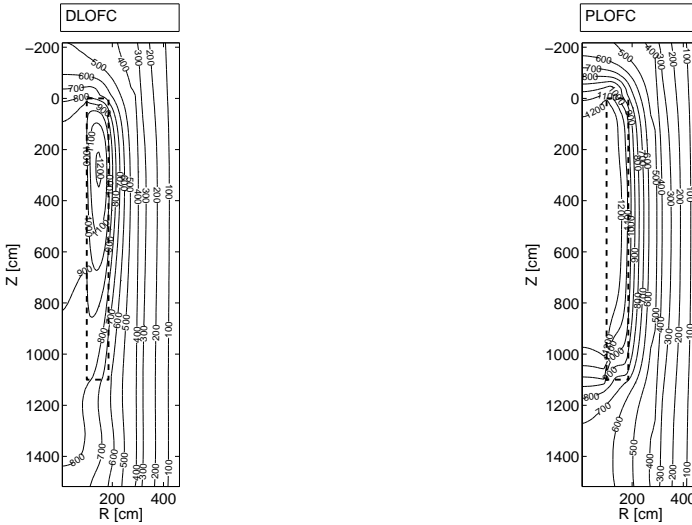


Fig. 5.17: Temperature profiles [°C] during DLOFC (left) and PLOFC (right) transients at the time of the maximum fuel temperature.

size ($R_{peb} = 3.0$ cm). The core average pebble center temperature increases with 100 °C. By reducing the pebble size and altering the (re)fueling scheme of the reactor this temperature can be reduced to 50 °C below the reference temperature, while maintaining the low pressure drop. This would result in a reduction of the pumping power with several percent of the generator power.

- By recycling the pebbles from the outside of the core to the inside the analytically derived optimal temperature profile can be approximated by adopting three or more radial fuel zones. For a standard pebble the improved power profile results in a decrease of the maximum fuel temperature with 125 °C.
- The optimized power profile is also advantageous during LOFC accidents since the peak is located at the outer zone of the pebble bed and the decay heat is removed more easily to the environment. In both PLOFC and DLOFC transient cases, the maximum fuel temperature remains below the design limit of 1600 °C and would allow for an increase in reactor power (helium outlet temperature). In the PLOFC transient the natural circulation of the helium between pebble bed and flow paths in the inner reflector causes higher temperatures in the pebble bed after several hours compared to the DLOFC transient.
- In contrast with the large pressure drop over the pebble bed in an axially cooled design, the total pressure drop in a radially cooled design is determined by losses in the coolant flow paths in the inner and outer reflector.

6

Conclusions and discussion

Increasing the operating temperature of a High Temperature Pebble-Bed Reactor is attractive with regard to its thermodynamic efficiency. Furthermore, high temperature process heat is a requirement for cost-effective production of hydrogen. In this case the reactor is coupled to a chemical process for hydrogen production, i.e. high temperature electrolysis or a thermo-chemical water splitting process.

The main objectives of this thesis are to quantify the increase of the fuel temperature for the contemplated operating conditions and its consequence for the fuel integrity. In a second step, design improvements are sought in the optimization of the fuel management and in modifications of the reference core design in order to generate safety margins that allow for a temperature increase.

6.1 Conclusions

The main conclusion of the thesis is that increasing the operating temperature of a pebble-bed reactor is possible without compromising its safety. In order to maintain safety margins or allow for a further increase (above 1000 °C helium outlet temperature) it is however desirable to modify the fuel management or the core design.

- This thesis shows that during DLOFC incidents the fuel temperature in pebble-bed reactor with a low power density is close to its nominal value. From coupled neutronic and thermal-hydraulic calculations it was found that at power densities at 0.7 MW/m³ and 2.6 MW/m³ for the HTR-10 and AVR reactors, respectively, the maximum fuel temperature is within 100 °C of the nominal maximum fuel temperature. For the 400 MW_{th} PBMR reactor design with an average power density of 4.6 MW/m³ and a maximum power density of 10.6 MW/m³, a significant increase in the core maximum fuel temperature up to 1650 °C is encountered during a DLOFC transient compared to a nominal value of 1000 °C.

- An analysis of the stresses in the coatings of the TRISO fuel particles in the PBMR design shows that there is a significant margin in the tangential stress of the SiC coating layer during nominal conditions. For an increased helium outlet temperature, up to 1075 °C, the analysis shows that the SiC layer remains in compression. No failure due to pressure build up in the particles is therefore to be expected during nominal conditions, since the SiC layer is only expected to fail under a high tensile stress. Furthermore, it was found that the stress analysis models that ignore the presence of the graphite matrix surrounding the particles are conservative, since the surrounding graphite is expected to exert an additional compressive stress on the particle coatings. Taking this into account results in an increase of the compressive tangential SiC stress from -100 to -150 MPa for particles having a target burnup level of 95 MWd/kg U.
- By adopting multi pass fuel management for the pebbles the axial power profile is flattened and the maximum fuel temperature is reduced with increasing the total number of pebble passes. Beyond six pebble passes, which is the reference case, no significant improvement is found for the maximum fuel temperature at nominal conditions. However, an additional reduction of the maximum fuel temperature of 100 °C was found during a DLOFC case if a total of ten pebble passes is used. Using more than ten passes is expected to result in only a small reduction in the temperature for this transient case.
- By creating several radial fuel zones in the core in combination with multiple pebble recycling steps the radial distribution of fissile material can be influenced. For a core with two radial fuel zones recycling the pebbles eight times in the outer zone and two times in the inner zone consecutively, the peak in the radial power profile reduces from 10 MW/m³ to 8.7 MW/m³. This peak can be reduced to 8.2 MW/m³ if three radial fuel zones are used. In that case the pebbles are (re)loaded following a specific zone sequence. For this optimal case the maximum fuel temperature during normal operation and during a DLOFC transient is reduced by 80 °C and 300 °C, respectively.
- A Once-Through-Then-Out (OTTO) fueling scheme can be used to approximate the optimal power profile yielding an axially flat fuel temperature profile. The resulting high peak in the power profile which causes high temperatures in a small region of the core during a DLOFC transient are not expected to lead to a high particle failure probability, since the particles in that region have a low fuel burnup level. Therefore, the resulting maximum stress in the particle coatings during the DLOFC case is comparable to the stress at nominal conditions.
- By altering the coolant flow from axial to radial direction, the pressure drop in the pebble bed can be reduced theoretically from 2.8 bar to 0.002 bar for a standard pebble size ($R_{peb} = 3.0$ cm). This results in a reduction of the pumping power leading to an increase of the plant efficiency with more than 5 %.

The reduced heat transfer from pebble surface to coolant increases the core av-

erage pebble center temperature with 100 °C. Fortunately, the low pressure drop allows for a reduction of the pebble size that leads to a reduction of the thermal resistance between the pebble center and the helium coolant. This thesis shows that by a reduction in the pebble size to $R_{peb} = 0.5$ cm the temperature can be reduced from 1200 °C to 950 °C in combination with a low pressure drop of $\Delta p < 0.25$ bar. The maximum fuel temperature can also be reduced in this radial cooling configuration by optimizing the pebble (re)fueling scheme, which reduces the nominal maximum fuel temperature with 120 °C to 1080 °C for a standard pebble size. The optimized power profile is also advantageous during LOFC accidents since the power peak is located at the outer zone of the pebble bed and the decay heat is removed more easily to the environment.

6.2 Discussion and recommendations

From Chap. 2 it was found that small bypass and natural convection flows can be of major importance for transient behavior of HTRs. A further investigation and measurement of these flows is therefore recommended. The limiting side of the coupled neutronics and thermal-hydraulics code system is the 2D THERMIX code and more specifically, the determination of the flow velocity field in large helium cavities. The existence of a 3D thermal-hydraulics code that is able to cope with these flows, without the computational costs of a detailed CFD code, could improve the present code system.

For the determination of the equilibrium core composition a radially uniform pebble velocity field has been used. It is known that, depending on the shape and location of the pebble discharge tube, the radial pebble velocity distribution is not flat in general. The calculation method in the depletion analysis could therefore be improved by taking this flow profile into account. Furthermore, the pebble velocity profile could be optimized, since it influences the core burnup distribution, by modifying the bottom section and the pebble discharge region. One could take this one step further by also modifying the shape of the entire core as was done for the conical core design. An optimal shape, leading to a flat power profile, could then be derived.

Since the transition of the initial to the equilibrium core can take several years, an investigation of the core behavior during this transition and a possible reduction of the transition time are of interest.

The stress analysis code PASTA code be further improved by adding other failure mechanisms, such as the shrinkage induced cracking of the PyC layers, due to tensile stresses in the beginning of the irradiation, which can lead to possible failure of the SiC layer [99]. Furthermore, the availability of experimental data of the creep coefficient and shrinkage behavior of the PyC and graphite matrix at the appropriate dose rate and temperature range would also lead to a significant improvement of the fuel performance model. Data of other coating materials, such as ZrC, that could

improve particle performance is desirable. Preliminary tests of ZrC coatings show promising results for high temperatures, i.e. no significant coating failures up to 2400 °C [110, 111]. It is noted that with fuel temperatures at this order of magnitude, the temperature of other reactor components are likely to be above design limits and should be examined.

Recent developments in the core design of a liquid salt cooled pebble-bed reactor [112] show promising results of a core concept having a nominal power of 900 MW_{th} having a power density up to 30 MW/m³ with an efficiency of 46 % at a coolant outlet temperature of 700 °C. This concept uses so-called Pebble Channel Assemblies (PCAs) which guide the pebbles in tubes cooled by liquid salt. Thereby, the graphite to salt volume ratio can be adjusted allowing for more design freedom.

A

Point kinetic equations and HTR-10 reactivity coefficients

A.1 Neutron point kinetic equations

The point kinetic equations Eqs. (A.1),(A.2) are used in Section 2.3 of this paper to the model the neutronic behavior of the HTR-10 reactor [57].

$$\frac{dP_p}{dt} = \frac{\rho(t) - \beta}{\Lambda} P_p(t) + \sum_{i=1}^6 \lambda_i C_i(t) \quad (\text{A.1})$$

$$\frac{dC_k}{dt} = \frac{\beta_k}{\Lambda} P_p(t) - \lambda_k C_k(t) \quad k = 1, \dots, 6 \quad (\text{A.2})$$

It is assumed that change in reactivity is caused by temperature feedback $\Delta\rho_T$ (fuel, moderator or reflector) or by reactivity insertion $\Delta\rho_{rod}$ by control rod movement:

$$\rho(t) = \Delta\rho_T(t) + \Delta\rho_{rod}(t) \quad (\text{A.3})$$

To calculate the total reactor power P_t , the prompt power P_p is augmented with the decay heat P_d using the following equations:

$$P_t = P_p(t) + \sum_{j=1}^{23} P_{d_j}(t) \quad (\text{A.4})$$

$$\frac{dP_{d_j}}{dt} = -\lambda_j P_{d_j}(t) + \gamma_j P_p(t) \quad j = 1, \dots, 23 \quad (\text{A.5})$$

The coefficients for the precursors are taken from [57] and the parameters for the decay heat are adopted from [113], both assuming pure ^{235}U .

A.2 Applicability of point kinetics

According to reference [114] point kinetics can be applied without introducing large errors if the average neutron chain fission length is comparable to, or larger than, the size of the reactor. In that case a perturbation in one area of the reactor is felt throughout the core and the core is said to be tightly coupled. The average neutron chain fission length $\langle l^2 \rangle^{\frac{1}{2}}$ depends on the migration length M , the inserted reactivity ρ and the delayed neutron fraction β as follows:

$$\langle l^2 \rangle^{\frac{1}{2}} = \sqrt{\frac{6}{\beta - \rho}} \cdot M \quad (\text{A.6})$$

From the cross section generation procedure that is described in Sec. 2.1 it follows that $M \approx 80$ cm and $\beta = 6.8 \cdot 10^{-3}$ for the HTR-10. Using these values in Eq. A.6 it follows that the average neutron chain fission length is more than 25 meter for small perturbations, which is larger than the size of the HTR-10 reactor.

A.3 Reactivity coefficients of the HTR-10

The temperature reactivity coefficients for the HTR-10 benchmark calculation are generated using the procedure described in Sec. 2.1. The effect of a variation in the temperature in several zones in the reactor on the k_{eff} have been calculated. These temperature zones are:

- TRISO: The TRISO particles in the fuel zone of the pebble
- Fuel: The fuel zone of the pebble (TRISO's and graphite matrix)
- Moderator: The moderator surrounding the pebbles (pebble shell and dummy balls)
- Reflector: The graphite reflector surrounding the pebble bed
- Reactor: The entire reactor (this includes all temperature zones above). The reference temperatures above are varied with the same temperature step.

The reference operating temperatures were: $T_{fuel} = T_{TRISO} = 1000$ K, $T_{mod} = 950$ K and $T_{refl} = 750$ K. The results of the calculation for eigenvalues and corresponding average reactivity coefficients ($\bar{\rho}$) are presented in Table A.1.

Table A.1: Results of eigenvalue calculations and reactivity coefficients of the HTR-10

ΔT	Fuel	Moderator	Reflector	Reactor	TRISO
-200	1.01306	1.01551	0.98816	1.02127	
-100	1.00661	1.00785	0.99644	1.01065	1.00214
+100	0.99460	0.99329	1.00349	0.9908	0.99895
+200	0.98891	0.98613	1.00592	0.98143	
$\bar{\rho}$ [pcm·K ⁻¹]	-6.03	-7.33	4.13	-9.95	-1.53

B

Description of the DALTON and THERMIX codes

B.1 The neutronics code DALTON

The DALTON code can solve the 3D multigroup diffusion equations on structured grids (xyz or $rz\theta$ coordinates). The code's capabilities include both the fundamental and higher lambda modes and time-eigenvalues through the Arnoldi method by linking with the ARPACK package. Transient analysis in forward and adjoint mode is possible with or without precursors. Spatial discretization is performed using a second order accurate finite volume method.

DALTON uses an adaptive time-stepping algorithm that is based on the use of the second order time-accurate Backward-2 scheme. This scheme is fully implicit and unconditionally stable. We illustrate the implementation by looking at the forward equation. The Backward-2 scheme applied to the multigroup system of flux and precursor equations reads

$$\begin{aligned} \frac{1}{v\Delta t}(w_1^{n+1}\phi_g^{n+1} + w_2^n\phi_g^n + w_3^{n-1}\phi_g^{n-1}) = \\ (\nabla \cdot D\nabla - \Sigma_{t,g})\phi_g^{n+1} + \sum_{g'=1}^G \Sigma_s(g' \rightarrow g)\phi_{g'}^{n+1} + \sum_{k=1}^K \lambda_k C_k^{n+1} \chi_{d,k} \\ + (1 - \beta)\chi_p \sum_{g'=1}^G \nu \Sigma_{fg'}\phi_{g'}^{n+1} + Q_{g,ext}^{n+1} \end{aligned} \quad (\text{B.1})$$

$$\frac{1}{\Delta t}(w_1^{n+1}C_k^{n+1} + w_2^n C_k^n + w_3^{n-1}C_k^{n-1}) = -\lambda C_k^{n+1} + \beta_k \sum_{g'=1}^G \nu \Sigma_{fg'}\phi_{g'}^{n+1} \quad (\text{B.2})$$

Here, $\Delta t = t^{n+1} - t^n$ is the time step and the weights, w_i , depend on the previous time-step as well. The weights are obtained by fitting a second-order polynomial through the points $n - 1$, n and $n + 1$, differentiating once and evaluating at $n + 1$.

The precursor concentration at the new time level is eliminated from the flux equation [115]. Effectively the system can then be solved in a decoupled manner by solving for the multigroup flux first and subsequently for the precursor groups. The flux equation reads

$$(-\nabla \cdot D\nabla + \Sigma_{t,g}^*)\phi_g^{n+1} = \sum_{g'=1}^G \Sigma_s(g' \rightarrow g)\phi_{g'}^{n+1} + \chi \sum_{g'=1}^G \nu\Sigma_{fg'}\phi_{g'}^{n+1} + Q_g^{n+1}, \quad (\text{B.3})$$

where the various parameters in the equation can be derived from the flux and precursor equations:

$$\Sigma_{t,g}^* = \Sigma_{t,g} + \frac{w_1^{n+1}}{v\Delta t} \quad (\text{B.4})$$

$$\chi = (1 - \beta)\chi_p + \sum_{k=1}^K \beta_k \lambda_k \gamma_k \chi_{d,k} \quad (\text{B.5})$$

$$\gamma_k = \frac{\Delta t}{w_1^{n+1} + \lambda_k \Delta t} \quad (\text{B.6})$$

$$Q_g^{n+1} = Q_{ext,g}^{n+1} + \sum_{k=1}^K \lambda_k \gamma_k \left(\frac{w_2^n C^n + w_3^{n-1} C^{n-1}}{\Delta t} \right) \chi_{d,k} - \left(\frac{w_2^n \phi^n + w_3^{n-1} \phi^{n-1}}{v\Delta t} \right) \quad (\text{B.7})$$

Whether a time step is accepted or not depends on the maximum allowed absolute error, ATOL, and relative error, RTOL, as supplied by the user.

$$\sqrt{\frac{1}{N} \sum_{i=1}^N \left(\frac{\text{LTE}_i}{\text{ATOL} + \text{RTOL} \times \phi_i} \right)^2} \leq 1 \quad (\text{B.8})$$

where LTE is the local truncation error of the Backward-2 scheme. For prediction of the time step to be used in the next step, a similar procedure is adopted.

The adjoint procedure is similar to that outlined above. The linear systems arising from discretization are solved using preconditioned CG where the preconditioner is based on an incomplete factorization. In the multigroup case, acceleration of the Gauss-Seidel group by group solution procedure is obtained by the techniques introduced in references [116, 117]. Another option available is to use a GCR Krylov acceleration technique where the preconditioner consists of the Gauss-Seidel procedure.

In order to model the void regions, such as helium cavities, the adoption of directionally dependent diffusion in r-z geometry has been incorporated as an option.

B.2 The thermal-hydraulics code THERMIX

THERMIX-DIREKT [48] is a 2D thermal hydraulics code that consists of the two modules THERMIX (heat conduction and thermal radiation) and DIREKT (convection).

In the DIREKT part of the code the pressure field of the moving fluid for a two-dimensionally cylindrical geometry is solved by linking the equations for conservation of mass and momentum:

$$\frac{\partial \rho}{\partial t} + \rho \nabla \cdot \mathbf{v} = S \quad (\text{B.9})$$

$$\rho \frac{\partial \mathbf{v}}{\partial t} + \rho \nabla \cdot (\mathbf{v}\mathbf{v}) = \nabla \cdot \bar{\bar{\tau}} - \nabla p + \rho \mathbf{g} \quad (\text{B.10})$$

In order to avoid a time consuming procedure, a simplification is introduced, to deal with the terms for momentum flux and the stress tensor:

$$\rho \nabla \cdot (\mathbf{v}\mathbf{v}) - \nabla \cdot \bar{\bar{\tau}} = W \rho \mathbf{v} \quad (\text{B.11})$$

In this equation W is the flow resistance described by empirical laws.

The numerical method of the staggered grid definition is used for the spatial discretization [118]. In the temporal discretization the explicit, implicit or Crank-Nicholson integration methods can be used.

The energy equation including a source term q_f''' is used for calculating the fluid temperature field:

$$\rho c_p \frac{\partial T_f}{\partial t} + \rho c_p \nabla \cdot (\mathbf{v} T_f) = \nabla \cdot (k \nabla T_f) + q_f''' \quad (\text{B.12})$$

The source term represents the heat transfer of the fluid with solid and energy transfer by means of a mass source (or sink) within the control volume:

$$q_f''' = hA \cdot (T_s - T_f) + c_p \cdot \dot{m} \cdot T_{f,m} \quad (\text{B.13})$$

In the THERMIX (conduction) part of the code, the energy conservation equation is solved for steady state or time dependent cases considering the solid material:

$$\rho c_p \frac{\partial (T_s)}{\partial t} = \nabla \cdot (k \nabla T_s) + q_s''' \quad (\text{B.14})$$

in which case the heat source for the solid material q_s''' is defined as:

$$q_s''' = q_{nuc}''' - hA \cdot (T_s - T_f) \quad (\text{B.15})$$

The last term in Eq. (B.15) links the DIREKT (convection) part of the program with the THERMIX (conduction) part. A solution for the pressure and temperature field

is found after an iterative procedure in which the heat transfer between solid and fluid part is updated for each iteration.

The pebble bed is treated as a homogeneous material, having an effective conductivity based on the Zehner-Schlünder relation [119]. In this relation not only conductivity through touching pebbles is taken into account, but also radiation between the pebbles and a convective effect caused by mixing of the helium fluid in the direction perpendicular to the flow direction. The THERMIX-DIREKT code has several built-in libraries for heat conductivity, heat capacity and heat transfer.

At the boundary of the conduction model a fixed temperature or a reflective boundary condition is prescribed. For the convection model, the coolant inlet temperature and outlet pressure are used as boundary conditions.

C

Coefficients used in stress analysis equations

$$K_1 = -\frac{2r^3r_a^3(1-2\mu) + r_a^3r_b^3(1+\mu)}{2Er^2(r_b^3 - r_a^3)} \quad (\text{C.1})$$

$$K_2 = \frac{2r^3r_b^3(1-2\mu) + r_a^3r_b^3(1+\mu)}{2Er^2(r_b^3 - r_a^3)} \quad (\text{C.2})$$

$$K_3 = -\frac{2r^3r_a^3(1-2\nu) + r_a^3r_b^3(1+\nu)}{2r^2(r_b^3 - r_a^3)} \quad (\text{C.3})$$

$$K_4 = \frac{2r^3r_b^3(1-2\nu) + r_a^3r_b^3(1+\nu)}{2r^2(r_b^3 - r_a^3)} \quad (\text{C.4})$$

$$K_5 = \frac{r_a^3r_b^3 \ln \frac{r_a}{r_b}}{r^2(r_b^3 - r_a^3)} + \frac{r}{3} \quad (\text{C.5})$$

$$K_6 = -\frac{r_a^3r_b^3 \ln \frac{r_a}{r_b}}{r^2(r_b^3 - r_a^3)} + \frac{2r}{3} \quad (\text{C.6})$$

$$K_7 = \frac{2(\nu - \mu)}{3E(\nu - 1)} \left[\frac{r_b^3(r^3 - r_a^3) \ln r_b - r_a^3(r^3 - r_b^3) \ln r_a}{r^2(r_b^3 - r_a^3)} - r \ln r \right] \quad (\text{C.7})$$

Expressions used with Eq. 3.30

Eq. 3.30 can also be written as:

$$\begin{pmatrix} \dot{\sigma}_{r,I} \\ \dot{\sigma}_{r,O} \\ \dot{\sigma}_{r,X} \end{pmatrix} - \mathbf{B} \begin{pmatrix} \sigma_{r,I} \\ \sigma_{r,O} \\ \sigma_{r,X} \end{pmatrix} = \mathbf{G}(t) \quad (\text{C.8})$$

in which

$$\mathbf{G}(t) = \begin{pmatrix} x_0 \\ y_0 \\ z_0 \end{pmatrix} + \begin{pmatrix} x_1 \\ y_1 \\ z_1 \end{pmatrix} t \quad (\text{C.9})$$

and

$$\mathbf{B} = \begin{pmatrix} B_{11} & B_{12} & B_{13} \\ B_{21} & B_{22} & B_{23} \\ B_{31} & B_{32} & B_{33} \end{pmatrix} \quad (\text{C.10})$$

where

$$B_{11} = (-J_5 a_4 c_I) / Z \quad (\text{C.11})$$

$$B_{12} = (-J_6 e_3 c_O + J_4 d_3 c_O) / Z \quad (\text{C.12})$$

$$B_{13} = (-J_6 e_4 c_O + J_4 d_4 c_O + J_6 f_3 c_X) / Z \quad (\text{C.13})$$

$$B_{21} = a_4 c_I J_3 / Z \quad (\text{C.14})$$

$$B_{22} = (-J_2 d_3 c_O - J_1 e_3 c_O) / Z \quad (\text{C.15})$$

$$B_{23} = (-J_1 e_4 c_O - J_2 d_4 c_O + J_1 f_3 c_X) / Z \quad (\text{C.16})$$

$$B_{31} = -J_9 a_4 c_I / Z \quad (\text{C.17})$$

$$B_{32} = (-J_7 d_3 c_O + J_8 e_3 c_O) / Z \quad (\text{C.18})$$

$$B_{33} = (J_8 e_4 c_O - J_7 d_4 c_O - J_8 f_3 c_X) / Z \quad (\text{C.19})$$

$$Z = (e_2 - f_1)(b_2 c_1 + (b_1 - a_2)(d_1 - c_2)) - (b_1 - a_2)e_1 d_2 \quad (\text{C.20})$$

$$J_1 = d_2(a_2 - b_1) \quad (\text{C.21})$$

$$J_2 = (a_2 - b_1)(f_1 - e_2) \quad (\text{C.22})$$

$$J_3 = c_1(e_2 - f_1) \quad (\text{C.23})$$

$$J_4 = b_2(e_2 - f_1) \quad (\text{C.24})$$

$$J_5 = (c_2 - d_1)(e_2 - f_1) + e_1 d_2 \quad (\text{C.25})$$

$$J_6 = d_2 b_2 \quad (\text{C.26})$$

$$J_7 = e_1(a_2 - b_1) \quad (\text{C.27})$$

$$J_8 = (b_1 - a_2)(c_2 - d_1) - b_2 c_1 \quad (\text{C.28})$$

$$J_9 = e_1 c_1 \quad (\text{C.29})$$

$$(\text{C.30})$$

$$x_0 = 1/Z \begin{pmatrix} J_4(-c_3\alpha_{r,S}\dot{T}_S - c_4\alpha_{t,S}\dot{T}_S + d_5(\dot{S}_{r,O} + \alpha_{r,O}\dot{T}_O) \\ + d_6(\dot{S}_{t,O} + \alpha_{t,O}\dot{T}_O)) + J_5(-a_1\frac{dp}{dt} - a_3c_I(p_{n-1} - \frac{dp}{dt}t_{n-1}) \\ - a_5(\dot{S}_{r,I} + \alpha_{r,I}\dot{T}_I) - a_6(\dot{S}_{t,I} + \alpha_{t,I}\dot{T}_I) + b_3\alpha_{r,S}\dot{T}_S \\ + b_4\alpha_{t,S}\dot{T}_S) + J_6(f_2\frac{dq}{dt} + f_4c_X(q_{n-1} - \frac{dq}{dt}t_{n-1}) \\ + f_5(\dot{S}_{r,X} + \alpha_{r,X}\dot{T}_X) + f_6(\dot{S}_{t,X} + \alpha_{t,X}\dot{T}_X) - e_5(\dot{S}_{r,O} + \alpha_{r,O}\dot{T}_O) \\ - e_6(\dot{S}_{t,O} + \alpha_{t,O}\dot{T}_O)) \end{pmatrix} \quad (C.31)$$

$$x_1 = 1/Z(-J_5a_3c_I\frac{dp}{dt} + J_6f_4c_X\frac{dq}{dt}) \quad (C.32)$$

$$y_0 = 1/Z \begin{pmatrix} J_1(f_2\frac{dq}{dt} + f_4c_X(q_{n-1} - \frac{dq}{dt}t_{n-1}) + f_5(\dot{S}_{r,X} + \alpha_{r,X}\dot{T}_X) \\ + f_6(\dot{S}_{t,X} + \alpha_{t,X}\dot{T}_X) - e_5(\dot{S}_{r,O} + \alpha_{r,O}\dot{T}_O) - e_6(\dot{S}_{t,O} + \alpha_{t,O}\dot{T}_O)) \\ + J_2(c_3\alpha_{r,S}\dot{T}_S + c_4\alpha_{t,S}\dot{T}_S - d_5(\dot{S}_{r,O} + \alpha_{r,O}\dot{T}_O) \\ - d_6(\dot{S}_{t,O} + \alpha_{t,O}\dot{T}_O)) + J_3(a_1\frac{dp}{dt} + a_3c_I(p_{n-1} - \frac{dp}{dt}t_{n-1}) \\ + a_5(\dot{S}_{r,I} + \alpha_{r,I}\dot{T}_I) + a_6(\dot{S}_{t,I} + \alpha_{t,I}\dot{T}_I) - b_3\alpha_{r,S}\dot{T}_S - b_4\alpha_{t,S}\dot{T}_S) \end{pmatrix} \quad (C.33)$$

$$y_1 = 1/Z(J_1f_4c_X\frac{dq}{dt} + J_3a_3c_I\frac{dp}{dt}) \quad (C.34)$$

$$z_0 = 1/Z \begin{pmatrix} J_7(c_3\alpha_{r,S}\dot{T}_S + c_4\alpha_{t,S}\dot{T}_S - d_5(\dot{S}_{r,O} + \alpha_{r,O}\dot{T}_O) - d_6(\dot{S}_{t,O} + \alpha_{t,O}\dot{T}_O)) \\ + J_8(-f_2\frac{dq}{dt} - f_4c_X(q_{n-1} - \frac{dq}{dt}t_{n-1}) - f_5(\dot{S}_{r,X} + \alpha_{r,X}\dot{T}_X) \\ - f_6(\dot{S}_{t,X} + \alpha_{t,X}\dot{T}_X) + e_5(\dot{S}_{r,O} + \alpha_{r,O}\dot{T}_O) + e_6(\dot{S}_{t,O} + \alpha_{t,O}\dot{T}_O)) \\ + J_9(-a_1\frac{dp}{dt} - a_3c_I(p_{n-1} - \frac{dp}{dt}t_{n-1}) \\ - a_5(\dot{S}_{r,I} + \alpha_{r,I}\dot{T}_I) - a_6(\dot{S}_{t,I} + \alpha_{t,I}\dot{T}_I) + b_3\alpha_{r,S}\dot{T}_S + b_4\alpha_{t,S}\dot{T}_S) \end{pmatrix} \quad (C.35)$$

$$z_1 = 1/Z(-J_8f_4c_X\frac{dq}{dt} - J_9a_3c_I\frac{dp}{dt}) \quad (C.36)$$

Nomenclature

Abbreviations

AGR	Advanced Gas-Cooled Reactor
AHTR	Advanced High-Temperature Reactor
AVR	Arbeitsgemeinschaft Versuchsreaktor
CRW	Control Rod Withdrawal
DLOFC	Depressurized Loss Of Forced Cooling
EOL	End Of Life
FIMA	Fission per Initial Metal Atom
HTGR	High Temperature Gas-cooled Reactor
HTR	High Temperature Reactor
HTR-PM	High Temperature gas-cooled Reactor Pebble-bed Module
HTTR	High Temperature engineering Test Reactor
IPyC	Inner Pyrolytic Carbon
LSPBR	Liquid Salt-cooled Pebble-Bed Reactor
NEA	Nuclear Energy Agency
NGNP	Next Generation Nuclear Plant
OECD	Organization for Economic Co-operation and Development
OPyC	Outer Pyrolytic Carbon
OTTO	Once-Through-Then-Out
PASTA	PARTicle Stress Analysis
PBMR	Pebble Bed Modular Reactor
PCRV	Pre-stressed Concrete Reactor Vessel
PK	Point Kinetics
PLOFC	Pressurized Loss Of Forced Cooling
RAPHAEL	ReACTor for Process Heat And ELectricity
RCCS	Reactor Cavity Cooling System
RPV	Reactor Pressure Vessel
S-I (or I-S)	Sulphur Iodine

SCRAM	Safety Cut Rope Axe Man, i.e. insertion of control rods
SiC	Silicon Carbide
THTR	Thorium High Temperature Reactor
TRISO	Tri-isotropic
VHTR	Very High Temperature Reactor

Symbols

$\langle l^2 \rangle$	Mean square length of the fission chain
α	Thermal expansion coefficient
α_{ji}	Probability that the decay of nuclide j will yield nuclide i
β	Delayed neutron fraction
\mathbf{L}	Stress transformation matrix
χ_d	Delayed neutron energy spectrum
χ_p	Prompt neutron energy spectrum
\dot{S}	Dimensional change rate
η	Viscosity (dynamic)
η_{Carnot}	The Carnot thermodynamic efficiency
γ	Yield
γ_{ji}	Probability that a neutron interaction with nuclide j will yield nuclide i
Λ	Mean neutron generation time
λ_i	Decay constant of nuclide i
λ_k	Delayed neutron decay constant of group k
λ_{tot}	Total heat transfer coefficient
μ	Poisson's ratio
ν	Average number of new neutrons per fission
ν	Poisson ratio in creep
$\bar{\bar{\sigma}}$	Stress tensor
Φ	Failure probability
ϕ	Scalar neutron flux
ψ	Friction factor
ρ	Reactivity or density
σ_{med}	Median strength
σ	Stress

σ_{ai}	Absorption cross section of nuclide i
σ_{aj}	Absorption cross section of nuclide j
Σ_f	Fission cross section (macroscopic)
$\Sigma_s(g' \rightarrow g)$	Scatter cross section (macroscopic), from energy group g' to group g
Σ_t	Total cross section (macroscopic)
ε	Porosity of the pebble-bed
ε	Strain
A	Heat transfer area
A, B	Coefficients in incremental stress Eqs. (3.19,3.20)
a, b	Constants in Redlich-Kwong equation of state Eq. (3.3)
B	Geometric buckling
C	Concentration of fission products
c	Creep (irradiation) coefficient
c_p	Thermal capacity
C_k	Precursor concentration of group k
D	Neutron diffusion coefficient
D_{fis}	Diffusion coefficient of fission products
E	Young's modulus of elasticity
g	Gravitational acceleration
h	Heat transfer (between pebble surface and helium) coefficient
K	Constant (see App. C)
k	Thermal conductivity
M	Migration length
N	Atomic concentration
O/f	Oxygen release per fission
p	(internal) Pressure
Pr	Prandtl number
Q	Source (Fission products or neutrons)
q	External pressure
q'''	Power density
Q_{ext}	External neutron source
q_f'''	Power density in fluid

Nomenclature

q'''_{nuc}	Power (nuclear) density
q'''_s	Power density in solid material
R	Universal gas constant
r	Radius
R_{fuel}	Radius of the fuel zone in the pebble
R_{peb}	Radius of the pebble
Re	Reynolds number
S	Mass source
T	Temperature
t	Time or neutron fluence
T_{cold}	The temperature of a cold reservoir
$T_{f,m}$	Fluid temperature of mass source
T_{hot}	The temperature of a hot reservoir
t_{irr}	Irradiation time
u	Displacement
v	Velocity
V_m	Molar volume
W	Flow resistance
w	Weighting factor
Z	Constant for oxygen release
z	Axial coordinate
k_{eff}	Effective multiplication factor
k_{∞}	Infinite medium multiplication factor

Subscripts

a, b	Inner or outer
d	Decay heat
ext	External
f	Fluid
g	Neutron energy group
he	Helium
I	IPyC layer
i	Inner

<i>kernel</i>	Fuel kernel
<i>m</i>	Modulus of Weibull distribution
<i>max</i>	Maximum (located at the pebble center)
<i>O</i>	OPyC layer
<i>o</i>	Outer
<i>p</i>	Prompt
<i>r</i>	Radial direction
<i>rod</i>	Control rod
<i>S</i>	SiC layer
<i>s</i>	Solid
<i>t</i>	Tangential direction
<i>t</i>	Total
<i>X</i>	Graphite matrix layer
<i>z</i>	Axial

Bibliography

- [1] International Energy Agency. Energy Technology Perspectives; Scenarios & Strategies to 2050. Technical report, OECD/IEA, France, 2008.
- [2] International Atomic Energy Agency. Nuclear Power Reactors in the World. Technical Report IAEA-RDS-2/28, Vienna, Austria, July 2008. ISBN 978-92-0-107708-0.
- [3] C.H. Forsberg. Hydrogen, nuclear energy, and the advanced high-temperature reactor. *International Journal of Hydrogen Energy*, 28, 2003.
- [4] International Energy Agency. Prospects for hydrogen and fuel cells, December 2005. OECD/IEA.
- [5] G. Melese and R. Katz. *Thermal and flow design of helium-cooled reactors*. American Nuclear Society, 1984. ISBN 0-89448-027-8.
- [6] C.A. Rennie. Achievements of the Dragon project. *Annals of Nuclear Energy*, 5(305):8–10, 1978.
- [7] R. Bäumer et al. *AVR: experimental high temperature reactor; 21 years of successful operation for a future energy technology*. Assoc. of German Engineers (VDI), The Soc. for Energy Technologies, VDI-Verlag GmbH, Düsseldorf, 1990. ISBN 3-18401015-5.
- [8] J.L. Everett and E. Kohler. Peach Bottom Unit No. 1: A High-Performance Helium-Cooled Nuclear Power Plant. *Annals of Nuclear Energy*, 5(321), 1978.
- [9] A. Habush and A. Harris. 330-MW(e) Fort St. Vrain High-Temperature Gas-Cooled Reactor. *Nuclear Engineering and Design*, 7(312), 1968.
- [10] Das 300 MW Thorium-Hochtemperatur-Kernkraftwerk THTR. *Atomwirtschaft*, May 1971.
- [11] K. Kugeler and R. Schulten. *Hochtemperaturreaktortechnik*. Springer, 1989.
- [12] W.M. Stacey. *Nuclear Reactor Physics*. John Wiley & Sons, Inc., 2001. ISBN 0-471-39127-1.
- [13] H. Reutler and G.H. Lohnert. The Modular High-Temperature Reactor. *Nuclear Technology*, 62(22), July 1983.

- [14] G.H. Lohnert. Topical issue on Japan's HTTR. *Nuclear Engineering and Design*, 233(1-3), 2004.
- [15] G.H. Lohnert. Topical issue on China's HTR-10. *Nuclear Engineering and Design*, 218(1-3), 2002.
- [16] A. Koster, H.D. Matzner, and D.R. Nicholsi. PBMR design for the future. *Nuclear Engineering and Design*, 222:231–245, 2003.
- [17] Z. Zhang, Z. Wu, and F. Li. Design aspects of the Chinese modular high-temperature gas-cooled reactor HTR-PM. *Nuclear Engineering and Design*, 236:485–490, 2006.
- [18] S. Shiozawa, S. Fujikawa, T. Iyoku, K. Kunitomi, and Y. Tachibana. Overview of HTTR design features. *Nuclear Engineering and Design*, 233:11–21, 2004.
- [19] Z. Zhang and Y. Sun. Economic potential of modular reactor nuclear power plants based on the Chinese HTR-PM project. *Nuclear Engineering and Design*, 237:2265–2274, 2007.
- [20] U.S. DOE Nuclear Energy Research Advisory Committee and the Generation IV International Forum. *A Technology Roadmap for Generation IV Nuclear Energy Systems*. December 2002.
- [21] P.E. MacDonald. NGNP Preliminary Point Design - Results of the Initial Neutronics and Thermal-Hydraulics Assessments. Technical Report INEEL/EXT-03-00870, Idaho National Laboratory, 2003.
- [22] General Atomics. Gas Turbine-Modular Helium Reactor (GT-MHR) Conceptual Design Description Report. Technical Report 910720, GA, USA, July 1996.
- [23] H.D. Gougar, A.M. Ougouag, W.K. Terry, and K. Ivanov. Design of Pebble-Bed Reactors Using a Genetic Algorithm. In *PHYSOR-2004*, Chicago, April 2004.
- [24] A.M. Ougouag, H.D. Gougar, W.K. Terry, R. Mphahlele, and K. Ivanov. Optimal Moderation in the Pebble-Bed Reactor for Enhanced Passive Safety and Improved Fuel Utilization. In *PHYSOR-2004*, Chicago, April 2004.
- [25] D. Hittner et al. RAPHAEL, a European project for the development of HTR/VHTR technology for industrial process heat supply and cogeneration. In *HTR2006: 3rd International Topical Meeting on High Temperature Reactor Technology*, Johannesburg, South Africa, October 2006.
- [26] E.J.M. Wallerbos. *Reactivity effects in a pebble-bed type nuclear reactor. An experimental and calculational study*. PhD thesis, Delft University of Technology, Delft, The Netherlands, 1998.

-
- [27] E.E. Bende. *Plutonium burning in a pebble-bed type High Temperature Nuclear Reactor*. PhD thesis, Delft University of Technology, Delft, The Netherlands, 2000.
- [28] W.F.G. van Rooijen. *Improving Fuel Cycle Design and Safety Characteristics of a Gas Cooled Fast Reactor*. PhD thesis, Delft University of Technology, Delft, The Netherlands, 2006.
- [29] E.C. Verkerk. *Dynamics of the pebble-bed nuclear reactor in the direct Brayton cycle*. PhD thesis, Delft University of Technology, Delft, The Netherlands, 2000.
- [30] J.F. Kikstra. *Modelling, Design and Control of a Cogenerating Nuclear Gas Turbine*. PhD thesis, Delft University of Technology, Delft, The Netherlands, 2001.
- [31] C.W. Forsberg. The advanced high-temperature reactor: high-temperature fuel, liquid salt coolant, liquid-metal-reactor plant. *Progress in Nuclear Energy*, 47(1-4):32–43, 2005.
- [32] S.J. de Zwaan, B. Boer, D. Lathouwers, and J.L. Kloosterman. Static design of a liquid-salt-cooled pebble bed reactor (LSPBR). *Annals of Nuclear Energy*, 34:83–92, 2007.
- [33] G.H. Lohnert. Technical design features and essential safety-related properties of the HTR-module. *Nuclear Engineering and Design*, 121:259–275, 1990.
- [34] K. Krüger. *Experimentelle Simulation eines Kühlmittelverlust-Störfalls mit dem AVR-Reaktor*. PhD thesis, FZ Jülich, Germany, 1989.
- [35] Z. Wu, D. Lin, and D. Zhong. The design features of the HTR-10. *Nuclear Engineering and Design*, 218:25–32, 2002.
- [36] X. Jing, X. Xu, Y. Yang, and R. Qu. Prediction calculations and experiments for the first criticality of the 10 MW High Temperature Gas-cooled Reactor-Test Module. *Nuclear Engineering and Design*, 218:43–49, 2002.
- [37] Zhu Ling Gao and Lei Shi. Thermal hydraulic calculation of the htr-10 for the initial and equilibrium core. *Nuclear Engineering and Design*, 218:51–64, 2002.
- [38] IAEA. Hydrogen as an energy carrier and its production by nuclear power. Tecdoc-1085, International Atomic Energy Agency, Vienna, Austria, 2001.
- [39] R. Hino, K. Haga, H. Aita, and K. Sekita. R&D on Hydrogen Production by High-Temperature Electrolysis of Steam. *Nuclear Engineering and Design*, 233:363–375, 2004.

- [40] J.S. Herring, J.E. O'Brien, C.M. Stoots, G.L. Hawkes, and J.J. Hartvigsen. High Temperature Electrolysis for Hydrogen Production Using Nuclear Energy. In *Global 2005*, page Paper 501, October 2005. Tsukuba, Japan.
- [41] C.L. Brown, J.F. Funk, and S.K. Showalter. High Efficiency Generation of Hydrogen Fuels Using Nuclear Power. Technical Report GAA23451, General Atomics, San Diego.
- [42] Shinji Kubo, Seiji Kasahara, Hiroyuki Okuda, Atsuhiko Terada, Nobuyuki Tanaka, Yoshitomo Inaba, Hirofumi Ohashi, Yoshiyuki Inagaki, Kaoru Onuki, and Ryutaro Hino. A pilot test plan of the thermochemical water-splitting iodine-sulfur process. *Nuclear Engineering and Design*, 233:355–362, October 2004.
- [43] Shinji Kubo, Hayato Nakajima, Seiji Kasahara, Syunichi Higashi, Tomoo Masaki, Hiroyoshi Abe, and Kaoru Onuki. A demonstration study on a closed-cycle hydrogen production by the thermochemical water-splitting iodine-sulfur process. *Nuclear Engineering and Design*, 233:347–354, October 2004.
- [44] A. Terada, J. Iwatsuki, S. Ishikura, H. Noguchi, S. Kubo, H. Okuda, S. Kasahara, N. Tanaka, H. Ota, K. Onuki, and R. Hino. Development of Hydrogen Production Technology by Thermochemical Water Splitting IS Process Pilot Test Plan. *Nuclear Science and Technology*, 44(3):477482, 2007.
- [45] Y. Kato, T. Nitawaki, and Y. Muto. Medium temperature carbon dioxide gas turbine reactor. *Nuclear Engineering and Design*, 230:195–207, 2003.
- [46] J.N. Smith, H.C. van Ness, and M.M. Abott. *Introduction to Chemical Engineering Thermodynamics*, volume 6th Ed. McGraw-Hill, 2001. ISBN 0-07-118957-2.
- [47] B. Boer, D. Lathouwers, M. Ding, and J.L. Kloosterman. Coupled neutronics / thermal hydraulics calculations for High Temperature Reactors with the DALTON - THERMIX code system. In *International Conference on the Physics of Reactors (PHYSOR)*, 2008. Interlaken, Switzerland.
- [48] S. Struth. *Thermix-Direkt: Ein Rechenprogramm zur instationären zweidimensionalen Simulation thermohydraulischer Transienten*. FZ Jülich, Germany, 1995.
- [49] J. Oppe, J.B.M. de Haas, and J.C. Kuijper. *PANTHERMIX (PANTHER-THERMIX) User Manual*. Report ECN-I98-019, ECN Petten, June 1998.
- [50] Bismark Tyobeka, Kostadin Ivanov, and Andreas Pautz. Utilization of two-dimensional deterministic transport methods for analysis of pebble-bed reactors. *Annals of Nuclear Energy*, 34:396405, 2007.

-
- [51] W.K. Terry, H.D. Gougar, and A.M. Ougouag. Direct deterministic method for neutronics analysis and computation of asymptotic burnup distribution in a recirculating pebble-bed reactor. *Annals of Nuclear Energy*, 29:1345–1364, 2002.
- [52] T.J. Downar et al. PARCS: purdue advanced reactor core simulator. *PHYSOR-2002*, October 2002. Seoul, Korea.
- [53] Won-Jae Lee, Jae-Jun Jeong, Seung-Wook Lee, and Jongwha Chang. Development of MARS-GCR/V1 for Thermal- Hydraulic Safety Analysis of Gas-Cooled Reactor System. *Nuclear Engineering and Technology*, 37(587), 2005.
- [54] H. Gerwin and E. Teuchert W. Scherer. The TINTE Modular Code System for Computational Simulation of Transient Processes in the Primary Circuit of a Pebble-Bed High-Temperature Gas-Cooled Reactor. *Nuclear Science and Engineering*, 103:302–312, 1989.
- [55] SCALE-5. *Modular Code System for Performing Standardized Computer Analysis for Licensing Evaluations*. Oak Ridge National Laboratory, Tennessee, USA, 2005.
- [56] H.J. Rütten and K.A. Haas. *V.S.O.P. (99/3)-Input Description*. Institut für Sicherheitsforschung und Reaktortechnik (ISR), Forschungszentrum Jülich, 2003.
- [57] Karl O. Ott and Robert J. Neuhold. *Introductory Nuclear Reactor Dynamics*. American Nuclear Society, 1985. ISBN 0-89448-029-4.
- [58] N.M. Greene, L.M. Petrie, and R.M. Westfall. Nitawl-3: Scale system module for performing resonance shielding and working library production. Technical report, Oak Ridge National Laboratory, 2005. Oak Ridge, Tennessee, USA.
- [59] N.M. Greene. Bonami: Resonance self-shielding by the bondarenko method. Technical report, Oak Ridge National Laboratory, 2005. Oak Ridge, Tennessee, USA.
- [60] N.M. Greene, L.M. Petrie, and R.M. Westfall. Xsdrnpm: a one-dimensional discrete-ordinates code for the transport analysis. Technical report, Oak Ridge National Laboratory, 2005. Oak Ridge, Tennessee, USA.
- [61] E.E. Bende, A.H. Hogenbirk, J.L. Kloosterman, and H. van Dam. Analytical calculation of the average dancoff factor for a fuel kernel in a pebble bed high-temperature reactor. *Nuclear Science and Engineering*, 133(2):147–162, October 1999.

- [62] H. Gerwin and W. Scherer. Treatment of the Upper Cavity in a Pebble-Bed High Temperature Gas-Cooled Reactor by Diffusion Theory. *Nuclear Science and Engineering*, 97:9–19, 1987.
- [63] L. Massimo. *Physics of high temperature reactors*. Pergamon Press, 1st edition, 1976. ISBN 0-08-019616-0.
- [64] Y. Yang, Z. Luo, X. Jing, and Z. Wu. Fuel management of the HTR-10 including the equilibrium state and the running -in phase. *Nuclear Engineering and Design*, 218:33–41, 2002.
- [65] IAEA. Evaluation of high temperature gas cooled reactor performance: Benchmark analysis related to initial testing of the HTTR and HTR-10. Technical Report IAEA-TECDOC-1382, International Atomic Energy Agency, November 2003.
- [66] M. Zha, S. Zhong, R. Chen, and S. Li. Temperature Measuring System of the In-core Components for Chinese 10 MW High Temperature Gas-cooled Reactor. *Journal of Nuclear Science and Technology*, 39(10):1086–1093, October 2002.
- [67] S. Hu, R. Wang, and Z. Gao. Transient tests on blower trip and rod removal at the HTR-10. *Nuclear Engineering and Design*, 236:677–680, 2006.
- [68] S. Hu, R. Wang, and Z. Gao. Safety demonstration tests on HTR-10. In *2nd International Topical Meeting on High Temperature Reactor Technology*, Beijing, China, September 2004.
- [69] T. Iyoku, W. Jahn, and W. Rehm. Analytical Investigations of the AVR Loss-of-Coolant Accident Simulation Test-LOCA (HTA-5). Technical Report KFA-ISR-IB-3/92, Forschungszentrum Jülich, Germany, March 1992.
- [70] M. Ishihara. Specific Analysis with the Heat Transport Code Heating-3D of the LOCA Simulation Test with the AVR Reactor. Technical Report KFA-ISR-IB-13/92, Forschungszentrum Jülich, Germany, September 1992.
- [71] OECD. PBMR coupled neutronics/thermal hydraulics transient benchmark - the PBMR-400 core design - benchmark description. Technical Report Draft-V03, Nuclear Energy Agency, September 2005.
- [72] G. Strydom. TINTE results of the PBMR benchmark. PBMR Ltd., Personal communication, 2008.
- [73] J.W. Prados and J.L. Scott. Mathematical model for predicting coated-particle behavior. *Nuclear Applications*, 2:402–414, October 1966.
- [74] G.K. Miller and R.G. Bennett. Analytical solutions for stresses in triso-coated particles. *Journal of Nuclear Materials*, 206:35–49, 1993.

-
- [75] Jing Wang, Ronald G. Ballinger, and Heather J. Maclean. TIMCOAT: an integrated fuel performance model for coated particle fuel. *Nuclear Technology*, 148:68–96, October 2004.
- [76] I-NERI. Development for improved models and designs for coated particle gas reactor fuels. Technical Report INEEL/EXT-05-02615, INEEL, 2004.
- [77] IAEA. Current status and future development of modular high temperature gas cooled reactor technology. TECDOC 1198, International Atomic Energy Agency, February 2001.
- [78] B. Liu, T. Liang, and C. Tang. A review of triso-coated particle nuclear fuel performance models. *Rare Metals*, 25(6):337–342, october 2006.
- [79] T.X. Liang, H.S. Zhao, C.H. Tang, and K. Verfondern. Irradiation performance and modeling of the HTR-10 coated fuel particles. *Nuclear Engineering and Design*, 236:1922–1927, 2006.
- [80] M. Phelip, F. Michel, M. Pelletier, G. Degeneve, and P. Guillermier. The ATLAS HTR fuel simulation code. Objectives, description and first results. In *Proc. Intern. Topical Meet. On High Temperature Reactor Technology*, Beijing China, September 2004.
- [81] A.M. Ougouag, J.L. Kloosterman, W.F.G van Rooijen, H.D. Gougar, and W.K. Terry. Investigation of the bounds on the particle packing in pebble-bed high temperature reactors. *Nuclear Engineering and Design*, 236:669–676, 2006.
- [82] K. Sawa, S. Shiozawa, K. Minato, and K. Fukuda. Development of a coated fuel particle failure model under high burnup irradiation. *Journal of Nuclear Science and Technology*, 33(9):712, 1996.
- [83] B. Boer, J.L. Kloosterman, and A.M. Ougouag. Optimization of HTR fuel to reduce fuel particle failure. Vancouver, BC, Canada, September 2006. PHYSOR-2006, ANS Topical Meeting on Reactor Physics.
- [84] D. Olander. *Fundamental Aspects of Nuclear Reactor Fuel Elements*. Technical information center, Energy Research and Development Administration, 1976.
- [85] H. Nabielek, K. Verfondern, and H. Werner. Can we predict coated particle failure? A conversation on CONVOL, PANAMA and other codes. In *Technical Meeting on the Current Status and Future Prospects of Gas Cooled Reactor Fuels*. Vienna, June 2004.
- [86] E. Proksch, A. Strigl, and H. Nabielek. Production of carbon monoxide during burn-up of UO_2 kerneled HTR fuel particles. *Journal of Nuclear Materials*, 107(28), 1982.

- [87] T. Oku, M. Eto, and S. Ishiyama. Irradiation properties and strength of a fine-grained isotropic graphite. *Journal of Nuclear Materials*, 172:77–84, 1990.
- [88] T. Oku and M. Ishihara. Lifetime evaluation of graphite components for HT-GRs. *Nuclear Engineering and Design*, 227:209–217, 2004.
- [89] D. Gross and T. Seelig. *Fracture mechanics*. Springer, 2006. ISBN 3-540-24034-9.
- [90] G.K. Miller. Stresses in a spherical pressure vessel undergoing creep and dimensional changes. *International Journal of Solids and Structures*, 32(14):2077–2093, 1995.
- [91] G.K. Miller. Considerations of Irradiation-Induced Transient Creep in Fuel Particle Modeling. *Journal of Nuclear Science and Technology*, 32(10):989, October 1995.
- [92] S.P. Timoshenko and J.N. Goodier. *Theory of Elasticity*. McGraw-Hill, Inc., third edition, 1970.
- [93] G.K. Miller. Updated solutions for stresses and displacements in triso-coated fuel particles. Engineering Design File EDF-7042, Idaho National Laboratory, 2006.
- [94] W.E. Boyce and R.C. DiPrima. *Elementary differential equations and boundary value problems*. John Wiley & Sons, Inc., 6th edition, 1996. ISBN 0-471-08955-9.
- [95] R. Gontard and H. Nabilek. Performance Evaluation of Modern HTR TRISO Fuels. Technical Report HTA-IB-05/90, Forschungszentrum Jülich GmbH, Germany, July 1990.
- [96] B.J. Marsden. Irradiation damage in graphite. IAEA-TECDOC-901 XA9642900, International Atomic Energy Agency, 1995. 17-46.
- [97] W.B. Bickford. *Advanced mechanics of materials*. Addison Wesley Longman, Inc., 1998. ISBN 0-673-98195-9.
- [98] Gregory K. Miller, David A. Petti, Dominic J. Varacalle, and John T. Maki. Consideration of the effects on fuel particle behavior from shrinkage cracks in the inner pyrocarbon layer. *Journal of Nuclear Materials*, 295:205–212, March 2001.
- [99] J. Jonnet, J.L. Kloosterman, and B. Boer. Development of a stress analysis code for TRISO particles in HTRs. In *International Conference on the Physics of Reactors*, September 2008. Interlaken, Switzerland.
- [100] J.L. Kloosterman. Application of boron and gadolinium burnable poison particles in uO_2 and puO_2 in htrs. *Annals of Nuclear Energy*, 30:1807, 2003.

-
- [101] M. Fratoni and E. Greenspan. Determination of the equilibrium composition of cores with continuous fuel feed and removal using mocup. In *Joint International Topical Meeting on Mathematics & Computation and Supercomputing in Nuclear Applications (M&C + SNA 2007)*. ANS, 2007.
- [102] I.C. Gauld, O.W. Hermann, and R.M. Westfall. Origen-s: scale system module to calculate fuel depletion, actinide transmutation, fission product buildup and decay, and associated radiation source terms. Technical report, Oak Ridge National Laboratory, 2005. Oak Ridge, Tennessee, USA.
- [103] B. Boer, D. Lathouwers, M. Ding, and J.L. Kloosterman. Coupled neutronics / thermal hydraulics calculations for High Temperature Reactors with the DALTON - THERMIX code system. In *International Conference on the Physics of Reactors*, September 2008. Switzerland.
- [104] P. Mkhabela, J. Han, B. Tyobeka, K. Ivanov, F. Reitsma, and E. Sartori. Summary of Comparison and Analysis of Results from Exercises 1 & 2 of the OECD PBMR Coupled Neutronics/Thermal Hydraulics Transient Benchmark. Vancouver, BC, Canada, September 2006. PHYSOR-2006, ANS Topical Meeting on Reactor Physics.
- [105] A.C. Kadak and M.Z. Bazant. Pebble flow experiments for pebble bed reactors. *2nd International Topical Meeting on High Temperature Reactor Technology*, Sept. 2004. Beijing, China.
- [106] R. van Geemert, A.J. Quist, J.E. Hoogenboom, and H.P.M. Gibcus. Research reactor in-core fuel management optimization by application of multiple cyclic interchange algorithms. *Nuclear Engineering and Design*, 186:369–377, 1998.
- [107] Yasushi Muto and Yasuyoshi Kato. A New Pebble Bed Core Concept with Low Pressure Drop. In *Transactions of the Global 2003 Conference*, pages 1202–1209. American Nuclear Society, November 2003. New Orleans.
- [108] Yasushi Muto, Yasuyoshi Kato, and Ryoza Udagawa. Improvement of fuel temperature characteristics in a pebble bed core with horizontal flow by means of fuel zoning. In *Proceedings of ICAPP '05*, Seoul, Korea, May 2005.
- [109] R.B. Bird, W.E. Stewart, and E.N. Lightfoot. *Transport Phenomena*. Wiley, second edition, 2002.
- [110] K. Minato, T. Ogawa, K. Sawa, A. Ishikawa, T. Tomita, and S. Iida. Irradiation experiment on ZrC-coated fuel particles for High-Temperature Gas-cooled Reactors. *Nuclear Technology*, 130:272–281, June 2000.
- [111] S. Ueta, J. Aihara, A. Yasuda, H. Ishibashi, T. Takayama, and K. Sawa. Fabrication of uniform ZrC coating layer for the coated fuel particle of the very high temperature reactor. *Journal of Nuclear Materials*, 376:146–151, 2008.

- [112] P. Bardet, E. Blandford, M. Fratoni, A. Niquille, E. Greenspan, and P. Peterson. Design, Analysis and Development of the Modular PB-AHTR. In *ICAPP '08*, Anaheim, California USA, June 2008. paper 8211.
- [113] ANS Standards Committee. American national standard for decay heat power in light water reactors. Technical report, American Nuclear Society, 1979.
- [114] J. Keijzer. *Investigations of spatial effects in nuclear reactor kinetics*. PhD thesis, Delft University of Technology, Delft, The Netherlands, 1996.
- [115] A. Pautz and A. Birkhofer. DORT-TD: A Transient Neutron Transport Code with Fully Implicit Time Integration. *Nuclear Science and Engineering*, 145:299–319, 2003.
- [116] J.E. Morel and J.M. McGhee. An Outer Iteration Acceleration Technique for Time-Dependent Even-Parity S_N Calculations. *Nuclear Science and Engineering*, 116:73–85, 1994.
- [117] B.T. Adams and J.E. Morel. A Two-Grid Acceleration Scheme for the Multi-group S_N Equations with Neutron Upscattering. *Nuclear Science and Engineering*, 115:253–264, 1993.
- [118] S.V. Patankar. *Numerical heat transfer and fluid flow*. Hemisphere Publishing Corp., 1980.
- [119] P. Zehner and E.U. Schlünder. Einfluss der Wärmestrahlung und des Druckes auf den Wärmestromtransport in nicht durchströmten Schüttungen. *Chemie-Ing.-Technik*, 44:1303, 1972.

List of publications

B. Boer, D. Lathouwers, J.L. Kloosterman, T.H.J.J. van der Hagen, *Optimization of the pebble recycling scheme in a pebble-bed reactor*, Submitted to Annals of Nuclear Energy, 2008.

B. Boer, D. Lathouwers, J.L. Kloosterman, T.H.J.J. van der Hagen, *Analysis of LOFC transients in the HTR-10 and PBMR reactors with the DALTON-THERMIX code system*, Submitted to Nuclear Technology, 2008.

M. Ding, B. Boer, J.L. Kloosterman, D. Lathouwers, *Evaluation of experiments in the AVR with the DALTON-THERMIX code system*, Submitted to Nuclear Engineering and Design, 2008.

B. Boer, J.L. Kloosterman, D. Lathouwers, T.H.J.J. van der Hagen, H. van Dam, *Optimization of a Radially Cooled Pebble Bed Reactor*, Submitted to Nuclear Engineering and Design, 2008.

B. Boer, J.L. Kloosterman, D. Lathouwers, T.H.J.J. van der Hagen, H. van Dam, *Optimization of a Radially Cooled Pebble Bed Reactor*, Proc. of the 4th International Topical Meeting on High Temperature Reactor Technology (HTR-2008), Washington-DC, USA 2008.

J. Jonnet, J.L. Kloosterman, B. Boer, *Development of a stress analysis code for TRISO particles in HTRs*, International Conference on the Physics of Reactors, "Nuclear Power: a Sustainable Resource" (PHYSOR-2008), Interlaken, Switzerland, 2008.

B. Boer, D. Lathouwers, M. Ding, J.L. Kloosterman *Coupled neutronics / thermal hydraulics calculations for High Temperature Reactors with the DALTON - THERMIX code system*, International Conference on the Physics of Reactors, "Nuclear Power: a Sustainable Resource" (PHYSOR-2008), Interlaken, Switzerland, 2008.

B. Boer, A.M. Ougouag, J.L. Kloosterman and G.K. Miller, *Stress analysis of coated particle fuel in graphite of High Temperature Reactors*, Nuclear Technology (ANS) **162**:276-292, June 2008.

S.J. de Zwaan, B. Boer, D. Lathouwers and J.L. Kloosterman, *Static Design of a Liquid Salt-cooled Pebble Bed Reactor (LSPBR)*, Annals of Nuclear Energy, **34**:83-92, 2007.

B. Boer, A.M. Ougouag, G.K. Miller and J.L. Kloosterman. *Mechanical Stresses in Fuel Particles and Graphite of High Temperature Reactors*, Joint International Topical Meeting on Mathematics & Computation and Supercomputing in Nuclear

Applications (M&C+SNA 2007), Monterey, California, USA, 2007.

B. Boer, J.L. Kloosterman and A.M. Ougouag, *Optimization of HTR fuel design to reduce fuel particle failures*. International Conference on the Physics of Reactors (PHYSOR-2006), Vancouver, Canada, September 2006.

S.J. de Zwaan, B. Boer, D. Lathouwers and J.L. Kloosterman, *Neutronic Design of a Liquid Salt-cooled Pebble Bed Reactor (LSPBR)*. International Conference on the Physics of Reactors (PHYSOR-2006), Vancouver, Canada, September 2006.

B. Boer, *Feasibility of a High Temperature Nuclear Reactor as back up system for Wind power*, MSc thesis, Delft University of Technology, The Netherlands, May 2004.

B. Boer, *Thermal Hydraulic Reactor model of the Pebble Bed Modular Reactor in Flownet*, Potchefstroom University, South Africa, 2003.

Summary

The Very High Temperature Reactor (VHTR) has been selected by the international Generation IV research initiative as one of the six most promising nuclear reactor concepts that are expected to enter service in the second half of the 21st century. As one of the fourth generation nuclear reactors, the VHTR is characterized by a high plant efficiency and a high fuel discharge burnup level. More specifically, the (pebble-bed type) High Temperature Reactor (HTR) is known for its inherently safe characteristics, coming from a negative temperature reactivity feedback, a low power density and a large thermal inertia of the core. The core of a pebble-bed reactor consists of graphite spheres (pebbles) that form a randomly packed porous bed, which is cooled by high pressure helium. The pebbles contain thousands of fuel particles, which are coated with several pyrocarbon and silicon carbon layers that are designed to contain the fission products that are formed during operation of the reactor. The inherent safety concept has been demonstrated in small pebble-bed reactors in practice, but an increase in the reactor size and power is required for cost-effective power production. An increase of the power density in order to increase the helium coolant outlet temperature is attractive with regard to the efficiency and possible process heat applications, such as hydrogen production. However, this increase leads in general to higher fuel temperatures, which could lead to a consequent increase of the fuel coating failure probability. This thesis deals with the pebble-bed type VHTR that aims at an increased coolant outlet temperature of 1000 °C and beyond in order to increase reactor performance and to allow for cost-effective production of hydrogen using nuclear energy.

For the simulation of the neutronic and thermal-hydraulic behavior of the reactor the DALTON-THERMIX coupled code system has been developed and has been validated against experiments performed in the AVR and HTR-10 reactors. An analysis of the 400 MW_{th} Pebble Bed Modular Reactor (PBMR) design shows that the inherent safety concept that has been demonstrated in practice in the smaller AVR and HTR-10 reactors, can also be applied to a commercial size reactor. The fuel temperatures of this design remain below the limits, both during nominal operation as well as during anticipated Depressurized Loss Of Forced Coolant (DLOFC) transients. However, it is shown that the fuel temperature during a DLOFC incident will reach the 1600 °C limit in a small part of the core after 22 hours without active intervention. Therefore, a further increase of the reactor power to raise the helium outlet temperature is unattractive.

A one dimensional visco-elastic stress analysis code (PASTA) has been developed for analysis of mechanical stresses in the coatings of the particle fuel during irradiation. An analysis of the coating stresses in the PBMR design shows that there is sufficient room for an increase in operating temperature with regard to the SiC coating layer stress during nominal operation. An analysis of a VHTR design with increased helium outlet temperature shows that up to an outlet temperature of 1075 °C the SiC layer remains in compression during the entire lifetime of the coated particle. It was found that the graphite matrix in which the particles are embedded provides additional compressive stress to the SiC layer and delays the time point at which the compressive stress in this layers turns to tensile. This is beneficial for this main load barer of the particle, which is only expected to fail under high tensile stress.

The total number of times that a certain pebble is (re)introduced in the core can be increased to flatten the axial power and the fuel temperature profile. The effect has been analyzed by linking the DALTON-THERMIX code system with fuel depletion analysis calculations using SCALE. For nominal operation a total of six pebble passes is optimal since the peak in the axial power profile in the top region of the core matches the cool helium temperatures in this region. For a DLOFC case, in which the maximum fuel temperature is determined largely by the peak in the power profile, a further increase to ten pebble passes is found to be advantageous. By creating several radial fuel zones in the core in combination with multiple pebble recycling steps the radial distribution of fissile material can be influenced. For a two zone core it was found that by recycling the pebbles eight times in the outer zone and two times in the inner zone consecutively, the peak in the radial power profile reduces from 10 MW/m³ to 8.7 MW/m³. The maximum power density can be further reduced to 8.2 MW/m³ using three radial fuel zones. For an improved pebble bed design with three radial fuel zones, the maximum fuel temperature during normal operation and during a DLOFC transient is reduced by 80 °C and 300 °C, respectively.

A Once-Through-Then-Out (OTTO) fueling scheme can be used to approximate the optimal power profile yielding an axially flat fuel temperature profile. The resulting high peak in the power profile which causes high temperatures in a small region of the core during a DLOFC transient are not expected to lead to a high particle failure probability, since the particles in that region have a low fuel burnup level. By altering the coolant flow from axial to radial direction, the pressure drop in the pebble bed can be reduced tremendously, which results in an increase of the plant efficiency with several percent. The resulting increase in fuel temperature can be compensated by reducing the pebble size or by recycling the pebbles from the outside of the core to the inside. In the latter case, the power profile has its peak on the outside of the core, which is also advantageous in a DLOFC case.

An increase of the reactor power is allowable if one or more of the above proposed design or fuel management modifications would be implemented in current reactor designs. This would lead to an increase of the reactor performance and the availability of high temperature helium for process heat applications.

Delft, The Netherlands, October 2008,

B. Boer

Samenvatting

Het internationale Generatie IV onderzoeksforum voor kernenergie heeft zes veelbelovende kernreactorconcepten geselecteerd voor verdere ontwikkeling met als doel deze reactoren beschikbaar te maken voor energieproductie in de tweede helft van de 21^{ste} eeuw. De Very High Temperature Reactor (VHTR) (Zeer Hoge Temperatuur Reactor) is één van die vierde generatie nucleaire reactoren die worden gekarakteriseerd door een hoog rendement en een hoge opbrand van de nucleaire brandstof. De Hoge Temperatuur Reactor (HTR) wordt bovendien gekenmerkt door zijn inherent veilige eigenschappen, die voortkomen uit een negatieve terugkoppeling van de temperatuur van de kern naar de reactiviteit, een lage vermogensdichtheid en een grote thermische capaciteit. Hierdoor zal de kettingreactie uitdoven als de temperatuur onvoorzien oploopt tijdens een ongevalsituatie en is het mogelijk dat de kern afkoelt zonder aanwezige (nood)koeling. De kern van een kogelbed (pebble-bed) type HTR bestaat uit grafietkogels die een willekeurig gestapeld poreus bed vormen, waardoor de heliumkoeling onder hoge druk stroomt. De kogels (pebbles) bevatten duizenden brandstofdeeltjes in een coating van pyrolytische carbon en siliciumcarbide, die zijn ontworpen voor de retentie van splijtingsproducten die tijdens reactorbedrijf worden gevormd. De brandstof in de reactor kan tijdens bedrijf worden gewisseld door de opgebrande kogels te verwijderen aan de onderkant van de kern en door verse kogels aan de bovenkant toe te voegen.

Het onderzoek van dit proefschrift is gericht op het kogelbed type VHTR welke streeft naar een helium uitlaattemperatuur van tenminste 1000 °C. Het concept van inherente veiligheid is in de praktijk met succes gedemonstreerd in kleine kogelbedreactoren. Een voorwaarde voor kosteneffectieve vermogensproductie is het opschalen van deze demonstratiereactoren naar een groter vermogen. Bovendien is een verhoging van de vermogensdichtheid teneinde de helium uitlaattemperatuur te verhogen aantrekkelijk met het oog op het thermodynamisch rendement en het gebruik van de warmte in industriële processen, zoals waterstofproductie. Deze vermogensverhoging leidt in het algemeen tot hogere brandstoftemperaturen, wat mogelijk falen van de brandstofcoatings tot gevolg heeft.

Voor de simulatie van het thermo-hydraulisch gedrag gekoppeld aan het neutronentransport in de kern van een HTR is de DALTON-THERMIX computercode ontwikkeld, welke is gevalideerd met experimentele gegevens van de AVR en HTR-10 reactoren. Een analyse van het 400 MW_{th} Pebble Bed Modular Reactor (PBMR) ontwerp laat zien dat het concept van inherente veiligheid, wat is gedemonstreerd in de AVR en HTR-10, ook kan worden toegepast op grotere reactorontwerpen. De

brandstoftemperaturen in dit ontwerp blijven onder de limietwaarden, zowel tijdens normaal bedrijf als tijdens een situatie waarin een verlies van actieve kernkoeling optreedt. De analyse toont echter ook dat de temperatuur van een klein deel van de kern de limietwaarde van 1600 °C bereikt na 22 uur zonder interventie van de operator, indien naast actieve koeling ook de systeemdruk wegvalt. Hierdoor is de gewenste verhoging van het reactorvermogen zonder verdere aanpassing van het ontwerp onaantrekkelijk.

Een één-dimensionaal visco-elastisch analytisch model (PASTA) is ontwikkeld voor de analyse van de mechanische spanningen in de coatings van de brandstofdeeltjes tijdens bestraling in de kern. Een analyse van de spanningen in de coatings van de PBMR laat zien dat er voldoende ruimte is voor een verhoging van de temperatuur in de kern, wanneer de tangentiële spanning in de SiC coating tijdens normaal reactorbedrijf als maatstaf wordt genomen. Een analyse van een VHTR versie van de PBMR toont aan dat de helium uitlaattemperatuur kan worden verhoogd tot 1075 °C zonder dat de SiC coating aan trekspanning wordt blootgesteld. Door invloed van bestraling met neutronen krimpt de grafiet matrix waarin de brandstofdeeltjes zijn ingebed. Dit heeft tot effect dat de SiC coating onder een hogere tangentiële drukspanning staat dan wanneer het deeltje in vacuüm zou zijn bestraald. Dit is een voordelig effect aangezien het falen van de SiC coating enkel onder een grote trekspanning is te verwachten.

Door het aantal keren dat een brandstofkogel in de kern wordt geïntroduceerd te verhogen kan het vermogens- en temperatuurprofiel in de kern worden afgevlakt. Het effect is geanalyseerd, gebruikmakend het SCALE codepakket voor opbrandanalyse dat is gekoppeld aan het DALTON-THERMIX codesysteem. Uit de analyse volgt dat wanneer men de kogels zes keer door de kern laat passeren, de maximale reductie in brandstoftemperatuur reeds wordt bereikt. Uit een transientanalyse, waarin verlies van actieve koeling en systeemdruk wordt aangenomen, blijkt een totaal aantal van tenminste tien kernpassages nog tot een reductie van de maximale brandstoftemperatuur te leiden. Door het wegvallen van actieve koeling is de maximale temperatuur in een dergelijke transient sterk afhankelijk van de maximale vermogensdichtheid in de kern. Door de kern in radiale zin op te delen in zones waarin de kogels gedurende hun levensduur in een specifieke volgorde worden geïntroduceerd kan het radiale vermogensprofiel ook worden afgevlakt. De vermogenspiek kan hierdoor worden afgevlakt van 10 MW/m³ naar 8.7 en 8.2 MW/m³ voor respectievelijk twee en drie radiale zones. Gebruikmakend van meervoudige recycling en brandstofzoning kan de maximale temperatuur met 80 °C en 300 °C worden gereduceerd respectievelijk voor nominaal bedrijf en voor een transient met verlies van koelmiddel.

Door gebruik te maken van een beladingsschema waarin de kogels slechts éénmaal de kern passeren kan het optimale vermogensprofiel worden benaderd wat resulteert in een vlak temperatuurprofiel tijdens nominaal bedrijf. Het resulterende vermogensprofiel heeft in dit geval een hoge piek, wat tot hoge brandstoftemperaturen leidt in een klein deel van de kern tijdens een ongevalsituatie met koelmiddelverlies. Deze hoge temperaturen leiden echter niet tot een hoge faalkans van de brandstofcoatings doordat het gebied waarin ze optreden, gekenmerkt wordt door een lage opbrand van de splijstof.

Door de stroomrichting van het koelmiddel van axiaal naar radiaal te veranderen kan het drukverlies door frictie significant worden gereduceerd, waardoor het rendement van de reactor met enkele procenten toeneemt. De resulterende verhoging in brandstoftemperatuur kan worden teruggedrongen door de kogels te verkleinen of door de kogels van buiten-naar-binnen te recycleren, gebruikmakend van meerdere radiale zones in de kern. In het laatsgenoemde geval heeft het vermogensprofiel zijn piek aan de buitenkant van het kogelbed, wat voordelig is in geval van een transient met koelmiddelverlies.

Een verhoging van het reactorvermogen is derhalve mogelijk indien één of meerdere van de bovenstaande ontwerpmodificaties worden doorgevoerd. Dit verhoogt het rendement van de reactor en maakt het mogelijk de hoge helium temperatuur te benutten in industriële warmteapplicaties, zoals waterstofproductie.

Delft, Oktober 2008,

B. Boer

Acknowledgments

Eindelijk is het boekje af!

Graag wil ik een aantal mensen bedanken die geholpen hebben bij de totstandkoming van dit proefschrift.

Op de eerste plaats zijn dit Prof. Tim van der Hagen en Dr. Jan Leen Kloosterman die mij hebben begeleid gedurende het promotieonderzoek. Jan Leen was altijd bereikbaar om advies te geven of ideeën te bespreken. Ook de aanwezigheid van Prof. Hugo van Dam tijdens werkbesprekingen en presentaties heb ik als zeer prettig en positief ervaren.

In een andere context wil ik Harald Labout bedanken voor het beschikbaar stellen van de foto ('ballorig') die gebruikt is voor de cover van dit proefschrift.

Ik heb de afgelopen jaren met plezier gewerkt op het Reactor Instituut Delft en wil daarvoor iedereen van de sectie PNR bedanken. Ik pik er een paar bijzondere gevallen uit:

Danny Lathouwers heeft mij niet alleen enorm geholpen met de fantastische DALTON code, die onmisbaar was voor mijn onderzoek, maar ook met de vele adviezen en niet te vergeten de wielertaining voor de Amstel Gold!

Wilfred ('chocoladeschuimgebak') van Rooijen, mijn kamergenoot tijdens de eerste drie jaar van mijn onderzoek, wil ik vooral bedanken voor alle politiek incorrecte opmerkingen en eindeloze verhalen tijdens koffiepauze en lunch, maar natuurlijk ook voor al zijn hulp met Perl en SCALE.

Masterstudenten Sieuwert de Zwaan en Andrea Ooms heb ik met veel plezier begeleid tijdens hun afstuderen. De combinatie van Sieuwert en Wilfred op een kamer kon af en toe voor veel achtergrondruis zorgen, maar garandeerde wel een erg gezellige werksfeer.

Stavros Christoforou and Jérôme Jonnet helped me out on many occasions, and I'm not only talking about dealing with bottles of Laurent-Perrier, thanks!

Special thanks go to Ming Ding from Beijing for whom I have an enormous respect. Ming was able to tackle the complex AVR benchmark and produced some very nice simulation results, which can be found in Sec. 2.4 of this thesis.

I would like to thank Abderrafi Ougouag and Hans Gougar for giving me the opportunity to work at the Idaho National Lab and their guidance. A big thank you to Javi Ortensi and the van Sickle family for making my life outside the lab more

Acknowledgments

enjoyable by taking me rafting, diving and hiking in Idaho.

Nele, de momenten waarop ik het even had gehad met de pebbles heb jij mijn frustraties kunnen verzachten. Jouw geduld en aandacht zijn van onschatbare waarde.

Als laatste wil ik graag mijn ouders bedanken voor al hun aanmoedigingen en de interesse voor mijn onderzoek.

Curriculum Vitae

Brian Boer

E-mail: b.boer@tudelft.nl

Date and place of birth: 23-12-1978; Rotterdam, the Netherlands

Professional Experience

- 2004 - ... PhD candidate at the Reactor Institute Delft, Delft University of Technology
Optimization of the core design and the fuel management of a High Temperature Pebble-Bed Reactor
- 2006 Internship at the Idaho National Laboratory (INL), USA
Modeling and analysis of mechanical stresses in coated particle fuel and graphite of High Temperature Reactors
- 2000 - 2004 Consultant (part-time)
Thermal-hydraulic analysis of heated storage tanks and pipes in the petrochemical industry

Education

- 1997 - 2004 M.Sc, Mechanical Engineering at the Delft University of Technology
Specialization: Energy Technology. Thesis title: Feasibility of a High Temperature Nuclear Reactor as backup system for Wind Power
- 2002 - 2003 Research project at the University of Potchefstroom (PUK), South Africa
Investigation of the thermal-hydraulics of the Pebble Bed Modular Reactor
- 1991 - 1997 Preparatory Scientific Education (VWO) at Het Rotterdamsch Lyceum, Rotterdam, The Netherlands

blank page

blank page

blank page